ISBN 978-82-326-6694-2 (printed ver.)
ISBN 978-82-326-5937-1 (electronic ver.)
ISSN 1503-8181 (printed ver.)
ISSN 2703-8084 (electronic ver.)

NTNU
Norwegian University of
Science and Technology

Doctoral theses at NTNU, 2022:62

Yingpeng Zhen

Electrochromic Tungsten Oxide Nanofilms and Ionic Liquid Based Ion Conductor for Smart Windows Development: Preparation, Characterization and Applications

Yingpeng Zhen
Doctoral thesis

NTNU
Norwegian University of
Science and Technology
Thesis for the degree of
Philosophiae Doctor
Faculty of Engineering
Department of Civil and Environmental
Engineering

Doctoral theses at NTNU, 2022:62
NTNU

NTNU
Norwegian University of
Science and Technology

Yingpeng Zhen

Electrochromic Tungsten Oxide Nanofilms and Ionic Liquid Based Ion Conductor for Smart Windows Development: Preparation, Characterization and Applications

Thesis for the degree of Philosophiae Doctor

Trondheim, November 2022

Norwegian University of Science and Technology
Faculty of Engineering
Department of Civil and Environmental Engineering

NTNU
Norwegian University of
Science and Technology

NTNU
Norwegian University of Science and Technology

Thesis for the degree of Philosophiae Doctor

Faculty of Engineering
Department of Civil and Environmental Engineering

ISBN 978-82-326-6694-2 (printed ver.)
ISBN 978-82-326-5937-1 (electronic ver.)
ISSN 1503-8181 (printed ver.)
ISSN 2703-8084 (electronic ver.)

Doctoral theses at NTNU, 2022:62

PRINTED IN NORWAY
NO - 1598

NORDIC SWAN ECOLABEL
Printed matter
2041 0731

Printed by Skipnes Kommunikasjon AS

Preface

This thesis is submitted to the Norwegian University of Science and Technology (NTNU) in partial fulfillment of the requirements for the degree of Philosophiae Doctor (Ph.D.).

The Ph.D. thesis mainly consists of seven peer-reviewed articles or manuscripts. The work for this thesis has mainly been performed at the Department of Civil and Environmental Engineering, NTNU, Trondheim. My main supervisor is Professor Bjørn Petter Jelle. The co-supervisor is Dr. Tao Gao. Parts of the experimental work were performed at NTNU Nanolab.

The Ph.D. project was financed by the Research Council of Norway and several partners through The Research Centre on Zero Emission Buildings (ZEB) (project no. 193830). The Research Council of Norway is acknowledged for the support to the Norwegian Micro- and Nano-Fabrication Facility, NorFab, with project number 245963/F50.

Acknowledgements

I am very grateful to my supervisor Professor Bjørn Petter Jelle for giving me the opportunity to perform my Ph.D. project in his research group. I thank him for his valuable guidance, diligent attitude and enthusiasm for my scientific research work. In addition, he gave me much encouragement when I faced difficulties and hesitated to continue with my research. I would also like to thank my co-supervisor Dr. Tao Gao, for his valuable discussions, suggestions, comments, and help during the work on the Ph.D. project.

Many thanks are owed to the engineers at NTNU Nanolab for the good working environment and for giving a lot of training in the use of instruments, as well as technical support. I would especially like to express my sincere thanks to Svenn Ove Linde, Mathilde Isabelle Barriet, Trine Østlyng Hjertås, and Ken Roger Ervik for their help during my research. Additionally, Kristin Høydalsvik Wells is thanked for her help in conducting the XRD experiments.

Many thanks to the administrative staff in my department: Maren Berg Grimstad, Marit Skjåk-Bræk, Elin Mette Tønset, Maria Therese Bergan, and Kjerstina Røhme for helping me during the period of my Ph.D. project. I would also like to thank Kåre By, a member of the technical staff. Additionally, I give many thanks to Erlend Andenæs, Anna Fedorova, and Per-Olof Andersson Borrebæk for the useful discussions in our office.

I thank my mother, father and brother. They have given me a lot of encouragement in phone or video conversation during the period of my Ph.D. project.

Last, but not least, I am very grateful to my husband for his love, support and help during my research for the thesis. When I felt unwell or found it difficult to work on the project, he always had good ideas to help and support me. He is also acknowledged for checking mistakes in earlier drafts of the thesis. I am also grateful to my daughter and my son. They make my heart return to peace when I meet difficulties. During the work of my Ph.D. project, I have obtained fruitful outcomes, including research results and my two lovely children.

Abstract

The main objective of this thesis is to investigate electrochromic nanofilms and ionic liquid ion conductors (electrolyte) to make electrochromic devices for electrochromic smart window development. Electrochromic film and ion conductor are two main parts in the structure of an electrochromic device. Tungsten oxide (WO_3) nanofilms and ionic liquid ion conductors are prepared and characterized to make electrochromic devices for further electrochromic smart windows applications.

WO_3 is one of the most important and popular electrochromic materials for electrochromic smart window applications. Recent academic work has shown that nanostructured electrochromic materials have distinct advantages for high performance electrochromic device applications, including improved cycling stability, high coloration efficiency, and fast switching ability. Firstly, in this thesis, the main work relating to preparation, characterization, and application of WO_3 electrochromic thin films for electrochromic smart window glass was described in Papers 1-4. Electrochromic WO_3 thin films were prepared using a radio frequency (RF) sputtering method to form a transmittance switchable coating for application in electrochromic smart windows. The thickness of the WO_3 film can be controlled and prepared at nanometer scale. The physical properties, including morphology and microstructures, of WO_3 film samples were characterized using x-ray diffraction (XRD), scanning electron microscope (SEM), and Fourier transform infrared (FTIR) spectroscopy. The electrochromic properties of WO_3 thin films were investigated using cyclic voltammetry (CV) analysis and ultraviolet-visible-near infrared (UV-VIS-NIR) spectroscopy. Experiments were performed with the aim of improving the electrochromic performance of as- prepared WO_3 thin films. Effect of film thickness on the electrochromic performance of WO_3 films was investigated. Subsequently, effect of the presence of oxygen on the sputtering process of WO_3 films was investigated. The effect of heat treatment on WO_3 coatings was also investigated.

In addition, Paper 5, Paper 6 and Paper 7 represented fundamental research work on ionic liquids (ILs). The aim of the research was to select and screen suitable ILs as ion conductors (electrolyte) for electrochromic smart window development. ILs are types of salts, which are liquid at temperatures below 100 ^{o}C. There are also ILs with liquid state at room temperature, which are called room temperature ILs. They have many advantageous properties for utilization as electrolyte in electric devices and electrochromic devices. ILs utilized in this work are an extremely safe type of electrolyte since they are not water-sensitive or oxygen-sensitive, and when used in an electrical device they are not flammable. Therefore, there is no risk of explosion or fire associated with the use of ionic liquid (IL) based electrolytes. In this thesis, chemical and physical properties, such as density, viscosity,

crystallization temperature, thermal stability, ionic conductivity, and electrochemical window of ionic liquid-based electrolytes were investigated for electrochromic smart windows applications.

Paper 1 describes preparation and characterization of WO_3 thin films with a thickness of 36 nm. Firstly, WO_3 thin films were prepared using radio frequency (RF) sputtering method. Subsequently, electrochromic properties of as-prepared WO_3 films were investigated using CV analysis and UV-VIS-NIR spectroscopy. At a scan rate of 20 mV/s, the color of the WO_3 films changed at around -0.15 V and bleached at around +0.05 V. The WO_3 films could be cycled for 200 times with the potential between -0.30 V and +0.30 V vs. Ag/AgCl reference electrode (3M KCl aqueous solution). The results of CV test and UV-VIS-NIR spectroscopy demonstrated that the transmittance of the WO_3 film could be regulated by an adjustable external voltage (electric field).

Paper 2 reported preparation and characterization of WO_3 thin films with various thickness, including 36 nm, 72 nm, 108 nm and 180 nm, using sputtering method. Effect of film thickness on the structure and physical properties of WO_3 films was investigated. Bleached WO_3 films were pale gray, pale blue, lemon green or brown in color. Simultaneously, colored films had a blue color with different transmittance levels. Among the WO_3 film samples with various thickness of 36 nm, 72 nm, 108 nm, and 180 nm, the largest transmittance modulation, ΔT_{550nm}, was obtained from samples with a thickness of 108 nm, which was 66% when measured using 0.5 M H_2SO_4 as ion conductor. This showed that the transmittance value of colored samples decreased with the increasing of film thickness. However, in the bleached samples the transmittance was not influenced significantly by the thickness of the samples. To summarize, the prepared WO_3 films with various thicknesses showed various colors.

Paper 3 described preparation and characterization of WO_3 thin films with thickness of 72 nm using RF sputtering method. In addition, the effect of oxygen during the sputtering process on WO_3 film formation and effect of heat treatment on WO_3 film were investigated. As shown in Paper 3, Sample D was prepared as follows. Firstly, a WO_3 thin film was coated on the surface of a conductive indium tin oxide (ITO) glass using RF sputtering under O_2 and argon atmosphere (volume ratio of O_2 and argon is ca. 1:4). Subsequently, the obtained WO_3 thin film was treated with heat flow. In the end, Sample D was obtained. The results showed that the coating of the film on the surface of Sample D was a crystalline WO_3 film. Sample D had a transmittance value of 50.9%. It also had the best aging ability compared with the other films that were prepared. Sample D had the largest transmittance modulation value among the four samples. The results also showed that electrochromic performance of the WO_3 sample films were improved in the presence of O_2 during the RF sputtering process. Moreover, heat treatment might result in a transition of crystalline phase from amorphous to monoclinic of the sputtered WO_3 thin films. Furthermore, aging durability showed a large

improvement after the crystal transition. The crystal transition also resulted in an increased transmittance modulation value of WO_3 thin film samples.

Paper 4 presented the research work on electrochromic materials (ECMs) and electrochromic windows (ECWs). In order to show dynamic and flexible solar radiation ability, ECWs can be characterized by several different solar radiation glazing factors as follows: ultraviolet solar transmittance (T_{uv}), visible solar transmittance (T_{vis}), solar transmittance (T_{sol}), solar material protection factor (SMPF), solar skin protection factor (SSPF), external visible solar reflectance ($R_{vis,ext}$), internal visible solar reflectance ($R_{vis,int}$), solar reflectance (R_{sol}), solar absorbance (A_{sol}), emissivity (e), solar factor (SF), and color rendering factor (CRF). Comparison of these important solar quantities for various ECM and ECW combinations and configurations enable the selection of the most appropriate ECM/ECW for specific electrochromic smart window and building applications.

Paper 5 presented the investigations of thermal properties of ILs, including thermal conductivity and thermal diffusivity. The thermal properties were crucial and important to utilize ILs as ion conductors in electrochromic smart windows. Thermal conductivity of water and some pure ILs, including $BmimBF_4$, $BmimPF_6$, OmimCl, $BmimFeCl_4$, and $OmimFeCl_4$, was measured. It was found that thermal conductivity measurements of ILs using the hot disk method had high accuracy compared with the thermal conductivity measurement values of water, $BmimBF_4$, and $BmimPF_6$ as reported in the literature. Therefore, the hot disk method can be utilized for thermal conductivity measurement of ILs. In addition, the thermal diffusivity of pure ILs, including $BmimBF_4$, $BmimPF_6$, $BmimFeCl_4$, OmimCl, and $OmimFeCl_4$, was measured. The results showed that ILs resulted in less energy loss than water in energy storage. This also demonstrated that ILs have better performance than water based ion conductors in electrochromic smart windows due to less energy loss and consumption.

Paper 6 investigated density, viscosity, heat capacity, decomposition temperature, ionic conductivity, and electrochemical window of IL based electrolytes (ion conductor). These physical and chemical properties of ILs are important when ILs are applied as electrolytes (ion conductor) in making electrochromic smart window and electric devices. Initially, density of ILs was measured using a density meter. Thereafter, viscosity of various ILs was investigated using a rheological method. In addition, crystalline temperature of various ILs samples was investigated using differential scanning calorimetry (DSC). Moreover, decomposition temperature of ILs was investigated using thermogravimetric analysis (TGA). Furthermore, ionic conductivity and electrochemical window of ILs samples were measured using electrochemical instruments.

Paper 7 presented a pure ionic liquid of 1-butyl-3-methylimidazolium tetrachloroferrate ($BmimFeCl_4$), which was synthesized and utilized as electrolyte (ion conductor) in this work. Chemical structure, physical and thermal stability properties, including density, viscosity, melting

point and decomposition temperature, of $BmimFeC1_4$ were investigated. In addition, electrochemical properties of the prepared ILs, including electrochemical window and ionic conductivity, were investigated. Moreover, $BmimFeCl_4$ is used as an electrolyte in an electric device, iron-ion battery, to investigate the performance of ILs ion conductor for reversible redox couple transformation in electrochemical reaction. The results showed that ILs have good electrochemical properties and can be further applied as ion conductors in electrochromic smart windows. The reason why $BmimFeCl_4$ was utilized in this paper is that: (1) Easy to synthesize; (2) Not water or oxygen sensitive; (3) Low cost; (4) Non-flammable; (5) Good thermal, physical and chemical properties, including low melting point, high decomposition temperature, and low viscosity. $BmimFeCl_4$ is not a perfect ion conductor for electrochromic devices because of the color of $BmimFeC1_4$. However, Due to the good properties of ILs, other transparent ILs with color will be further employed to produce electrochromic glass for electrochromic smart windows applications.

List of included papers

Paper 1. Yingpeng Zhen, Tao Gao, and Bjørn Petter Jelle. Synthesis and characterization of tungsten oxide electrochromic thin films. 2018 IEEE 18th International Conference on Nanotechnology *(2018 IEEE-NANO).* DOI: 10.1109/NANO.2018.8626293 , 2018.

Paper 2. Yingpeng Zhen, Bjørn Petter Jelle, and Tao Gao. Electrochromic properties of WO_3 thin films: The role of film thickness. *Analytical Science Advances* 1(2), 124–131, 2020.

Paper 3. Yingpeng Zhen, Bjørn Petter Jelle, and Tao Gao. Influence of O_2 on electrochromic WO_3 thin films preparation using radio frequency sputtering. (*Under review*)

Paper 4. Bjørn Petter Jelle, Tao Gao, Yingpeng Zhen, and Arild Gustavsen. Electrochromic materials and their characterization by solar radiation glazing factors for smart window applications. *Proceedings of SETCOR International Conference on Smart Materials and Surfaces (SMS Bangkok 2014)*, 26th - 28th of August, 2014.

Paper 5. Yansong Zhao, Yingpeng Zhen, Bjørn Petter Jelle, and Tobias Boström. Measurements of ionic liquids thermal conductivity and thermal diffusivity. *Journal of Thermal Analysis and Calorimetry,* 128, 279–288, 2017.

Paper 6. Yansong Zhao, Yingpeng Zhen, and Bjørn Petter Jelle. Ionic liquid based electrolytes preparation and characterization of density, viscosity, crystallization temperature, decomposition temperature, ionic conductivity, and electrochemical. (*Under review)*

Paper 7. Yansong Zhao, Yingpeng Zhen, and Tobias Boström. Rechargeable iron-ion battery using pure ionic liquid electrolyte, *ACS Omega*, 2022, doi: 10.1021/acsomega.1c06170. (*Published*)

Declaration of contributions

Paper 1.

Yingpeng Zhen had the main responsibility for the writing process of the article and the execution of the laboratory experiments. All authors have participated in the writing process, discussions and planning of the work.

Paper 2.

Yingpeng Zhen had the main responsibility for the writing process of the article and the execution of the laboratory experiments. All authors have participated in the writing process, discussions and planning of the work.

Paper 3.

Yingpeng Zhen had the main responsibility for the writing process of the article and the execution of the laboratory experiments. All authors have participated in the writing process, discussions and planning of the work.

Paper 4.

Bjørn Petter Jelle had the main responsibility for the writing process of the article, calculations of the solar radiation glazing factors and the execution of the laboratory experiments. All authors have participated in the writing process and discussions of the work.

Paper 5.

Yansong Zhao designed an experimental work plan. In addition, he prepared experimental samples which were utilized in this work. He had the main responsibility for the writing process of the article too. Yingpeng Zhen had the main responsibility for the execution of the laboratory experiments of thermal conductivity and thermal diffusivity measurements using the hot disk method for the samples, including water, $BmimBF_4$, $BmimPF_6$, OmimCl, $BmimFeCl_4$, $OmimFeCl_4$, and ILs + nanoparticles systems. All authors have participated in the writing process and discussions of the work.

Paper 6.

Yansong Zhao had the main responsibility for the writing process of the article and the execution of the laboratory experiments. Yingpeng Zhen joined the laboratory work on the ionic liquids part, including the synthesis of $BmimFeCl_4$ and $OmimFeCl_4$, the preparation of samples of NPs in ILs,

such as 0.55 % Fe_3O_4 NPs in $BmimBF_4$, 0.33 % Fe_2O_3 NPs in $BmimBF_4$, 0.13% R711 NPs in $BmimPF_6$, 0.28 % Fe_3O_4 NPs in $BmimFeCl_4$, and 0.46% Fe_3O_4 NPs in $OmimFeCl_4$, as well as ionic conductivity and electrochemical windows measurement of samples utilized in this work. All authors have participated in the writing process and discussions of the work.

Paper 7.

Yansong Zhao had the main responsibility for the writing process of the article and the execution of the laboratory experiments. Yingpeng Zhen joined the laboratory work on the ionic liquids part, including the synthesis of $BmimFeCl_4$, anode preparation, and cathode preparation. All authors have participated in the writing process and discussions of the work.

Publications not included in this thesis

During the work on this Ph.D. thesis, I also contributed to following publications which are not part of this thesis:

- Serina Ng, Bjørn Petter Jelle, Yingpeng Zhen, and Olafur Wallevik, Effect of storage and curing conditions at elevated temperatures on aerogel-incorporated mortar samples based on UHPC recipe, *Construction and Building Materials*, 106,640-649, 2016.
- Yansong Zhao, Zhonghua Chen, Fei Yang, and Yingpeng Zhen, Ionic liquid: A promising material for petroleum production and processing. *Current Organic Chemistry*, 24, 1763-1774, 2020.
- Yansong Zhao, Yingpeng Zhen, Tobias Boström, Stefano Passerini, Dominic Bresser, and Aranna Moretti. Rechargeable iron-ion battery. Application No. 20180939 filed on 3rd July 2018.

Abbreviations

A	Absorbance
A_{sol}	Solar absorbance
ATR	Attenuated total reflectance
$BmimBF_4$	1-butyl-3-methylimidazolium tetrafluoroborate
BmimCl	1-Butyl-3-methylimidazolium chloride
$BmimFeCl_4$	1-butyl-3-methylimidazolium tetrachloroferrate
$BmimPF_6$	1-butyl-3-methylimidazolium hexafluorophosphate
CE	Counter electrode
C-Fe	Carbon coated iron
CRF	Color rendering factor
CMC	Sodium carboxymethyl cellulose
CV	Cyclic voltammetry
CVD	Chemical vapor deposition
DSC	Differential scanning calorimetry
e	Emissivity
ECM	Electrochromic material
ECW	Electrochromic windows
FTIR	Fourier transform infrared
FTO	Fluor-tin oxide (tin oxide doped with fluor, SnO_2:F)
H_xWO_3	Tungsten bronzes
I_0	Intensities of the incident lights
ILs	Ionic liquids
ITO	Indium-tin oxide (indium oxide doped with tin, In_2O_3:Sn)
“Low-e”	Low-emissivity
LCD	Liquid crystal display
NPs	Nanoparticles
η	Coloration efficiency
OD	Optical density
$OmimBF_4$	1-Methyl-3-octylimidazolium tetrafluoroborate
OmimCl	1-methyl-3-octylimidazolium chloride
$OmimFeCl_4$	1-methyl-3-octylimidazolium tetrachloroferrate
PANI	Polyaniline

PB	Prussian blue
PC	Polycarbonate
PDLCs	Polymer dispersed liquid crystals
PEO	Poly(ethylene oxide)
PET	Polyethylene terephthalate
PMMA	Poly(methyl methacrylate)
PVD	Physical vapor deposition
Q	Integration of the current versus the coloration time
RE	Reference electrode
RF	Radio frequency
R_{sol}	Solar reflectance
$R_{vis,ext}$	External visible solar reflectance
$R_{vis,int}$	Internal visible solar reflectance
SEM	Scanning electron microscope
SF	Solar factor
SMPF	Solar material protection factor
SPDs	Suspended-particle devices
SSPF	Solar skin protection factor
TCO	Transparent conducting oxide
TGA	Thermogravimetric analysis
T_{sol}	Solar transmittance
T_{uv}	Ultraviolet solar transmittance
T_{vis}	Visible solar transmittance
T_c	Transmittance value of electrochromic films at color state
T_b	Transmittance value of electrochromic films at bleached stated
τ	The switching time
UV-VIS-NIR	Ultraviolet-visible-near infrared
WE	Working electrode
XRD	X-Ray diffraction
ΔT	Transmittance difference
λ	Denotes the certain wavelength

Contents

Chapter 1. Background

Greenhouse gas emissions may result in global warming, where the harmful effects have become more and more noticeable in recent years. Energy consumption in buildings and greenhouse gases emissions from buildings account for a large part of the total energy consumption and greenhouse gas emissions in developed countries and developing countries [1, 2]. To solve the problem of energy consumption and greenhouse gas emissions from buildings, new technologies and advanced materials for increasing energy efficiency, energy generation, and energy saving have been widely investigated by research teams worldwide.

In 2007, energy consumption in buildings was 37% of the total energy consumption in the EU [3]. In the USA, energy utilized in residential and commercial buildings accounted for ca. 40% of the primary energy consumption in both 2011 and 2015 [4]. The energy consumption distribution in the USA in 2011 is shown in Figure 1.1 [5]. Evidently, the potential for energy savings in the buildings sector is huge [6].

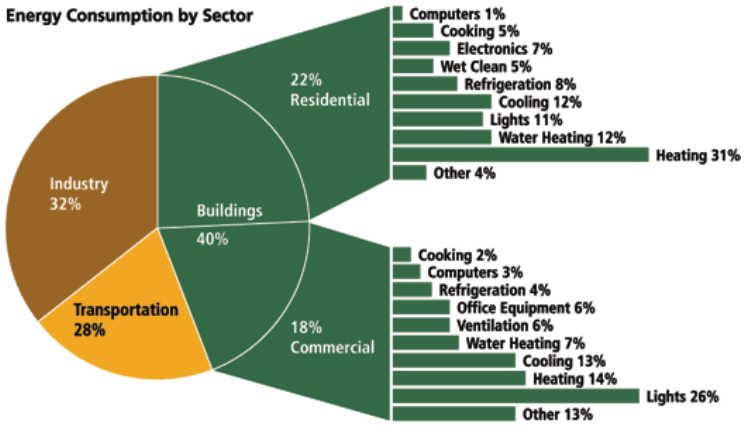

Figure 1.1. Total energy consumption in buildings in the USA in 2011 [5].

Windows are regarded as a low energy efficiency building component, mainly due to their (traditionally) poor thermal insulation properties. Around 60% of a building's heating or air conditioning energy may be lost through its windows [6, 7]. Due to high thermal conductivity of glass (i.e. window panes), heat flow can enter easily into buildings when the outside temperature of the building is high. However, thermal energy is easily transferred from a warm room to the cold outdoor

environment during wintertime. One solution to prevent energy loss would be installation of small windows. However, in practice, current trends are larger windows will be installed in modern buildings. The reason is that windows bring light into buildings and offer wider and greater views of the outdoor locations, where people normally may find more comfortable and enjoyable. For this reason, more and more modern buildings are installed with larger window walls. Therefore, improving windows' energy saving properties is crucial and important to reduce energy loss and energy consumption of housing.

Traditional ways to avoid too much solar energy entering indoors through windows are the utilization of curtains, blinds, awnings, shutters, or combination of these. These measures can decrease heat transfer by thermal radiation. However, visible light is blocked at the same time. In order to solve this problem, researchers have focused on high-performance energy efficient windows, including insulated windows, low-emissivity ("low-e") windows, and smart windows. A short introduction to the principles of heat transfer and some types of high-performance energy efficient windows is shown as follows in Section 1.1.

1.1. Principles of heat transfer

Windows are often characterized as having a low degree of energy efficiency, since large amounts of heat are transferred through them. To reduce unexpected heat transfer, it is necessary to understand the mechanism of heat transfer through windows. There are three fundamental modes in heat transfer: conduction, convection, and radiation. Normally, in real heat transfer processes, it is a combination of two or more modes of the three fundamental modes.

1.1.1. Conduction

If a temperature gradient exists in a continuous substance, heat can be transferred through the substance without any significant motion of matter. This mechanism of heat flow is called conduction and takes place at a micro scale (molecule or atom level). Conduction occurs by rapidly moving or vibrating atoms and molecules that interact with neighboring atoms and molecules. By this way, energy is transferred from one particle to the neighboring particles. Conduction is the most significant means of heat transfer within a solid or between solid objects that are in thermal contact [8]. According to Fourier's law, the heat flux is proportional to the temperature gradient. For one-dimensional heat flow, Fourier's law is

$$\frac{dq}{dA} = -k\frac{dT}{dx} \tag{1.1}$$

where q is the rate of heat flow in the perpendicular direction to surface, A is the heat transfer area, T is the temperature, x is the distance perpendicular to surface, and k is the proportionality constant or thermal conductivity.

In metals, thermal conduction mainly results from the motion of free electrons. In solids that are poor conductors of electricity and in most liquids, thermal conduction results from momentum transfer between adjacent vibrating molecules or atoms. In gases, conduction occurs by the random motion of molecules, where heat is "diffused" from hotter regions to colder ones [8-10].

According to equation 1.1, for a typical heat transfer, the heat transfer area A, the temperature difference between inside and outside ΔT, and the distance perpendicular to surface x are fixed values. To decrease the rate of heat flow in the direction perpendicular to the surface (q), the thermal conductivity of the heat transfer material k should be decreased.

Insulated windows are typically energy efficient. To decrease heat transferred through windows by conduction, materials with low thermal conductivity have been used between the glass pane layers in the window. Insulated windows are described in more detail in section 1.2.1.

1.1.2. Convection

Convection refers to flow of heat associated with the movement of a fluid. The convective flux is usually proportional to the difference between the surface temperature and the temperature of the fluid, as stated in Newton's law of cooling

$$\frac{q}{A} = h(T_s - T_f) \tag{1.2}$$

where T_s is the surface temperature, T_f is the bulk temperature of fluid, far from the surface, and h is the heat transfer coefficient.

Convection is the transfer of heat from one place to another by the movement of fluids. Essentially, the process involves the transfer of heat through mass transfer. Convection is usually the dominant form of heat transfer in liquids and gases [8].

The heat transfer by convection occurs in a fluid medium. To decrease heat transfer through windows with convective air flow, the tightness of the window frames must be ensured. The direction of heat flow is from a high-temperature (warm) place to a low-temperature (cool) place.

1.1.3. Radiation

The term radiation refers to the transfer of energy through space by electromagnetic waves. If radiation occurs in empty space, it is not transformed into heat or any other form of energy, nor is it

diverted from its path. However, if matter appears in its path, the radiation will be transmitted, reflected, or absorbed. Only absorbed energy will transform into heat, and the transformation is quantitative.

The energy emitted by a black body is proportional to the fourth power of the absolute temperature [11]:

$$W_b = \sigma T^4 \tag{1.3}$$

where W_b is the rate of radiant energy emission per unit area, σ is the Stefan-Boltzmann constant, and T is absolute temperature.

Thermal radiation is energy emitted by matter as electromagnetic waves, due to the pool of thermal energy in all matter with a temperature above absolute zero. Thermal radiation is a direct result of the random movements of atoms and molecules in matter. Since atoms and molecules are composed of charged particles (protons and electrons), their movement results in the emission of electromagnetic radiation, which carries energy away from the source [8].

A lot of heat is transferred into rooms by solar radiation, while little heat is transferred from indoor to outdoor of buildings by solar radiation. Heat loss from buildings to outside are mainly by conduction and convection. Energy loss by radiation is very low compared with energy loss by conduction and/or convection. Therefore, energy loss by radiation can be ignored.

The heat and visible light entering the room through the window is mainly solar radiation. Therefore, there are two directions to adjust the amount of energy the window gains or releases. One direction is to reduce heat loss from windows by reducing heat conduction and convection through the window, and the other direction is to tint the transmittance of the window glass to adjust the solar radiation gained through the window.

1.2. Thermal transmittance (U-value)

Thermal transmittance (U-value) is utilized to characterize window panes and glass structures in buildings. It is the rate of heat transfer through a structure. U-value depends on the temperature difference between the inside and outside of the structure. The better insulated a structure is, the lower U-value it will have.

Losses due to thermal radiation, thermal convection and thermal conduction are taken into account in the *U*-value. It is described by the equation:

$$U = \frac{\Phi}{A * (T1 - T2)} \tag{1.4}$$

Where *U* is the thermal transmittance, Φ is the heat transfer in watts, T_1 is the temperature on one side of the structure, T_2 is the temperature on the other side of the structure, and *A* is the area in square meters.

U value is influenced by window frame materials, quality of installation, window structure, and coatings on window panes.

Typical thermal transmittance values for common building structures are as follows [12]:

Single glazing: 5.7 W/(m^2·K)

Single glazed windows, allowing for frames: 4.5 W/(m^2·K)

Double glazed windows, allowing for frames: 3.3 W/(m^2·K)

Double glazed windows with advanced coatings: 2.2 W/(m^2·K)

Double glazed windows with advanced coatings and frames: 1.2 W/(m^2·K)

Triple glazed windows, allowing for frames: 1.8 W/(m^2·K)

Triple glazed windows, with advanced coatings and frames: 0.8 W/(m^2·K).

1.3. Energy efficient windows

To decrease heat transfer between buildings and outside, many types of energy efficient windows have been designed to decrease heat transfer via conduction, convection, or radiation according to the principles of heat transfer. A program called THERM is used to evaluate energy efficient windows. In this section, an introduction is given to some types of energy efficient windows, including insulated windows, low-emissivity ("low-e") windows, and some types of smart windows.

1.3.1. Insulated windows

Insulated windows or insulating glass units (IGUs) are designed to decrease heat transfer by conduction. They have either double or triple glazing, in which the panes of glass are separated by air or other materials with low thermal conductivity than air. Insulated windows can reduce heat transfer significantly. In addition, insulated windows have good transparency.

In many countries, insulated windows have replaced most single-pane windows in modern buildings. Generally, insulated windows reduce heat loss by 50%. Figure 1.2 shows the structure of

a typical insulated window. The gas in the space between the panes can be air, inert gas such as argon, krypton or xenon, or another non-toxic and non-flammable gas, such as nitrogen.

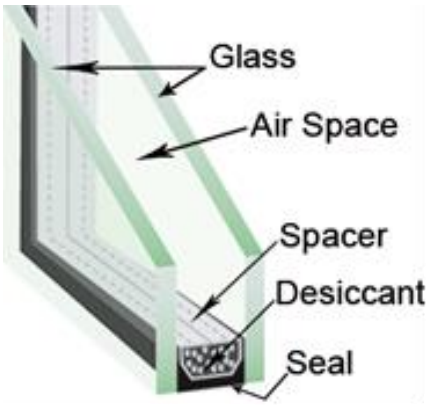

Figure 1.2. Illustration of an insulated window [13].

Moreover, solid materials with low thermal conductivity can be applied between the panes of insulated windows. Recently, research has been performed on insulated windows with aerogel between the panes [14]. Aerogels are dried gels with very high porosity, high specific surface area, and low apparent density. Some aerogel showed optical properties as opaque, translucent, or transparent (as shown in Figure 1.3) [15, 16]. It is possible to utilize the optical properties of aerogels in insulated windows. At ambient pressure, the thermal conductivity can be as low as 0.0135 W/(m·K) [16].

Figure 1.3. A transparent aerogel [15].

The thermal conductivity values of some gases and aerogels that are suitable for utilization in insulated windows are listed in Table 1.1. However, aerogel based insulated windows are still impractical due to the relatively low transparency of this type of windows.

Table 1.1. Thermal conductivity of materials that can be utilized in insulated windows [17-20].

Material	Thermal conductivity (300K) Units: mW/(m·K) (milliwatt per meter kelvin)
glass	1000
Air	26.4
N_2	25.9
Ar	17.7
Kr	9.5
Aerogel	13.0

1.3.2. Low-emissivity windows

Further improvement of the energy efficiency performance is achieved by the use of glass panes with a low- emissivity (low-e) coating —such a coating can reflect a certain amount of infrared light while allowing visible light to pass through. The low-e coating must be located on the side of the gap because it corrodes quickly when exposed to weather conditions.

Therefore, heat energy transferred through windows can be reduced without significant reduction in transparency. In low-e windows, a thin transparent low-e film is applied to the raw soda-lime glass. Such coatings can reflect radiant infrared energy. Therefore, radiant infrared energy is kept on the side of the glass where it originated, while letting visible light pass through the window. As shown in Figure 1.4, low-e windows keep heat inside a building on cold days, and heat outside the building on hot days [21, 22].

Low-e materials can be used to reduce energy usage in both opaque and transparent parts of a building. When low-e materials are utilized in low-e windows, they can reduce the heat transfer through thermal radiation [23]. Compared with an ordinary single-pane window, the best low-e windows can reduce heat loss by around 85% [24].

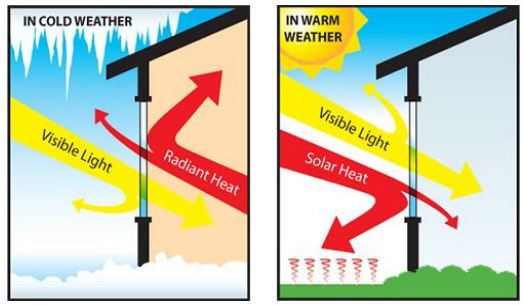

Figure 1.4. Low-e windows transmit most of visible light and block most of infrared radiation (heat) [25].

1.3.3. Smart windows

Smart windows, which are also called switchable windows, have altering optical properties (including transmittance, reflectance, and absorptance) when power is applied. For example, the solar transmittance of smart windows can be regulated by changing the applied power. As a result, the optical state of the windows and the thermal energy absorbed by buildings can be adjusted via smart windows installed in the buildings. The applied power on smart windows can be in the form of, for example, voltage, light, heat, and gas.

There are two main types of smart windows: adaptive smart windows and controllable smart windows. Typical adaptive windows are photochromic smart windows [26] and thermochromic smart windows [27, 28]. Optical properties of photochromic smart windows and thermochromic smart windows are influenced by light intensity or surrounding temperature. Controllable smart windows include electrochromic windows [29, 30], gasochromic smart windows [31], suspended particle smart windows [32], and reversible metal electrodeposited windows [33]. Optical properties of controllable windows can be adjusted by regulating the extra applied power.

It is important to obtain as high transmittance of visible light (T_{vis}) as possible in the transparent state, and at the same time as low T_{vis} as possible in the colored state. In the former case, the goal is to get as much natural light as possible, while in the latter case, it is necessary to block as much solar radiation as possible.

In addition, for the same reasons, it is important for smart windows to have high transmittance values of solar radiation (T_{sol}) or solar factor (*SF,* which refer to transmittance of total solar energy) in their transparent state and low values in colored state [34].

The leading commercially viable switchable technologies are: Solid state electrochromics $LiWO_3$ based SAGE and View windows, and polymer electrolyte based laminated flexible film

ChromoGenics AB. The alternative non-electrochromics are: thermochromic polymers (Pleotint), PDLCs (NSG and others), SPDs (RFI and their licensee's). The polymer laminated electrochromic designs from other companies, for example Gesimat and E-control (Pilkington patents), are no longer in business.

1.3.3.1. Thermochromic windows

Thermochromic material [35] is a type of smart material in which the color will vary as the result of the phase transition caused by temperature change. Thermochromic windows are coated with thermochromic materials. Their reflectance and transmission properties change at a specific critical temperature. Thus, thermochromic windows can automatically control the amount of light and heat in response to temperature variations.

Thermochromic materials can be divided into inorganic, organic and liquid crystal types. Inorganic thermochromic materials mainly include metal iodide, double salt, transition metal compounds, metal alloys, and metal chloride. Organic thermochromic materials include spiropyrans, fluoranthene, triarylmethane, ethylene with substituents and organic complexes, having advantages of optional and adjustable colors, low discoloration temperature, high sensitivity of discoloration and low cost. Liquid crystal can be divided into smectic, nematic and cholesteric types according to molecular arrangement, which has the advantages of good stability and high thermal sensitivity, but its application is limited because of its chemical sensitivity and high cost [35].

Vanadium dioxide (VO_2) is mainly used as a thermochromic material for windows, due to its large reversible changes in optical properties. However, its transition temperature is around 70°C [36]. Doped VO_2 has been studied a lot and some very interesting results have been reported on doping with various metals such as tungsten, molybdenum, or niobium, which make the metallic structure more stable and thus decrease the transition temperature to near the ambient temperature [35, 37]. The value of transmittance in bleached and colored states can also be altered by doping with W as well as with some other metals.

However, in manufacturing, V_2O_5 and VO_x compounds are considered highly toxic, possibly carcinogenic. This is a serious drawback in commercial manufacturing.

The working mechanism of a thermochromic window is shown in Figure 1.5. When the air temperature is below the critical temperature, the material has low infrared reflectance. Consequently, solar radiation and associated heat will enter the interior of the building, as it will not be reflected. Conversely, when the temperature is above the critical temperature, part of the energy from the sun will be reflected, as the material's reflectance will be higher. Therefore, the energy needed for cooling in summer and heating in winter will decrease significantly [38].

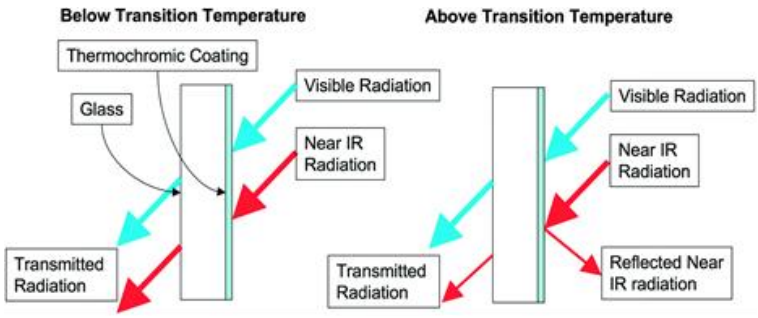

Figure 1.5. Schematic illustration of the thermochromic mechanism [38].

A good thermochromic window should have high values of T_{vis}, T_{sol} and *SF* in the transparent state, and low values of T_{vis}, T_{sol} and *SF* in the colored state. Nevertheless, most thermochromic window products that are currently available in the market have low values of T_{vis} and T_{sol} in their bleached state [39].

1.3.3.2. Photochromic windows

The transmittance of photochromic materials is sensitive to electromagnetic radiation. When the glass is exposed to sunlight, the molecular structure of the photochromic material will change and exhibit a certain color. Photochromic technology is not popular in smart windows. Until now, photochromic windows have not been commercially made. It is because organic photochromic materials are not stable enough, and inorganic photochromic materials are still too expensive for commercial window applications. Photochromic technology is widely utilized in the manufacture of sunglasses [39].

1.3.3.3. Electrochromic windows

Electrochromic windows have optical properties such as transmittance or reflectance that can be regulated by modulation of external electrical power. In the presence of an external voltage, the electrochromic materials can change from a dark state (e.g., dark blue) to a bleached (e.g., transparent, with no color tint) state. Therefore, the amount of light and heat in buildings/rooms by solar radiation can be controlled. Figure 1.6 shows an example of electrochromic windows installed in a building and Table 1.2 lists data for various types of electrochromic windows currently available on the market [34]. Further information on electrochromic windows is provided in Chapter 2.

Research on electrochromic windows has been conducted through eco-friendly building certification systems such as LEED (Leadership in energy and environmental design) in the US, ZEB

(Zero emission buildings) in Norway, BREEAM (The Building research establishment environmental assessment methodology) in the UK, CASBEE (The comprehensive assessment system for built environment efficiency) in Japan, and GSEED (The green standard for energy and environmental design) in South Korea [40]. SageGlass, the pioneer of the world's electrochromic glass, offers benefits such as the ability to optimize daylight, reduce glare and manage heat – all while maintaining unobstructed views of the outdoors. It contributes to many of the requirements of LEED.

Figure 1.6. Electrochromic windows manufacture by SageGlass [41].

Table 1.2. Data for commercially available electrochromic windows [34].

Manufacturer	**Product**	**Size (cm × cm)**	**U_g (W/(m²K))**	**T_{vis}**	**T_{sol}**	**SF**	**Cycles**
SAGE Electrochromics	Classic™	180 × 304	1.59	0.62–0.02	0.38–0.007	0.47–0.09	100,000 30 years
VIEW Inc.	Standard Dual Pane IGU	152.4 × 304.8	1.65	0.58–0.03	0.37–0.01	0.46–0.09	50,000 50 years

1.3.3.4. Gasochromic windows

Gasochromism is the color rendering effect of material that absorbs light waves of a specific wavelength due to a reversible chemical reaction after material comes into contact with certain gases. Gasochromic technology is mainly utilized in the preparation of gas sensors (oxygen, hydrogen, nitric oxide, hydrogen sulfide and carbon monoxide, etc.) [31, 42, 43]. Yoshimura's group at the NIRIN in Nagoya, Japan have investigated gasochromic switchable mirror windows for a long time [44]. There are not commercially viable photochromic windows yet.

1.3.3.5. Liquid crystal display (LCD) windows

Mechanism of utilized in LCD windows is similar to that of polymer dispersed liquid crystals (PDLCs) used in smart windows. PDLCs devices require power for their smart windows to be transparent. In these windows, the liquid crystals respond to an electrical field by aligning parallel and letting light through. When the electrical field is absent, the liquid crystals in the window are randomly oriented. With liquid crystals, the glass is either clear or translucent. There is no intermediate status. Figure 1.7 showed the principle of a PDLC smart windows [45]. PDLC windows have been utilized in offices, restaurants and homes. It can achieve a translucent status to protect privacy without sacrificing all light.

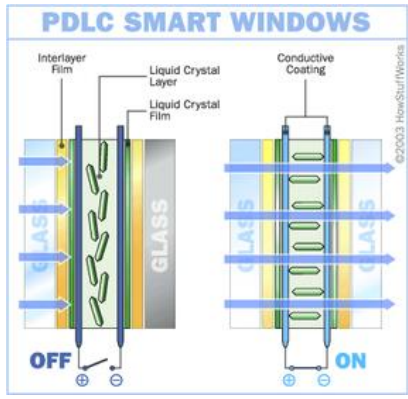

Figure 1.7. Principle of a PDLC smart windows [45].

Figure 1.8. A PDLC smart window [45].

1.3.3.6. Electrophoretic or suspended particle windows

In suspended-particle devices (SPDs), a thin film laminate of rod-like nano-scale particles is suspended in a liquid and placed between two pieces of glass or plastic, or attached to one layer. The principle of SPDs is similar to PDLC windows. When no voltage is applied, the suspended particles are randomly organized, thus blocking and absorbing light. When voltage is applied, the suspended particles align and let light pass. Varying the voltage of the film varies the orientation of the suspended particles, thereby regulating the tint of the glazing and the amount of light transmitted. SPDs can be manually or automatically "tuned" to precisely control the amount of light, glare and heat passing through [32, 46].

1.3.3.7. Reversible metal electrodeposited windows

Reversible metal electrodeposited windows operate through the reversible electrochemical movement of metal atoms on and off a transparent conducting oxide (TCO) electrode. The electrolyte of these windows contains solubilized, nearly colorless metal cations that can be reduced upon application of a cathodic potential to the TCO film to induce optical tinting. Pt nanoparticles adhered to the ITO surface serve as an enhanced metal nucleation seed layer to allow uniform metal electrodeposition at a large scale without significantly influence on transmissivity or conductivity of electrode [33, 47]. Figure 1.9 showed a sample of reversible metal electrodeposited windows prepared by Tyler *et al*. However, these windows were still in the stage of research, which were not commercially available yet due to instability.

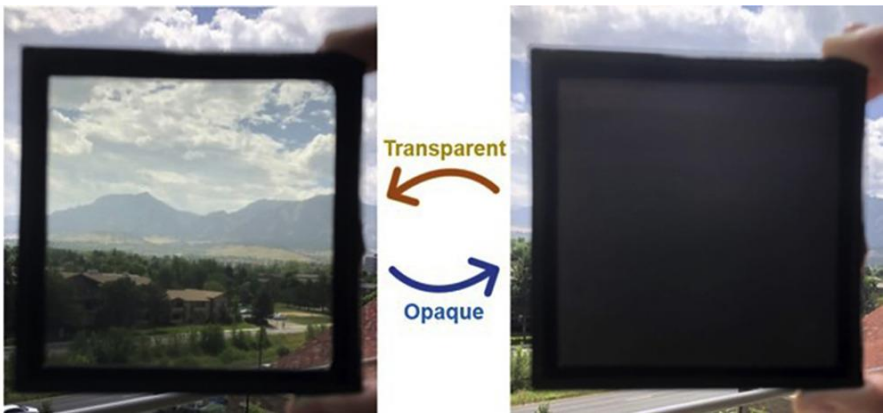

Figure 1.9. A sample of reversible metal electrodeposited window [33].

1.4. Ionic liquids (ILs)

Ionic liquids (ILs) are salt. Many ILs are liquid at room temperature. In theory, there are 10^{18} ILs. Some ILs have only one anion and one cation. However, some ILs may have several anions or cations. Anions of traditional ILs are shown as follows: Cl^-, Br^-, I^-, NO_3^-, SO_4^{2-}, ClO_4^-, BF_4^-, PF_6^-, CF_3COO^-, $CF_3SO_3^-$, Tf_2N^-, NO_3^-, $MeSO_4^-$. Cations of traditional ILs are shown in Scheme 1 as follows [48]:

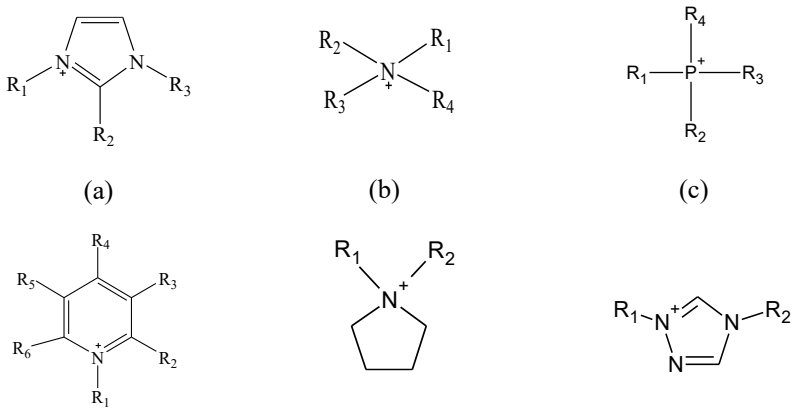

Scheme 1. Six types of cations in traditional ILs: (a) imidazolium; (b) ammonium；(c) phosphonium; (d) pyridinium；(e) pyrrolidinium；(f) triazolium [48].

ILs can be utilized in medical sciences, CO_2 capture, catalysis science, and separation processes. In addition, ILs can be utilized in energy saving, energy conversion, and energy storage applications, for example, in electrochromic smart windows, batteries and solar cells. Some ILs are suitable candidates of electrochromic materials. Aida *et al.* reported a liquid electrochromic cell in a glass U tube containing two immiscible ILs as electrochromic electrode [49]. Additionally, pure ILs can also be utilized as electrolytes. McEwen and Koch proposed ILs as nonflammable electrolytes for electrochemical devices, including electrochromic. Ionic liquid mixed with other materials, but still in liquid final form, can also be used as electrolytes [50].

ILs can improve the current performance of electrochromic and other electrochemical devices. There are some advantages of using ILs as ion conductor (electrolyte) in electrochromic devices. The advantages are as follows.

1. ILs have low vapor pressure, and high thermal and chemical stability properties, which can improve safety properties of electrochromic devices. This means that ILs are better than water based solvent or organic solvent as ion conductors.

2. Low melting point. Many ILs are liquid at temperatures as low as -60°C and therefore can be utilized in cold climate areas. This means that ILs ion conductor is better than water based ion conductor because water based ion conductor becomes solid in cold weather and cannot be utilized as ion conductor.
3. Favorable solubility in inorganic and organic chemicals. ILs have good permeability characteristics to the separator in electrochromic devices.
4. Task-specific ILs can be synthesized from designed chemical and functional groups. In theory, 10^{18} various ILs can be synthesized in the laboratory, which means it is possible to design and synthesize ILs as ion conductors according to specific requirements in producing electrochromic smart windows.
5. Many ILs are environmentally friendly. Therefore, they can replace the current use of toxic electrolytes in electrochromic devices.

Due to the good properties of ILs mentioned above, ILs are investigated and utilized to produce electrochromic glass for electrochromic smart windows development.

Chapter 2. Introduction to Electrochromic Technology and Materials

Electrochromism is the ability for the reversible change to occur in optical properties when a material is electrochemically oxidized or reduced. The concept was proposed by J.R. Platt in 1961 [51]. However, Granqvist claims that the phenomenon has been recognized much earlier: he stated that in 1930 Kobosew and Nekrassow had found that WO_3 showed color change when it was reduced in an acid solvent [52]. In 1951, Brimm found reversible color change caused by electrochemical reaction [53, 54]. In 1953, Kraus described the electrochromic phenomenon of tungsten oxide films in an unpublished report, which did not attract attention [55]. Deb had two papers on tungsten oxide published in 1969 and 1971, respectively [56, 57]. Subsequently, electrochromic science and technology became a hot research topic among researchers worldwide [58].

Commercial interest in electrochromism relates to many applications such as low power displays, smart windows to develop energy-saving buildings as well as light-adapting mirrors in high-end cars and aircrafts [59]. Electrochromic windows can regulate light transmission continuously. Buildings with electrochromic windows have the potential for energy savings in some locations and some seasons. Additionally, comfort factors relating to privacy, glare, and fading have driven interest in the development of electrochromic windows for buildings and vehicles [30].

2.1. Construction and principle of electrochromic devices

The working principle of electrochromic devices is similar to that of batteries. Figure 2.1 shows a schematic construction of a typical electrochromic device. There are basically five layers in the functional part of electrochromic device: transparent conductor layer, electrochromic film layer (as the working electrode (WE)), ion conductor layer (as electrolyte and separator), ion storage film layer (as the counter electrode), and a transparent conductor layer [60]. These layers are between two substrates. Normally, glass is utilized as a transparent substrate in an electrochromic device. For some special applications, a transparent polymer such as polyethylene terephthalate (PET) or polycarbonate (PC) can also be utilized as a substrate.

The key part of the electrochromic device is the cathode/electrolyte/anode, where two electrode layers are separated by an electrolyte layer. At least one of the two electrodes is made from electrochromic materials, which are electrically sensitive, and their color can be altered during an electrochemical reaction process. A cross-sectional diagram of the layers of a typical laminated electrochromic device is shown in Figure 2.2 [61].

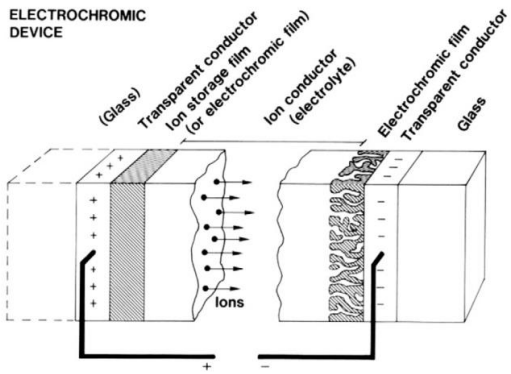

Figure 2.1. A five-layer electrochromic device [62].

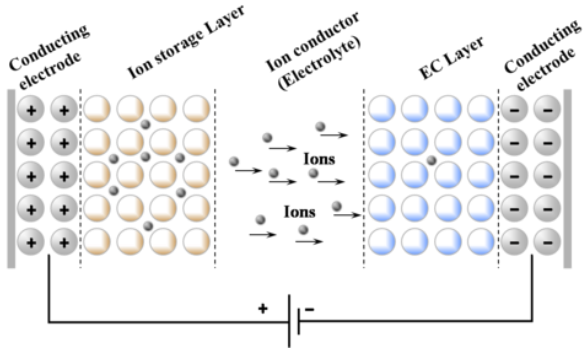

Figure 2.2. Cross-sectional view of the layers of a typical laminated electrochromic device [61], indicating transport of positive ions under the action of an electric field.

A good electrochromic window should have the following features:

1. Good transmittance modulation ability
2. Fast reaction speed
3. Stable performance over a large number of cycles
4. Long lifespan when operated by electric power and solar radiation
5. A good corrosion inhibition property at low or high temperatures, as well as against chemical corrosion
6. Low cost of preparation and maintenance
7. Can be produced on a large-scale.

Electrochromic devices that had been studied from 1993 to 1998 and 1998-2001were organized by Granqvist. Table 2.1 showed electrochromic devices based on inorganic electrochromic materials

from 1993 to 1998. Table 2.2 showed electrochromic devices based on organic and polymer electrochromic materials from 1993 to 1998. Table 2.3 showed electrochromic devices based on both inorganic and polymer electrochromic materials from 1998 to 2001. These tables showed researched electrochromic devices construction, their size, transmittance under bleached state and color state, number of color/bleach cycles, and switching time (τ_{sw}).

Table 2.1. Electrochromic devices based on inorganic electrochromic materials [55]. Data for inorganic electrochromic devices investigated 1993–1998, showing materials, sample size, modulation range for the transmittance (*T*), number of color/bleach (c/b) cycles, and switching time (τ_{sw}). G denotes glass, and the subscript for T signifies the wavelength (in nm) or the averaging over wavelength to obtain luminous (lum) and solar (sol) values.

Entry	Device construction	Size (cm^2)	*T* (%)	c/b (cycles)	τ_{sw} (s)
1	G/ITO/WO_3/SiO_2/Au	-	-	10^6	-
2	G/ITO/WO_3/$SbHP_2O_2 \cdot qH_2O$/Au	-	-	$> 10^4$	-
3	G/ITO/WO_3/$SB_2O_5 \cdot qH_2O$/IrO_2/ITO/G	-	-	$> 10^7$	-
4	G/ITO/WO_3/TiO_2/TiO_2-CeO_2/ITO/G	-	$18 < T_{550} < 58$	360	-
5	G/ITO/WO_3/$ZrP \cdot qH_2O$/ZrO_2/NiO/ITO/G	20	$17 < T_{550} < 75$	-	60
6	G/ITO/NiO/Ta_2O_5/WO_3/ITO	180	$12 < T_{lum} < 78$	$> 2\times10^4$	10
7	G/ITO/V_2O_5/$LiBO_2$/WO_3/Au	3	$3 < T_{815} < 38$	~100	-
8	G/SnO_2/WO_3/Li_2O-CeO_2-SiO_2/V_2O_5/Au	-	$9 < T_{sol} < 25$	-	10
9	G/ITO/WO_3/MgF_2/V_2O_5/Au	1	$\Delta T \approx 50$	-	-
10	G/ITO/V_2O_5/$LiBO_2$/WO_3/ITO	3	$13 < T_{lum} < 65$ $9 < T_{sol} < 58$	-	720
11	G/ITO/V_2O_5/$LiBO_2$-LiF/WO_3/ITO/MgF_2	3	$21 < T_{lum} < 60$ $13 < T_{sol} < 52$	2000	450
12	G/ITO/VO_2/$LiAlF_4$/WO_3/ITO	3	$10 < T_{sol} < 50$	> 1000	-
13	G/ITO/WO_3/$LiNbO_3$/$LiCoO_2$/In_2O_3	2	$12 < T_{550} < 65$	1.8×10^4	-
14	G/ITO/CrO_2/$LiBO_2$/WO_3/ITO/ZrO_2	16	$9 < T_{lum} < 74$	> 5000	30

Table 2.2. Electrochromic devices based on polymer- laminated electrochromic materials [55]. Data for laminated electrochromic devices investigated 1993–1998, showing materials, sample size and modulation range for the transmittance (T), number of color/bleach (c/b) cycles and the switching time (τ_{sw}). G denotes glass, P denotes polymer and the subscript for T signifies the wavelength (in nm) to obtain luminous (lum), and solar (sol) values.

Entry	Device construction	Size (cm^2)	T (%)	c/b (cycles)	τ_{sw} (s)
15	G/ITO/WO_3:Mo/PPSA-H/ITO/G	6	$8< T_{lum} < 58$ $7< T_{sol} < 46$	300	20
16	G/ITO/WO_3/PAMPS/PB/ITO/G	400	$5< T_{550} < 69$	2×10^4	60
17	G/ITO/PVA/PANI/ITO/G	-	$9 < T_{700} < 42$	-	1
18	P/ITO/WO_3/BPEI-H^+/FI/ITO/P	16	$25 < T_{lum} < 60$	-	20
19	P/ITO/WO_3-PMMA/BPEI-H^+/PANI/Au/P	2	$25 < T_{550} < 50$	-	-
20	G/ITO/WO_3/PMMA-Li^+/V_2O_5/ITO/G	25	$22 < T_{lum} < 73$ $14 < T_{sol} < 60$	-	60
21	G/ITO/WO_3/PMMA-Li^+/V_2O_5/ITO/G	64	$20 < T_{550} < 50$	-	5
22	G/ITO/WO_3/HEMA-NPG-Li+/PB/ITO/G	2025	$20< T_{lum}< 77$	10^5	120
23	G/ITO/WO_3/PMMA-PC-Li^+/NiO/ITO/G	-	$31 < T_{600} < 78$	10^4	-
24	G/ITO/$K_{0.3}WO_3$/PEO-PC-Li^+/ WO_3-NiO/ITO/G	9	$25 < T_{550} < 80$	-	5
25	G/ITO/WO_3/PVB-Li^+/TiO_2-CeO_2/ITO/G	100	$7 < T_{lum} < 81$ $4 < T_{sol} < 73$	5×10^4	60
26	G/ITO/WO_3/Silane-Li^+/TiO_2-CeO_2/ITO/G	1225	$20 < T_{380\text{-}800} < 80$	-	> 100
27	G/ITO/WO_3/GLYMO-TEG-Li+/SnO_2(Mo,Sb) /ITO/G	5	$25< T_{550} < 75$	500	30
28	G/ITO/WO_3/PMMA-PPG-Li^+/TiO_2-ZrO_2/ITO/G	5	$20< T_{550} < 80$	-	200
29	G/ITO/WO_3/PEO-Li^+/PODS/ITO/G	15	$9 < T_{lum} < 55$ $4 < T_{sol} < 34$	-	< 60
30	G/ITO/WO_3/PEO-ECH-Li^+/PPY-DDS/ITO/G	2	$30 < T_{700} < 60$	1.5×10^4	2
31	P/ITO/WO_3/PMMA-PC-Li^+/V_2O_5/ITO/P	-	$8 < T_{600} < 65$	3×10^4	-
32	G/ITO/dye-TiO_2/electrolyte/WO_3/ITO/G	-	$54 < T_{788} <70$	-	-

Table 2.3. Data for electrochromic devices investigated 1998–2001 [60], showing materials, sample size and modulation range for the transmittance (*T*), reflectance (*R*) and emittance (*E*). Also shown are the number of color/bleach (c/b) cycles and the switching time (τ_{sw}). G denotes glass, P denotes polymer and the subscript for T, R or E signifies the wavelength (in nm) or the averaging over wavelength to obtain luminous (lum), solar (sol) or thermal (therm) values. Optical density is denoted by OD, an antireflection layer is denoted by AR and c-WO_3 signifies a crystalline state of the oxide.

For some devices, no specification was given for the transparent electrical conductor (TC), ion conductor (IC) and counter electrode (CE) [60].

Entry	Device construction	Size (cm^2)	T (%)	c/b (cycles)	τ_{sw} (s)
1	G/ITO/NiO/Ta_2O_5/WO_3/ITO	2400	$18 < T_{lum} < 73$ $11 < T_{sol} < 55$	10^5	-
2	G or P/ITO/WO_3/Ta_2O_5/IrO_2/ITO	30	$18< T_{550} < 70$	3.5×10^4	-
3	G/ITO/WO_3/$LiAlF_4$/V_2O_5/ITO	900	$23< T_{lum} < 55$	-	-
4	G/TC/WO_3/IC–Li^+/CE/TC	-	$8< T_{lum} < 55$	-	150
5	G/ITO/WO_3/ZrP·qH_2O/ZrO_2/NiO/ITO/G	25	$38 < T_{lum} < 74$ $25 < T_{sol} < 53$	-	60
6	G/SnO_2/WO_3/PEO-H+/IrO_2/SnO_2/G	130	$10< T_{550} <48$	-	-
7	G/SnO_2/WO_3/PVSA–PVP–H^+/PB/SnO_2/G	155	$6 < T_{550} <72$	2×10^4	30
8	G/SnO_2/WO_3/PAMPS/PANI/SnO_2/G	8	$27< T_{550} <64$	-	26
9	G/ITO/WO_3/PAMPS/PANI–PB/ITO/G	2	$23< T_{sol} <73$	3700	30
10	P/ITO/WO_3/PMMA–PC–Li^+/V_2O_5/ITO/P	-	$8< T_{600} <65$	3×10^4	-
11	G/ITO/WO_3/PPY–Li^+/V_2O_5/ITO/G	-	ΔT_{788}=30	-	-
12	G/ITO/WO_3/PEO–Li^+/TiO_2/ITO/G	-	ΔOD=1	10^6	2
13	G/ITO/WO_3/PMMA–PPG–Li^+/TiO_2–ZrO_2/ITO/G	5	$20< T_{550} <80$	-	200
14	G/ITO/WO_3/Silane–Li^+/TiO_2–CeO_2/ITO/G	1225	$20< T_{380\text{-}800}<80$	-	>100
15	G/ITO/GLYMO–TEG–Li+/SnO2(Mo,Sb)/ITO/G	5	$25< T_{550} <75$	500	30
16	G/SnO_2/WO_3/Ormolyte–Li^+/SnO_2(Mo,Sb)/SnO_2/G	9	$20< T_{550} <60$	500	~100
17	G/SnO_2/WO_3/Ormolyte–Li^+/CoO–Li^+/SnO_2/G	9	$20< T_{550} <65$	-	-
18	G/SnO_2/Nb_2O_5:Li/Ormolyte–Li^+/SnO_2(Mo,Sb)/SnO_2/G	9	$20< T_{550} <70$	-	-
19	G/SnO_2/WO_3/PEGMA–PEO–Li+/NiO:Li/SnO_2/G	144	$27< T_{lum}<70$	-	~120
20	G/SnO2/WO_3/PVDF–Li+/NiO:Li/SnO_2/G	7	$2< T_{lum} <75$	-	-
21	G/ITO/WO_3/PMMA–PC–Li+/NiO/ITO/G	-	$31< T_{600} <78$	10^4	-
22	P/ITO/WO_3/PMMA–PPG–Li+/NiO/ITO/P	220	$35< T_{550} <70$	5000	~200
23	P/ITO/WO_3·H_2O/PVDF–HFP–Li^+/PANI/ITO/P	-	$2< T_{800} <12$	-	-
24	G/TC/WO_3/IC/C-dots/TC/G	25	$2< T_{lum} <55$	3×10^5	~20
25	G/TC/WO_3/IC/CE/TC/G	4800	$13 < T_{lum} < 58$ $7< T_{sol} < 37$	-	-
26	P/ITO/PEDT–PSS/PEPI–PEO–Li^+/PPY–DS–IC/ITO/P	-	$23< T_{640} <75$	-	4
27	P/ITO/PNNDMBP–PEPI–PEO/PEPI–PEO–Li^+/PET_2–PEPI–PEO/ITO/P	-	$27< T_{620} <64$	1000	7
28	G/ITO/PBEDOT–NCH_3C_z/PMMA–PC–Li^+/PEDOT–$C_{16}H_{33}$/ITO/G	-	$8< T_{650} <68$	10^4	1
29	G/ITO/dye-TiO_2/IC/WO_3/ITO/G	-	$54< T_{788} <70$	-	-
30	G/TC/WO_3/dye-TiO_2/IC/TC	25	$3< T_{lum} <8$	-	120

			2< T_{sol} <26		
31	P/ITO/dye-TiO_2/PEGMA–LiI/WO_3/ITO/P	8	30< T_{550} <40	-	-
32	G/TC/SiC:H/TC/V_2O_5:Li/$LiAlF_4$/WO_3/TC	16	8< T_{lum} <25	-	120
33	CaF_2 or Si/grid/c-WO_3/IC/CE/TC	-	40< R_{1000} <66	-	-
34	G/Al/WO_3/Ta_2O_5/c-WO_3/grid	-	40< E_{therm} <58	-	-
35	G/grid/WO_3/Ta_2O_5/c-WO_3/grid	-	64< E_{therm} <80	-	-
36	G/ITO/NiO/PAMPS–DMA–Li^+/c-WO_3/Si/AR	-	60< E_{therm} <68	-	-
37	G/ITO/WO_3/PAMPS–Li^+/PANI–CSA/grid/AR/ZnSe/AR	-	22< R_{12000} <65	900	9
38	G/ITO/NiO/PMMA–TFSI–Li^+/WO_3/grid/Si	11	56< E_{therm} <65	-	-

2.1.1. Transparent conducting layer

The transparent conducting layer in electrochromic devices is made of a kind of material that is optically transparent and electrically conductive. The transparent conducting layer is deposited to a transparent substrate, which can be either glass or plastic. The layer transmits an electrical current between the electrochromic film and the ion storage layer (film).

The material utilized to transparent conducting layers can be compounds with two or three kinds of metal or metal oxide. Their resistivity can be as low as 10^{-4} Ω cm. Thin films of ZnO, SnO_2, and In_2O_3, and their alloys can be utilized as transparent conducting layers [63]. Haacke found materials' electrical conductivity can be improved by doping these oxides, without any decrease in their optical transmittance [63]. Aluminum-doped ZnO (AZO), tin-doped In_2O_3 (ITO), antimony-doped SnO_2 (ATO), and fluorine-doped SnO_2 (FTO) are among the most used transparent conducting layers in modern technology [64]. Conducting polymers have also been studied [64, 65].

Currently, the most utilized TCO conductor is FTO glass, due to its high transmittance, low surface resistivity, and low cost. ITO glass is the most popular transparent conducting layer utilized by researchers because it has higher transmittance and lower surface resistivity. However, the cost of ITO glass is high, which hindered the wide utilization of ITO glass in the real industrial productions.

2.1.2. Electrochromic film layer

In an electrochromic device, an electrochromic film is coated on top of the transparent conducting layer. The electrochromic film layer is the core part of such devices. It is made of electrochromic materials, which are electrically sensitive. Their optical properties, such as color, transmittance, and reflectance, can be altered during an electrochemical reaction process. An electrochromic film can be switched between oxidized forms and reduced forms, which causes variations in its optical properties.

There are several promising electrochromic materials, including inorganic EC materials such as ZnO, WO_3, NiO, TiO_2, V_2O_5, and organic and polymer EC materials such as viologens, polyaniline (PANI), poly(3,4 ethylenedioxythiophene) (PEDOTs). Among all inorganic materials WO_3 have high coloration efficiency, quick response time and long life [66].

WO_3 is the most popular electrochromic material. Electrochromism of tungsten oxide is a complex phenomenon and its principle can be expressed as follows. Tungsten oxide has a cubic structure which is also described by "empty-perovskite" type structure formed by nanostructured WO_3. In octahedral structure atoms are shared at corners. The empty space which is available inside the cube is filled by an interstitial atom. In interstitial sites the guest ions can be inserted. Both amorphous and crystalline WO_3 thin films exhibit electrochromic coloration property due to ionic insertion [66].

The general electrochromic phenomenon of WO_3 is due to the formation of tungsten bronze (M_xWO_3) according to the following equation:

$$\underset{\text{(Bleached)}}{WO_3} + xM^+ + xe^- \Leftrightarrow \underset{\text{(Colored)}}{MxWO_3} \qquad (2.1)$$

where $0 < x < 1$, e^- denotes electrons, M^+ can be H^+, Li^+, Na^+, or K^+. M^+ is from the counter electrode (ion storage film), which is utilized as the balance ion. Ions with small ionic size can across the electrolyte layer easier and faster than ions with big ionic size. The fastest transport ions are protons. The others are much slower in comparison. K^+ is extremely large and slow. Lithium ion is favored in current commercial products.

The valence of the W element is +6 in the bleached state of WO_3. By contrast, the valence of the W element is reduced in the state of M_xWO_3, which shows a blue color.

WO_3 electrochromic film is a working electrode. Transmittance of WO_3 electrochromic film changes with regulation of applied electric power. WO_3 electrochromic film is transformed to M_xWO_3 film with different optical properties when it incorporates electrons and charge-balancing ions. The process is reversible. Granvquist pointed out that the reaction was a gross oversimplification. The thin films of practical interest were normally hydrous (i.e. contain hydroxyl groups and incorporated water molecules), and may deviate to some extent from the stated WO_3 stoichiometry. A detailed theoretical understanding of electrochromism depends on reliable theoretical modeling of the electronic structure of WO_3 and M_xWO_3. This modeling has advanced significantly during the past few years, but it is still not clear. Intercalation of H, Li, or Na in WO_3 leads to intricate structural changes that are not yet fully investigated and understood [67].

A potential is applied to the transparent conductors, which causes migration of ions, such as H^+ or Li^+, from the ion storage layer, through the ion conducting layer, to the electrochromic layer. As a result, a redox reaction occurs, and the transmittance of the electrochromic window is switched. When the process is reversed, voltage is reversed, causing the ions to migrate back, and resulting in the transmittance of the electrochromic window to switch back to its previous state.

One of the main advantages of electrochromic windows as a kind of smart window is that it requires low-voltage power for switching to take place. In addition, there is no requirement for power to maintain the electrochromic property in any switched state.

The performance of the electrochromic film is determined by its material and the coating method. There are many kinds of electrochromic materials, and they can be divided into two groups based on the transfer direction of electrons. One group comprises cathodic electrochromic materials (colors under charge insertion). The other group comprises materials that exhibit anodic electrochromic (colors under charge extraction). Anodic electrochromic materials can complement cathodic electrochromic materials [62]. Electrochromic materials are discussed further in Section 2.2.

2.1.3. Electrolyte layer

In an electrochromic device, the electrolyte layer works as an ion conductor. It separates the electrochromic film and counter electrode layer. The electrolyte layer can be in the form of a liquid, solid, or gel. The layer should have high ionic conductivity and low electrical conductivity. Its ionic conductivity should be more than 10^{-4} S/cm, and its electrical conductivity should be less than 10^{-12} S/cm. In addition, for electrochromic windows, the electrolyte layer should have high transmittance and good durability under solar radiation [55, 67, 68].

Liquid electrolytes have many advantages, including, for example, high ionic conductivity, high transmittance, easily prepared, easily filled into the electrochromic device, and low cost. Liquid electrolytes are widely utilized in research work on electrochromic technology.

There are three types of liquid electrolytes: aqueous solution, organic solution, and IL electrolyte. However, aqueous solution and organic solution electrolytes have the potential risk of dangerous leakages in electrochromic devices. Therefore, in recent years, IL electrolyte is investigated to utilize as an ion conductor in electrochromic devices, for example, electrochromic smart windows.

Aqueous solution electrolytes can be acidic electrolytes (e.g. H_2SO_4 aqueous solution) [69], alkaline electrolytes (e.g. KOH aqueous solution) [70], or neutral electrolytes (e.g. KCl aqueous solution) [69, 71]. Aqueous solution electrolytes are investigated and utilized wildly in electrochromic materials and devices. However, due to their potential risk of leakages and their high melting point (around 0 °C), their utilization in electrochromic windows is not preferred.

Organic solution electrolytes are organic solvents with salts. The organic solvents include dimethyl carbonate (DMC), ethylene carbonate (EC), ethyl methyl carbonate (EMC), which have the disadvantage properties as follows: (1) Flammable; (2) High vapor pressure; (3) Low thermal and chemical stability; (4) Toxic problem; (5) Leakage problem. Due to the disadvantageous properties of organic solvents, a lot of research was performed to replace organic electrolytes in commercial devices.

Ionic liquids (ILs) can be utilized as electrolytes (ion conductor) in electrochromic devices [72]. ILs are salts that are liquid at temperatures below 100 °C. ILs with liquid status at room temperature are called room temperature ILs. ILs are composed of cations and anions, of which there are many types. In theory, there are 10^{18} ILs that can be designed and synthesized. Many ILs are transparent. This means that there are many ILs that can be selected as ion conductors for electrochromic smart windows, which will enlarge the selective range of ion conductors for electrochromic devices. ILs ion conductors can also result in the development of electrochromic smart windows. Compared with conventional solvents, ILs have many advantageous properties: (1) low vapor pressure, high thermal and chemical stability; (2) favorable solubility in a wide range of inorganic and organic chemicals; (3) polarity is able to be modulated in a broad range; (4) phase behavior of ILs may be controlled and/or optimized by polarity modulation; and (5) wide chemical and functional groups. Due to the advantageous properties of ILs, they have been investigated and utilized in many fields: CO_2 capture and storage, catalysis, nanoscience, biotechnology, and cellulose science. Furthermore, some ILs are suitable to be utilized as electrolytes in electrochromic devices due to their favorable properties, including good ionic conductivity, wide electrochemical stability windows [72], high thermal stability, low melting point, non-flammable, low vapor pressure. Due to these advantages, the utilization of ILs can improve the performance of ion conductors in electrochromic devices. Actually, several groups in the world have utilized ILs as ion conductors to produce electrochromic devices. For example, Neto *et al.* reported electrochromic behavior of WO_3 thin films in H_2SO_4 aqueous solution and a protic ionic liquid N-methyl-pyrrolidinium tetrafluoroborate [73]. The results showed that PIL as electrolyte, instead of H_2SO_4, can improve all electrochromic parameters, including the cyclic durability that was higher in this medium. The work of Neto *et al.* suggests that protic IL can be utilized as an electrolyte in electrochromic devices [73]. Therefore, in this Ph.D. project, ILs are investigated to utilize as ion conductors for electrochromic smart windows.

Solid electrolytes include polymer solid electrolytes and inorganic solid electrolytes. Polymer solid electrolytes can be used to coat flexible films. Furthermore, they have good adhesion to electrochromic layers and counter electrode layers. By contrast, polymer solid electrolytes are

normally constructed with lithium salt dispersed into a polymer, such as poly(methyl methacrylate) (PMMA) and poly(ethylene oxide) (PEO).

The electrolyte layer should enable fast ion transfer, be transparent, and have good durability under solar radiation. It is still hard to find electrolytes that meet all the requirements for electrochromic devices, which means the performance of such devices is limited.

2.1.4. Counter electrode layer

The counter electrode layer in an electrochromic device is also known as an ion storage layer. The function of an ion storage layer is either to store ions or provide ions to the electrochromic film layer, in order to achieve charge balance. The counter electrode layer needs to have high transmittance when the electrochromic layer is in a bleached state. A fast chemical response speed and sufficiently high ionic storage space are necessary properties of a counter electrode layer.

There are two types of counter electrode layers. One type has no color change during the process of insertion and extraction of ions. CeO_2-TiO_2 is utilized in the ion storage layer because it has high transmittance and good cycle stability. However, its chemical response speed is slow, and the ionic storage space is limited. The other type of counter electrode layer is also an electrochromic layer. The counter electrode material has the opposite color changing property to the electrochromic working electrode layer. For example, the counter electrode can utilize an anodic color changing material (e.g. NiO), when the electrochromic layer in an electrochromic device is a cathode color changing material (e.g. WO_3). The counter electrodes variously employ V_2O_5, TiO_2 with or without additions of ZrO_2 or CeO_2, SnO_2 doped with Mo and Sb, CoO deposited with Li, and NiO deposited with or without Li [62].

2.2. Electrochromic materials

Electrochromic film is the most important functional part of an electrochromic device. The utilized electrochromic materials and the film preparation method will influence the properties of electrochromic film. There are many types of electrochromic materials, including organic and inorganic materials. According to their colored principle, they can also be divided into anodic coloration and cathodic coloration electrochromic materials. Some types of electrochromic materials are introduced in the following sections (2.2.1.–2.2.3.).

2.2.1. Transition metal oxides

Transition metal oxide electrochromic materials include oxidation states of transition metal element Ti, V, Cr, Mn, Fe, Co, Ni, Cu, Nb, Mo, Rh, Ta, W, and Ir (Table 2.4). They can be divided into anodic coloration electrochromic materials and cathodic coloration electrochromic materials, according to whether the applied voltage is positive or negative.

Table 2.4. Summary of the key features of the main electrochromic oxides, including oxide type, coloration type, and whether transparency can be achieved [55].

Oxide type	Coloration type	Transparency
TiO_2	cathodic	Yes
V_2O_5	cathodic/anodic	No
Cr_2O_3	anodic	No
MnO_2	anodic	No
FeO_2	anodic	No
CoO_2	anodic	No
NiO_2	anodic	Yes
Nb_2O_5	cathodic	Yes
MoO_3	cathodic	Yes
RhO_2	anodic	?
Ta_2O_5	cathodic	Yes
WO_3	cathodic	Yes
IrO_2	anodic	Yes

2.2.2. Prussian blue

Prussian blue (PB) is a dark blue pigment; its molecular formula is $C_{18}Fe_7N_{18}$ Electrochromic film made with Prussian blue has good electrochemical stability, especially in a solution with a pH of 2 to 3. A lower pH value is conducive both to enhancing the stability of PB and to improving its color change speed. PB was used in a laboratory at Gesimat (GmbH), Berlin, to prepare an electrochromic device with tungsten oxide [74]. The device is shown in Figure 2.3. However, the Gesimat GmbH Glass manufacturer has been permanently closed. Germany PB was also utilized to prepare all-solid-state electrochromic devices [75].

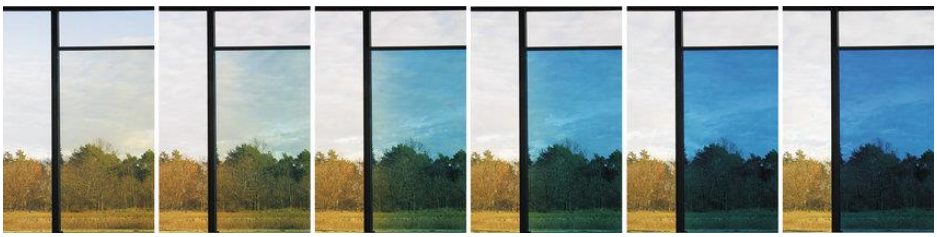

Figure 2.3. Six different coloration states of a complementary electrochromic device with electrochromic layers made with tungsten oxide and Prussian blue [74].

2.2.3. Organic electrochromic materials

Organic electrochromic materials include polyaniline [76], polypyrrole [77], polymerized polythiophene [78, 79], violet, and carbazoles [80]. Organic electrochromic materials can be designed according to requirements. They exist in many colors. Figure 2.4 shows some isophthalate-based electrochromic materials [81].

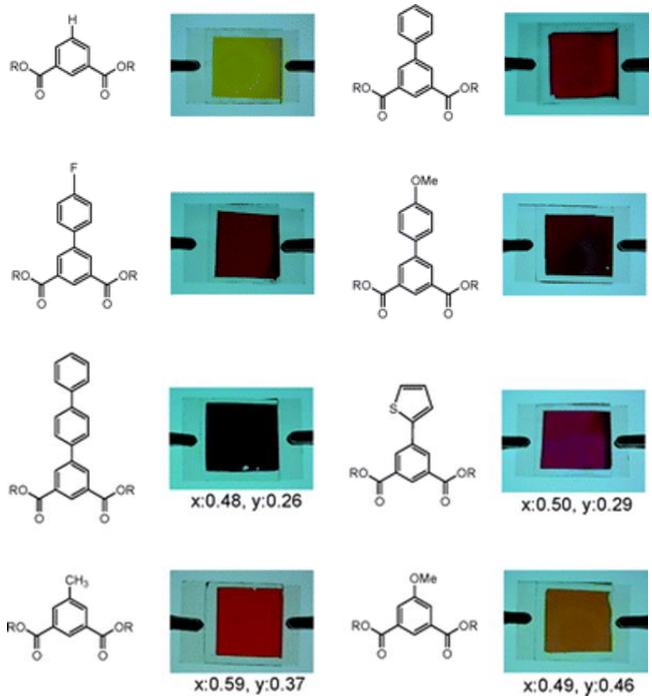

Figure 2.4. Some organic electrochromic materials based on isophthalate [81].

2.2.3.1. Polyaniline

Electrochromic devices composed of polyaniline can stably change between yellow and green. In addition, when some other materials (generally with electrochromic properties) are added during polyaniline preparation, the prepared composite materials will often have better electrochromic properties than pure polyaniline [76].

2.2.3.2. Polypyrrole

Polypyrrole [77] is a conductive polymer that has long been studied. It can transform between blue-violet, yellow-green, and pale colors. Pure polypyrrole film has a single color, low transparency, and poor chemical stability. Furthermore, the bonding force with the substrate is not strong.

2.2.3.3. Polythiophene

The original color of polythiophene film is red. The oxidized state is blue, and it can be reversibly changed between red and blue. Due to the diversity and optical properties of polythiophene's functionalized substituents and its controllable structure, polythiophene has become a promising electrochromic material with different substituents [78, 79]. Such as 3,4-Ethylenedioxythiophene (EDOT) is the organosulfur compound with the formula $C_2H_4O_2C_4H_2S$. The molecule consists of thiophene, substituted at the 3 and 4 positions with an ethylene glycol unit. It is a colorless viscous liquid [82]. EDOT is the precursor to the polymer PEDOT, which is sky blue when oxidized, and nearly opaque at reduced states. It is found in electrochromic displays, photovoltaics, electroluminescent displays, printed wiring, and sensors [83].

2.3. Methods to prepare electrochromic WO_3 film

Electrochromic films can be prepared by many methods. The different methods influence the microphysical structure of prepared electrochromic films, and therefore the films will have different electrochromic properties, such as transmittance modulation ability, response time, and durability [66]. The main methods used in electrochromic WO_3 film preparation are hydrothermal synthesis [84], electro-deposition [85], electron beam evaporation [86], thermal evaporation [87], sol-gel [88]and magnetron sputtering [89, 90]. All of these methods have their advantages and disadvantages. Their selection strongly depends on the required application and fabrication facility.

2.3.1. Vacuum evaporation method

The vacuum evaporation method is one type of physical vapor deposition (PVD). In this technology, the substrate and a source of the material to be deposited are located inside a vacuum chamber. The vacuum is required in order to allow the molecules of source material to evaporate freely in the chamber, and therefore to be deposited on all surfaces. The source material is then heated until it boils and evaporates. There are electro-beam (e-beam) evaporation and resistive evaporation, two technologies are based on this principle. Different materials use different methods to heat the source material. According to a material's phase transition properties, an evaporation method can be used for heating the source material [91].

The vacuum evaporation method is utilized for all-solid-state electrochromic devices. High temperature is utilized to vaporize the material and deposit it onto the cool substrate surface in a high vacuum environment to form film. For example, WO_3 film was prepared using vacuum evaporation method by Li *et al.* [92]. They report that all-solid-state ECDs glass/ITO/NiO/ZrO_2/Li/WO_3/ITO with different Li thickness were prepared by evaporation method. The layer NiO, ZrO_2, WO_3, ITO were

coated by e-beam power, while the Li layer was coated by resistive evaporation. Rao *et al*. [93] and Joraid *et al.* [94] also prepared WO_3 film by e-beam coating technology .

In addition, heat treatment can be carried to prototype of films. Agrawal and Habibi [95] report effect of heat treatment on structure, composition and electrochromic properties of evaporated tungsten oxide films. They reported that at 290 °C most of the hydroxyl groups condensed and then the water formed during this reaction was expelled. As this dynamic heating experiment was continued the film started to crystallize. This crystallization was complete by 350°C. While Beydaghyan *et al.* [96] prepared WO_3 films with the technique of glancing angle deposition (GLAD) in a thermal evaporation chamber. After deposition, samples were heated in a ceramic oven at 400 °C for 1 h under atmospheric pressure.

In this thesis, heat treatment was carried to sputtered films. The heat treatment was carried in a furnace oven at temperature 400 °C for 5 hours.

2.3.2. Magnetron sputtering method

Magnetron sputtering method is widely utilized for electrochromic thin film preparation. Magnetron sputtering is a high-rate vacuum coating technique that allows the deposition of many types of materials, including metals, alloys, compounds, and ceramics, onto as many types of substrate materials by the use of a specially formed magnetic field applied to a diode sputtering target.

In the magnetron sputtering coating process, a negative voltage of typically -300 V or more is applied to the target. This negative voltage attracts energetic positive ions of inert gases (e.g., argon (Ar), helium bombarded to the target surface. These high-energy ions collide strongly with the target metal, causing the target atom or molecular particles to fly into the sputtering chamber. These particles are deposited on the substrate material to form required films. The gas inside the chamber is either Ar or Ar + O_2. High pressure is applied to the chamber during the magnetron sputtering coating process [97, 98].

There are direct current (DC) sputtering and radio frequency (RF) sputtering - two ways of the magnetron sputtering process. The power source of DC sputtering is the direct current. Its chamber pressure is usually from 1 to 100 mTorr. The targets of DC sputtering are electrically conductive materials. Such as pure metal sputtering targets, Iron (Fe), Copper (Cu), Nickel (Ni), Tungsten (W). Metal oxide films can also be prepared by DC sputtering with pure metal target and supplied oxygen in the chamber. WO_3 films were prepared by reactive DC sputtering from a tungsten target by Chananonnawathorn *et al* [99]. In their experiment, the total pressure during deposition was 10 mTorr, sputtering power was 200 w. The WO_3 films with thickness of 50 to 500 nm were prepared under two conditions of the oxygen flow rates from 5 to 20 sccm with fixing argon flow rate at 5 sccm. The

result showed that the WO_3 films were of poor crystallinity or amorphous structure, which have better electrochromic properties than crystal structure. The WO_3 films deposited at low oxygen gas flow rate and high film thickness are found to exhibit better electrochromic properties.

Compared with DC sputtering, RF sputtering has a wider range of applications and is suitable for both conductive and non-conductive materials. However, it is most commonly used for depositing dielectric sputtering target materials. The power source of RF sputtering is alternating current. The power supplied is a high voltage RF source, which is often fixed at 13.56 MHz. RF peak to peak voltage is 1000 V, electron densities are 109 to 1011 cm^{-3}, and the chamber pressure is from 0.5 to 10 mTorr. The deposition rate of RF sputtering is lower compared with DC sputtering. It is normally used for smaller substrate sizes due to the high cost [100]. Kalagi *et al.* prepared WO_3 thin films by RF sputtering method using a WO_3 target. Both oxygen and argon are supplied during the sputtering process, and the ratio of oxygen to argon is 40%: 60% [89]. Meenakshi *et al.* prepared V_2O_5 mixed WO_3 thin films by RF sputtering method utilizing their self-made V_2O_5 mixed WO_3 targets with various compositions [101]. During sputtering they only used high-purity argon and did not use oxygen. RF magnetron sputtering is the approach that has proved to enhance the durability of the electrochromic films [59].

Generally, many of the groups moved to reactive RF sputtering and reactive D C sputtering of metal targets. The reason being the rate of deposition is much faster than with ceramic targets. In this thesis, the WO_3 thin films were prepared by radio frequency (RF) method with WO_3 as target. In the future, I plan to prepare electrochromic WO_3 films using reactive RF or DC sputtering with W target instead of WO_3 target, and oxygen will be provided during the sputter process.

2.3.3. Electrochemical deposition method

The electrochemical deposition method involves the use of three electrodes (working electrode, counter electrode, and reference electrode) in the precursor solution. An external electric field is applied to the solution to make the corresponding anions and cations move to the positive and negative electrodes respectively. The electrode undergoes an oxidation-reduction reaction in this electrochemical deposition method. For example, WO_3 films were prepared by deposition from a solution of tungsten chloride by Habib *et al.* [102], and Deepa *et al.* prepared WO_3 electrochromic thin films by surfactant mediated electrodeposition [103].

2.3.4. Sol-gel method

The sol-gel method disperses highly active raw materials, such as metal alkoxides and chlorides, in a solvent. Hydrolysis and condensation reactions obtain a precursor sol that is stably dispersed in the solution, and then drop the precursor sol onto the substrate. Finally, scraper, spin coating, spraying,

lifting, and other film forming techniques are utilized for film formation in this method. WO_3, TiO_2, SiO_2, Ta_2O_5, Al_2O_3 and ZrO_2 thin film can be prepared using sol-gel method [104]. Dip-coating, spin-coating, doctor blade and spraying are methods used for thin film preparation using sol-gel method.

2.3.5. Hydrothermal and solvothermal method

In the hydrothermal and solvothermal method, seed crystals are obtained by using precursor solution via a chemical reaction under certain temperature and pressure. With further chemical and/or physical interaction, seed crystals become various nanostructures. Vankova *et al.* prepared WO_3 thin films by hydrothermal method [105].

2.4. Performance requirements for electrochromic smart windows

To accomplish specific energetic and environmental tasks in buildings, large area electrochromic windows must exhibit acceptable levels in specific performance indicators. These parameters concern a number of electrical, thermal and optical properties which depend on the structural composition and configuration of the electrochromic device [106].

2.4.1. Switching voltage

The application of a switching voltage is required to initiate the coloration process, i.e. charge transfer in the constituent layers of the EC device. The potential level depends on the electronic conductivity and ionic diffusivity of the component substrate. Low voltage drop along the electrode surface is usually obtained by using transparent electronic conductors with low sheet resistivity, while high ionic diffusivity ($>10^{-4}$ S cm^{-1}) is usually achieved by using conductive materials with dissolved conductive materials such as gold nano- particles [107]. These properties are essential to achieve low switching voltages and to increase the commutation speed of the device between its extreme switching states, the so-called “switching speed” [106] .

2.4.2. Switching time

The switching time (τ) for coloration and bleaching is defined as the time the EC glazing takes to reach 90% respectively of its maximum and minimum transmittance level.

2.4.3. Optical density

Optical density (OD), also referred to as absorbance (A), is a property that describes a material’s ability to absorb the power of a given light (called “radiant power”) that is passed through that material. It is defined as a ratio between the incident radiant power (the power of the light as it hits the material) and the transmitted radiant power (the power of the light as it exits the material). In

other words, optical density is the ability of a material to block a particular light. The *optical density* or *absorbance* of a material is a logarithmic intensity ratio of the light falling upon the material, to the light transmitted through the material:

$$\Delta A(\lambda) = \Delta \mathrm{OD}(\lambda) = \log\left(\frac{\mathbf{I_0}}{\mathbf{I_b}}\right) - \log\left(\frac{\mathbf{I_0}}{\mathbf{I_c}}\right) = \log\frac{\mathrm{Tb}}{\mathrm{Tc}} = \eta Q \qquad (2.2)$$

where I_0 is the intensities of the incident lights, η is coloration efficiency, T_c and T_b are transmittance values of electrochromic films at color state and bleached stated, respectively, Q is the integration of the current versus the coloration time, and λ denotes the certain wavelength.

2.4.4. Coloration efficiency

Coloration efficiency (η) is defined as the change in optical density (OD) per unit of charge (Q) intercalated into or extracted from the EC film. A high coloration efficiency means that the device provides a large optical modulation range with a small charge intercalation or extraction. It can be calculated according to the following formulas:

$$\eta(\lambda) = \frac{\Delta \mathrm{OD}(\lambda)}{\mathrm{Q}} = \log\left(\frac{Tc}{Tb}\right)/Q \qquad (2.3)$$

where T_b and T_c represent the transmittance in bleached and colored states, respectively. Q is the integration of the current versus the coloration time, and λ denotes the certain wavelength [89, 90].

2.4.5. Cycle numbers

When an electrochromic material or device is continuously cycled between a colored state and a bleached state, the material or device eventually fails due to degradation in performance. The cycle number of an electrochromic material or device is the maximum number of cycles that can be used before failure.

2.5. Objectives and scope of the thesis

The main objective of this thesis is to investigate electrochromic nanofilms and ionic liquid ion conductors to make electrochromic devices for electrochromic smart window development. Electrochromic film and ion conductor are two main parts in the structure of an electrochromic device. Therefore, in this thesis, electrochromic tungsten oxide (WO_3) nanofilm and ionic liquid ion

conductor were prepared and characterized to make electrochromic devices for further electrochromic smart windows applications.

Electrochromic WO_3 thin films were prepared and characterized in this thesis. Firstly, the sputtering method was used to prepare thin WO_3 films. The films' thickness was controlled during the preparation process. Films with thickness of 36 nm, 72 nm, 108 nm, 144 nm, 180 nm were prepared by RF sputtering method. Their microphysical structure and electrochromic properties were investigated. Films' thickness might influence the performance of WO_3 films prepared in this work. Furthermore, effect of oxygen during AJA sputtering and effect of heat treatment on sputtered samples was investigated. Increased oxygen content during RF sputtering process and heat treatment might influence the performance of the prepared WO_3 films. Sputtering method has the advantages as follows for WO_3 film preparation, magnetron sputtering provides significant diversification in deposition and permits to deposit preferred morphology, design and structures by merely altering the main deposition parameters. (1) Film thickness can be easily controlled at nano scale; (2) The ratio of gas, such as oxygen can be alter based on request; (3) Repeatability of this method is good. Therefore, in this thesis, RF sputtering method is utilized for WO_3 film preparation.

In addition, ILs were prepared, characterized and utilized to make electrochromic devices for further electrochromic smart windows applications. Thermal properties of ILs, including thermal conductivity and thermal diffusivity, are measured. Physical and chemical properties of ILs are important when ILs are utilized as electrolytes. Density, viscosity, heat capacity, thermal stability, ionic conductivity, and electrochemical window of IL-based electrolytes were investigated. Due to advantageous properties of ILs, they can be utilized as electrolytes in electrochromic devices. IL based electrolytes have the potential to replace the aqueous electrolyte in electrochromic devices due to their thermal and electrochemical properties. IL based electrolytes can improve the cycle number of electrochromic devices. Hence, ILs are promising to be utilized as ion conductors to make electrochromic devices for further electrochromic smart windows applications.

Chapter 3. Research Methodology

3.1. Materials

The main chemicals and materials utilized during the experiments were as follows. The WO_3 sputtering target (diameter 5.08 cm, thickness 0.32 cm) was purchased from AJA International Inc., USA. Substrates for the growth of WO_3 thin films were ITO (tin-doped indium oxide, $In_2O_3(Sn)$) glass slides were purchased from Sigma-Aldrich; they had a transmittance of ca. 86% at 550 nm, a surface resistivity of ca. 70-100 Ω/square, and their dimensions were ca. 25 mm × 25 mm × 1.1 mm. When performing CV analysis ITO glass slides were cut into small pieces, with size of ca. 9.2 mm × 25 mm × 1.1 mm. Reagent grade sulfuric acid (H_2SO_4, 96 wt%) and potassium chloride (KCl, 99%) were purchased from Sigma-Aldrich. Distilled water was utilized throughout the experiments. Ag/AgCl reference electrode (3M KCl aqueous solution) were purchased from Metrohm.

3.2. Preparation of electrochromic WO_3 thin films

3.2.1. Sample preparation instruments

The instrument utilized during sample preparation was the E-Beam evaporator & Sputter AJA. Instrument model is: ATC-2200V (AJA International Inc., USA). The instrument utilized for sample heat treatment was a chamber furnace, model ELF 11/14B with E301Carroite controller (Carbolite Geron Ltd., UK).

3.2.2. Sputtering process

WO_3 films with thickness of 36 nm were prepared by the RF magnetron sputtering technique using an AJA sputter and evaporator. First of all, install WO_3 sputtering target into the AJA sputter and evaporator. Then check the sputter rate under the following sputter condition. The sputter rate was checked as 0.05 nm/s. Prior to the sample sputtering process, ITO glass was used as a substrate and loaded into the sample holder. The sputtering parameters were as follows: Open argen (Ar) flow as 67 sccm (standard cubic centimeter per minute). Plasma strike pressure was set at 30 mTorr (≈ 4.0 Pa) Ar pressure. Strike the target by going to 50 W. The pressure was changed and maintained at 3 mTorr (≈ 0.4 Pa) after the plasma was struck. The RF power was increased and kept at 120 W during sputtering. The ramp up rate was 1/3 W/s (Ramp up time was set at 210 s for RF power increasing from 50 W to 120 W). After the power reached the set value, 1 minute was spent waiting for the plasma to stabilize. Thereafter, the shutter that covered the target was opened and kept open for 720 s.

Finally, the shutter was closed to stop more material being deposited on the substrate. The films had an expected thickness of 36 nm. In the end, the power was ramped down to 50 W and then was turned off.

3.2.3. Heat treatment temperature optimization

WO_3 films with thickness of 36 nm were prepared by the RF sputtering technique under heat treatment. The following experiments were performed to determine the suitable temperature for heat treatment.

Firstly, WO_3 films with thickness of 36 nm were prepared by the RF sputtering technique, as shown in Figure 3.1. Subsequently, they were put into a chamber furnace and heated for 5 hours at temperatures of 100°C, 200°C, 300°C, 400°C, 500°C, and 600°C, respectively. The rate of temperature rise (i.e. temperature ramp rate) was 10°C/minute. The transmittance value of the samples was investigated using UV-VIS-NIR spectroscopy. The 36 nm WO_3 was coated on clear substrate without an ITO film on top.

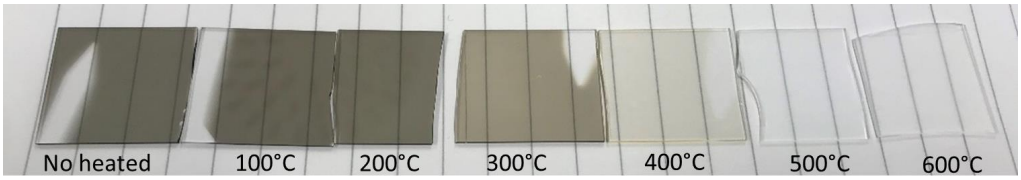

Figure 3.1. Samples of 36 nm WO_3 on top of clear substrate before and after heat treatment for 5 hours at temperatures of 100°C, 200°C, 300°C, 400°C, 500°C, and 600°C, respectively.

As shown in Figure 3.2, the transmittance value increased with increases in heat treatment temperature from 100°C to 400°C. However, it decreased with heat treatment temperature increases from 400°C to 600°C. A possible reason is that large crystals were formed when the temperature was higher than 400°C. Large crystals are not good for electrochromic modulation, and therefore we chose 400°C as the heat treatment temperature for subsequent experiments, which are described as follows.

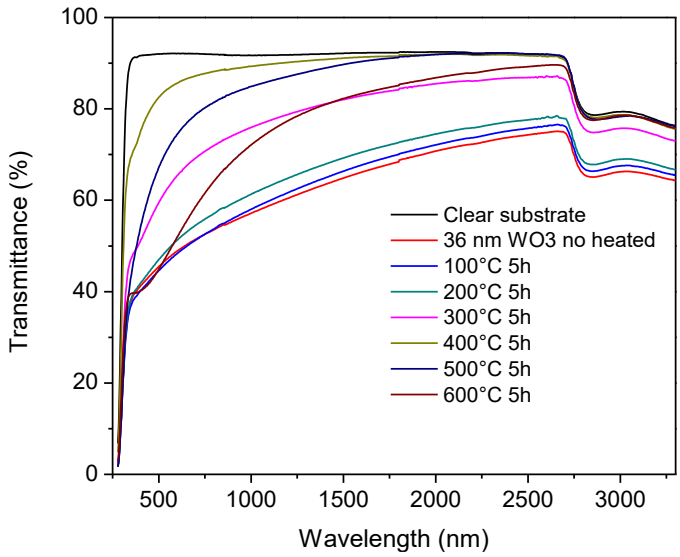

Figure 3.2 Transmittance spectra of 36 nm WO_3 on top of clear substrate before and after heat treatment for 5 hours at temperatures of 100°C, 200°C, 300°C, 400°C, 500°C, and 600°C, respectively.

Transmittance values obtained at wavelengths of 555 nm and 507 nm were compared, as shown in Figure 3.3. The transmittance value obtained at a wavelength of 555 nm was higher than the transmittance value obtained at a wavelength of 507 nm. The transmittance value order of samples obtained from a wavelength of 555 nm was the same as the transmittance value order of samples obtained from a wavelength of 507 nm.

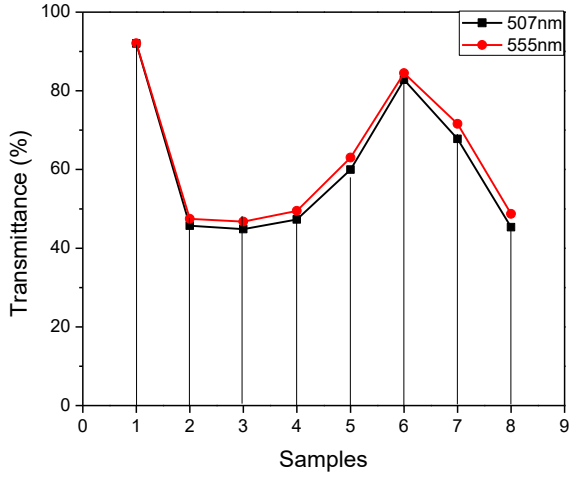

Figure 3.3 Transmittance values of Samples 1–8. 1 represents sample of plain glass, 2 represents samples of 36 nm WO_3 on top of glass before heat treatment, and 3–8 represent samples of 36 nm WO_3 on top of glass after heat treatment for 5 hours at temperatures of 100°C, 200°C, 300°C, 400°C, 500°C, and 600°C, respectively. Transmittance values were measured at wavelengths of 555 nm and 507 nm.

3.2.4. Heat treatment method

Samples of 36 nm WO_3 films deposited on top of ITO glass by RF sputtering were heated in a chamber furnace at 400°C for 5 hours. The starting temperature was 20°C. The temperature ramp rate was 10°C/minute. The prepared WO_3 thin films are shown in Figure 3.4.

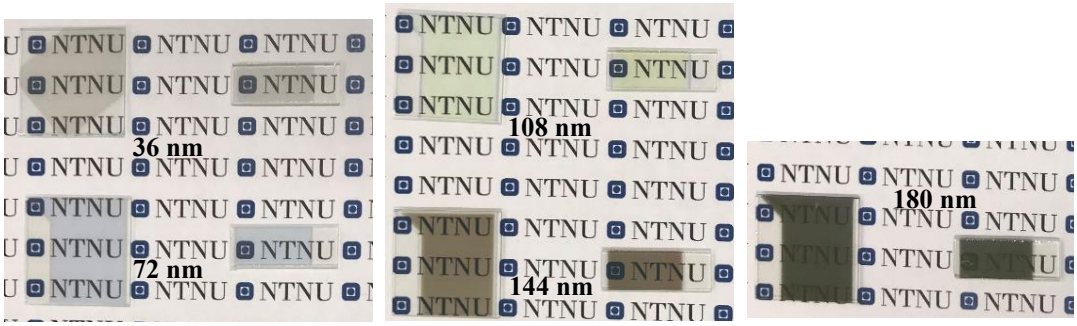

Figure 3.4 Prepared WO_3 thin film samples after heat treatment with thickness of 36 nm, 72 nm, 108 nm, 144 nm, and 180 nm.

3.3. Characterization

3.3.1. X-ray diffraction (XRD) analysis of samples

As-prepared samples were collected on a D8 A25 Davinci X-ray Diffractometer (Bruker, Germany) with Cu−Kα radiation. XRD data were collected in the range of 15–75° with a step size of 0.013°. The structures of the samples were analyzed using DIFFRAC.EVA V4.2 software (Bruker AXS, Germany).

It is shown that peaks shown on the "a" plot in Figure 3.5 (ITO glass original) is almost identical to peaks shown on the "b" plot in Figure 3.5 (ITO glass after heat treatment at 400°C for 5 hours), which means that heat treatment at 400 °C for 5 h will not change the structure of ITO glass. Therefore, the new peaks shown on the "d" plot in Figure 3.5 (36 nm WO_3 film after heat treatment at 400°C for 5 hours) are not due to the transformation of the ITO substrate. Furthermore, the peaks shown on the "c" plot in Figure 3.5 (newly formed 36 nm film before heat treatment) is almost identical to the peaks shown on the "a" plot in Figure 3.5 (ITO glass original), which means that there are no peaks relating to new coated WO_3 film. Therefore, WO_3 films deposited on the ITO glass were probably amorphous. Moreover, this means that the new peaks in curve d are from the WO_3 film after heat treatment. The new peaks are from the crystallization of WO_3 film during heat treatment.

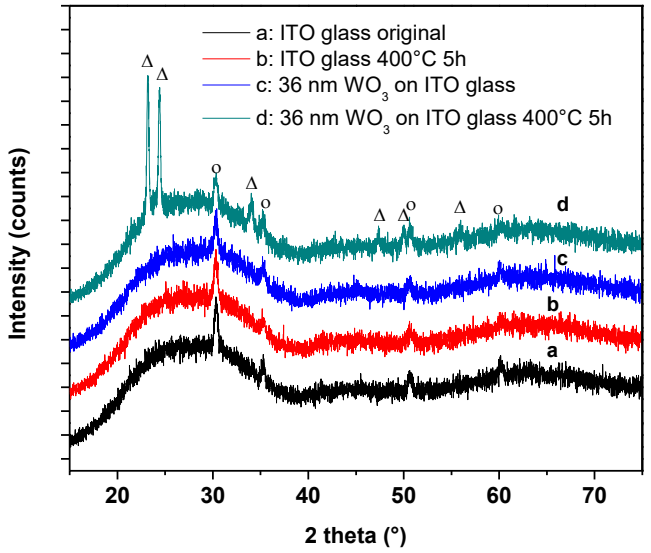

Figure 3.5. XRD analysis results of samples: (a) ITO glass original, (b) ITO glass after heat treatment at 400°C for 5 hours, (c) newly formed 36 nm film before heat treatment, and (d) 36 nm WO_3 film

after heat treatment at 400°C for 5 hours. Open circles (o)denote the reflections of ITO (PDF 04-019-3926). Open triangles (Δ) denote the reflections of monoclinic WO_3(PDF 00-043-1035).

The XRD signal for 36 nm WO_3 films was very weak because the film was too thin. Therefore, WO_3 film with thicknesses of 72 nm, 108 nm, and 180 nm were prepared to enhance the signal so that the structure of the prepared WO_3 film could be determined. The XRD curves (a–d) in Figure 3.6 are similar, which means that the WO_3 crystal structure was not changed when the film thickness increased from 36 nm to 180 nm. The peaks are clear with increases in thickness.

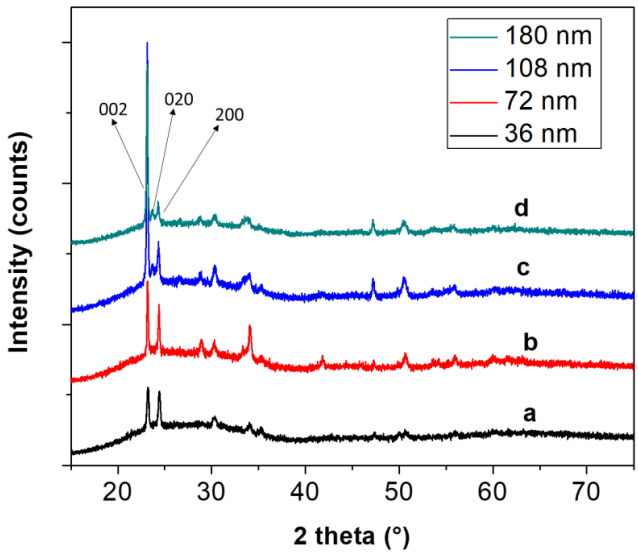

Figure 3.6 XRD results of prepared WO_3 thin films. (a) 36 nm (b) 72 nm (c)108 nm (d) 180 nm.

WO_3 thin film with thickness of 180 nm had the clearest signal peaks, as shown in Figure 3.6d. The peaks at 23.1º, 23.6º, and 24.4º could be assigned to (002), (020), (200) reflections of the monoclinic WO_3 (PDF 00-043-1035), respectively.

3.3.2. Field emission scanning electron microscopy (SEM)

The surface topography of the samples was captured by SEM (Thermo Fisher Scientific, USA). The results are shown in Figure 3.7. As shown in Figure 3.7(a), the newly sputtered film before heat treatment had a flat, smooth surface. As shown in Figure 3.7(b), after heat treatment, ice-like WO_3 crystals were formed. Therefore, the results show that heat treatment can cause a transition of the crystalline phase from amorphous to monoclinic for the RF sputtered WO_3 thin films.

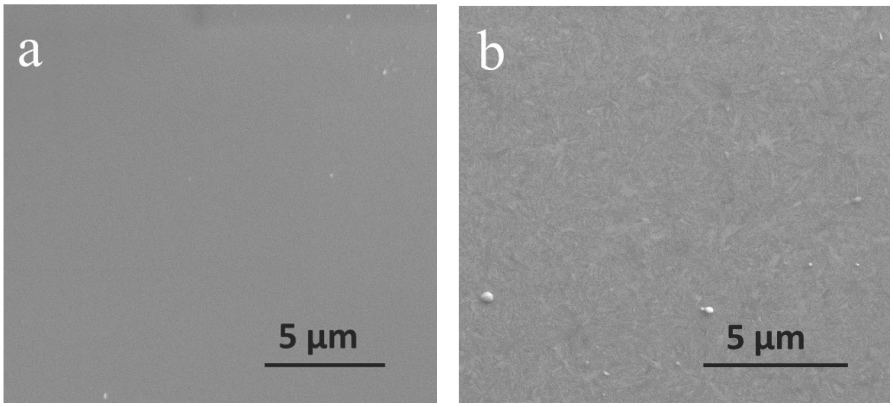

Figure 3.7. SEM images of samples: (a) newly formed film deposited on an ITO glass substrate before heat treatment, (b) WO_3 film deposited on an ITO glass substrate after heat treatment.

3.3.3. Attenuated total reflectance (ATR) Fourier transform infrared (FTIR) spectroscopy

ATR FTIR spectra were recorded on a Nicolet 8700 FTIR spectrometer (Thermo Scientific, USA). A horizontal single-bounce ATR diamond accessory was utilized for FTIR characterization. The spectra were recorded in wavenumbers ranging from 400 cm^{-1} to 4000 cm^{-1} at a spectral resolution of 2 cm^{-1}.

The FTIR spectroscopy results are shown in Figure 3.8. For the FTIR spectrum for ITO glass (curve a in Figure 3.8), all observed absorptions were in good agreement with previous reports [108, 109]. Curve b in Figure 3.8 shows no new absorption peaks compared with the spectrum for the ITO glass. The new formed WO_3 films after heat treatment showed two new absorptions at ca. 980 cm^{-1} and ca. 710 cm^{-1} (curve c in Figure 3.8), which correspond to W = O and O-W-O stretching vibrations of WO_3 [110]. Between 4000 cm^{-1} and 1600 cm^{-1}, the samples' spectra were almost identical. Therefore, the wavenumbers ranging from 4000 cm^{-1} to 1600 cm^{-1} were omitted from the curves in Figure 3.8. The spectra values are shown only from 400 cm^{-1} to 1600 cm^{-1} in Figure 3.8.

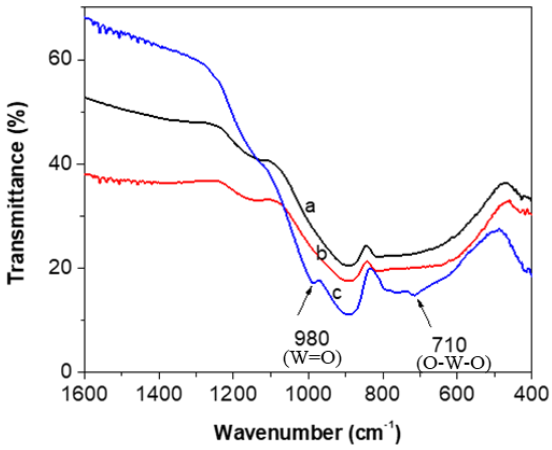

Figure 3.8. FTIR spectra of (a) ITO glass, (b) newly formed film coated on ITO glass before heat treatment, and (c) WO_3 film coated on ITO glass after heat treatment.

3.3.4. AutoLab PGSTAT302N electrochemical workstation

Cyclic voltammetry (CV) measurements were taken by using a potentiostatic procedure at a scan rate of 20 mV/s in the potential range of -0.5 V to 1.0 V (vs. Ag/AgCl, 3 M KCl) on an AutoLab PGSTAT302N electrochemical workstation (Metrohm Autolab B.V., Netherlands). A standard three-electrode electrochemical cell was assembled, with the WO_3 film utilized as working electrode, a Pt film utilized as a counter electrode (CE), and a reference electrode (Ag/AgCl, 3 M KCl) utilized as reference electrode (RE). The electrolyte was 0.5 M H_2SO_4 aqueous solution. The experiments were conducted in the ambient. All the potential values measured in this work are based on the Ag/AgCl reference electrode (3M KCl aqueous solution).

3.3.4.1. Influence of scan rate

The kinetic and thermodynamic behavior of as-prepared WO_3 films after heat treatment was investigated by cyclic voltammetry (CV), which was performed between -0.3 V and 0.3 V (vs. Ag/AgCl, 3 M KCl) at scan rates ranging from 5 mV/s to 100 mV/s. The composition electrochemical system is as follows: WE: WO_3 film; CE: Pt wire; RE: Ag/AgCl (3 M KCl); electrolyte: 0.5 M H_2SO_4. The CV curves are shown in Figure 3.9. A cathodic current peak appeared at around -0.15 V (vs. Ag/AgCl, 3 M KCl) and an anodic current peak appeared at around 0.05 V (vs. Ag/AgCl, 3 M KCl) (vs. Ag/AgCl, 3 M KCl) when the scan rate was 20 mV/s. These two potentials were accompanied by the coloration (from colorless to blue) and bleaching (from blue to colorless) of the WO_3 films, respectively.

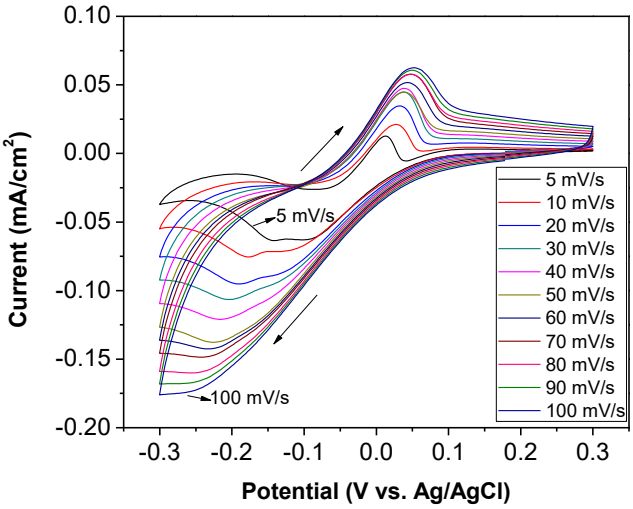

Figure 3.9. CV scans of WO_3 thin films deposited on ITO glass substrates after heat treatment.

With an increasing scan rate, the anodic potential shifted to higher voltages and the cathodic potential shifted to lower voltages, indicating increased polarization at higher sweep rates due to kinetic limitations associated with the H^+ diffusion through the active material. This indication was also supported by the observation that with the relatively high scan rates the WO_3 films were not able to change color completely during each scan. When the scan rate was higher than 60 mV/s, it was difficult to identify the cathodic current peak. At that relatively high scan rate, the WO_3 film was not able to change color completely during each cycle.

3.3.4.2. Durability of as-prepared WO_3 films

The cycling stability of the as-prepared WO_3 films was evaluated. The results were shown in Figure 3.10. No obvious change was observed during the first 200 scans. However, the CV curve changed at ca. 250 scans. This was because the film had started to exfoliate from the substrate, due to the acidic environment with oxygen in the electrolyte. It was found that increasing the cycling voltage to 0.5 V reduced the stability of WO_3 films. The film began to decompose after ca. 120 scans.

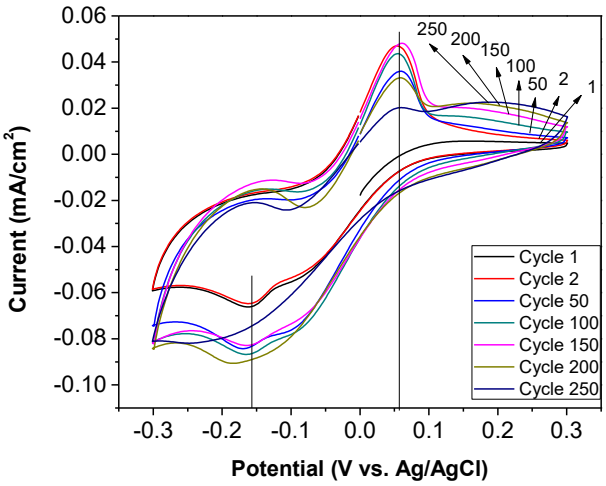

Figure 3.10. CV scans of a WO_3 thin film after heat treatment. Scan rate 20 mV/s.

3.3.5. UV-VIS-NIR spectrophotometer

The samples' transmittance was measured in the wavelength range 280–3300 nm on a UV-VIS-NIR spectrophotometer (PerkinElmer 1050 WB, USA). The samples were measured in situ when they acted as working electrodes in an electrochemical system. The electrolyte of the electrochromic system was sulfuric acid. It was poured into a glass container. The electrolyte absorbed all the radiation from wavelengths above 1350 nm. Thus, the transmittance spectra of most samples were recorded from 280 nm to 1300 nm.

UV-VIS-NIR spectroscopy was utilized to characterize the WO_3 films. The transmittance spectrum in the wavelength range 280–1300 nm of the WO_3 thin film in the colored state was compared with that in the bleached state and the results are shown in Figure 3.11. A potential of -0.3 V (vs. Ag/AgCl, 3 M KCl) was applied to the colored samples for 3600 s. Similarly, a potential of +0.3 V (vs. Ag/AgCl, 3 M KCl) was applied to the bleached samples for 3600 s. Figure 3.11 shows the spectrum of the bleached state (a) and the colored state (b) in the 4^{th} cycle. The largest transmittance difference (ΔT) was 59.1% at wavelength λ = 1300 nm, whereas ΔT was around 20% at λ = 555 nm. The goal was to increase this transmittance difference further both by making the bleached state more transparent and the colored state darker colored.

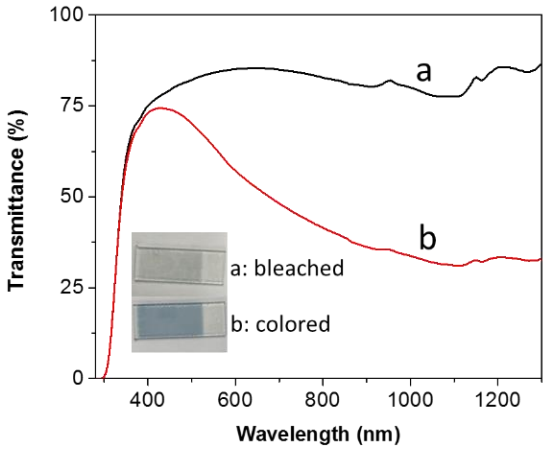

Figure 3.11. Transmittance spectra of a WO_3 thin film electrode in (a) a bleached state at +0.3 V (vs. Ag/AgCl, 3 M KCl), and (b) a colored state at -0.3 V (vs. Ag/AgCl, 3 M KCl) . The inset shows an optical photo of the corresponding sample states.

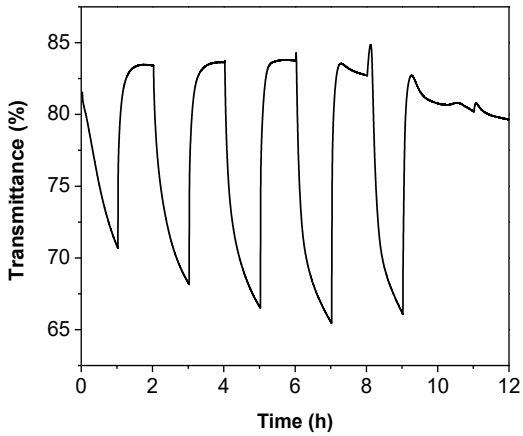

Figure 3.12. Transmittance of 36 nm WO_3 thin film electrode response to the Autolab procedure chronoamperometry: potentials -0.3 V (vs. Ag/AgCl, 3 M KCl) for 1 hour and 0.3 V for 1 hour. Transmittance value was recorded at 555 nm.

Figure 3.12 shows the colored and bleached process, which was recorded at λ = 555 nm from 0 to 12 hours. Firstly, the potential of -0.3 V (vs. Ag/AgCl, 3 M KCl) was applied in the 1st hour. Thereafter, the potential of +0.3 V (vs. Ag/AgCl, 3 M KCl) was applied in the 2nd hour. Subsequently,

the potentials of -0.3 V and +0.3 V (vs. Ag/AgCl, 3 M KCl) were applied from the 3rd hour to the 12th hour. Additionally, in situ coloration and bleaching of the samples were done, and a constant potential of -0.3 V and 0.3 V (vs. Ag/AgCl 3 M KCl) was utilized to color and bleach the samples, respectively. First, the potential of -0.3 V (vs. Ag/AgCl, 3 M KCl) was applied in the 1st hour. Subsequently, the potential of +0.3 V (vs. Ag/AgCl, 3 M KCl) was applied in the 2nd hour. Furthermore, the cycled potentials of -0.3 V and +0.3 V (vs. Ag/AgCl, 3 M KCl) were applied alternately for 1 hour. The coloration and bleaching state processes were recorded at a wavelength of 555 nm.

The color of the WO_3 film was changed from colorless to blue by the negative potential and the WO_3 film was bleached by the positive potential. The bleached transmittance reached a steady value (84%) for each cycle, whereas the colored transmittance value became lower and lower from 1st cycle to the 4th cycle. This means that the colored process had not been completed during the course of 1 hour. The 5th transmittance value was higher than the 4th one due to the influence of some degradation that happened after around 8 hours. The film lost its color changing properties almost completely after 10 hours (i.e. the film had become degraded). It seemed that the system with the 36 nm WO_3 film as a working electrode could not stand the acidic environment with oxygen in the electrolyte for a prolonged time. However, it might be possible to solve this problem by fabricating an oxygen-free solid state electrochromic device.

3.4. Ionic liquid based electrolytes preparation

Due to good physical and chemical properties, ILs were prepared and investigated as ion conductors (electrolyte) for electrochromic devices. ILs of $BmimBF_4$, $BmimPF_6$, BmimCl, OmimCl, $BmimFeCl_4$, and $OmimFeCl_4$ were utilized in this work. ILs of $BmimBF_4$, $BmimPF_6$, BmimCl, and OmimCl were purchased from a chemical company. $BmimFeCl_4$ and $OmimFeCl_4$ were synthesized in our laboratory. The synthesis process of $OmimFeCl_4$ was carried out as follows: OmimCl is added into a three necked flask. Subsequently, the same mole of iron (III) chloride hexa-hydrate ($FeCl_3 \cdot 6H_2O$) is added into the three necked flask. The reaction lasts for 8 hours under stirring at room temperature. Subsequently, the obtained IL was dried in the dry room using the method shown as follows. IL was dried using the vacuum pump in a dry room. Water content in the dry room is < 25 ppm. The IL drying procedure is shown as follows. First of all, IL is dried in the dry room using the membrane pump for at least 2 days. The vacuum pressure of the final dried ILs pressure is ca. 10^{-3} mbar. Subsequently, the pre-dried IL is dried further using an extremely high vacuum (10^{-7}~10^{-8} mbar) pressure pump to dry for at least 3 days at a certain temperature to remove the water and solvent in the IL. Water content of the final obtained $OmimFeCl_4$ is less than 25 ppm. The synthesis process of $BmimFeCl_4$ is similar to that of $OmimFeCl_4$ as shown above.

Thermal properties, including thermal conductivity and thermal diffusivity, are important for utilization of ILs as ion conductors in electrochromic devices. Therefore, thermal conductivity of water and some pure ILs, including $BmimBF_4$, $BmimPF_6$, OmimCl, $BmimFeCl_4$, and $OmimFeCl_4$, was measured. In addition, thermal diffusivity of pure ILs, including $BmimBF_4$, $BmimPF_6$, $BmimFeCl_4$, OmimCl, and $OmimFeCl_4$, was measured. The results showed that ILs resulted in less energy loss than water in energy storage. This also demonstrated that ILs have better performance than water based the ion conductor in electrochromic smart windows due to less energy loss and consumption. Moreover, density, viscosity, heat capacity, decomposition temperature, ionic conductivity, and electrochemical window of IL based electrolytes (ion conductor) were measured. These physical and chemical properties of ILs are also crucial when ILs are utilized as electrolytes (ion conductor) in making electrochromic smart window and electric devices. In the end, $BmimFeCl_4$ was utilized as an example to prove the performance of ILs as ion conductor for reversible redox couple transformation in electrochemical reaction. Chemical structure, physical and thermal stability properties, including density, viscosity, melting point, decomposition temperature, ionic conductivity, electrochemical window of BmimFeC1$_4$ were investigated. Furthermore, $BmimFeCl_4$ is utilized as electrolyte in an electric device, iron-ion battery, to investigate the performance of $BmimFeCl_4$ as ion conductor for reversible redox couple transformation in electrochemical reaction. The results showed that $BmimFeCl_4$ has good electrochemical properties. However, $BmimFeCl_4$ is not a perfect ion conductor for electrochromic devices because of the color of BmimFeC1$_4$. Due to good properties of ILs, other transparent ILs with color will be further utilized to produce electrochromic glass for electrochromic smart windows applications.

Chapter 4. Summary of Papers

This chapter gives an overview of the main research outcomes from seven papers that were included in this thesis. They were published or submitted as journal papers or conference papers.

Paper 1. Synthesis and characterization of tungsten oxide electrochromic thin films

A RF sputtering method was utilized for tungsten oxide film preparation. The thickness of the tungsten oxide film can be controlled at nanometer scale. Tungsten oxide thin films with thickness of ~36 nm were prepared and investigated. The microstructures of the as-prepared tungsten oxide thin films were characterized using X-ray diffraction, scanning electron microscopy, and Fourier transform infrared spectroscopy. The electrochromic properties of as-prepared WO_3 films were investigated using cyclic voltammetry (CV) analysis and UV-VIS-NIR spectroscopy. At a scan rate of 20 mV/s, the color of the WO_3 films changed at around -0.15 V and bleached at around 0.05 V. The WO_3 films could be cycled for 200 times between the potentials -0.3 V and +0.3 V (vs. Ag/AgCl, 3 M KCl).

Paper 2. Electrochromic properties of WO_3 thin films: The role of film thickness

Tungsten oxide (WO_3) thin films with various thicknesses of 36 nm, 72 nm, 108 nm and 180 nm were prepared using RF sputtering method. The morphologies and microstructures of the as-prepared WO_3 thin films were characterized using XRD, SEM, and FTIR. In addition, UV-VIS-NIR spectroscopy was utilized for transmittance investigations of the films.

The transmittance of the films changed during the electrochemical cycles. It was found that WO_3 films with various thicknesses gave various transmittance modulation between colored and bleached states. The bleached films appeared pale gray, pale blue, lemon green, and brown, while the colored films appeared blue with different transmittance levels. Among film samples with thickness of 36 nm, 72 nm, 108 nm and 180 nm, the largest transmittance modulation ΔT_{550nm} was obtained from a sample with thickness of 108 nm, which was 66% when measured in 0.5 M H_2SO_4. The results showed that the transmittance value of the colored samples decreased with increasing thickness, while the transmittance value of the bleached samples was not influenced by their thicknesses.

Paper 3. Influence of O_2 on electrochromic WO_3 thin films preparation using radio frequency sputtering

Tungsten oxide (WO_3) thin films with thickness of 72 nm were prepared using the RF sputtering method. ITO glass was used as a substrate when doing RF sputtering with AJA sputter. Both the influence of present oxygen during the sputtering process, and the influence of heat treatment after sputtering were investigated.

Films prepared under different conditions showed either an amorphous structure or crystal structure. They also showed differences in transmittance modulation and aging ability. Sample A was prepared without oxygen during the RF sputtering process, and the sputtered film underwent heat treatment. The results showed that the coated film on top of Sample A was an amorphous W film, which did not have any electrochromic ability. Sample B was prepared without oxygen during the RF sputtering process, and the sputtered film underwent heat treatment. The results showed that the coated film on top of Sample B was a crystal WO_3 film, which had good transmittance modulation ability. The transmittance modulation value reached 44.8% when measured at wavelength λ = 550 nm using ultraviolet-visible-near infrared (UV-VIS-NIR) spectroscopy, and showed good aging ability. Sample C was prepared with oxygen during the RF sputtering process, and the sputtered film was not heat treated. The results showed that the coated film on top of Sample C was an amorphous WO_3 film, which had transmittance modulation ability, but the transmittance value was only 25.3%. Furthermore, the film had bad aging ability. Sample D was prepared with oxygen during the RF sputtering, and the sputtered film underwent heat treatment. The results showed that the coated film on top of Sample D was a crystal WO_3 film. The film had the best transmittance modulation ability. The transmittance value was 50.9%. In addition, the film had the best aging ability compared with the other films that were prepared.

The results showed that the electrochromic performance of the WO_3 samples was improved by applying O_2 during the RF sputtering process. Furthermore, heat treatment after RF sputtering might have caused a transition of crystalline from amorphous to monoclinic for WO_3 thin films. The aging ability demonstrated large improvement after the crystal transition. In addition, the crystal transition also led to an increased transmittance modulation value.

Paper 4. Electrochromic materials and their characterization by solar radiation glazing factors for smart window applications

Electrochromic materials (ECMs) and electrochromic windows (ECWs) are able to regulate the amount of solar radiation throughput, due to the application of an external electrical voltage. Hence, as smart window applications, ECWs may decrease heating, cooling, and electricity loads in buildings

by admitting the optimum level of solar energy and daylight into the buildings at any given time (e.g., in a cold winter climate versus a warm summer climate. The following solar radiation glazing factors characterize ECWs' dynamic and flexible control over the effects of solar radiation: ultraviolet solar transmittance (T_{uv}), visible solar transmittance (T_{vis}), solar transmittance (T_{sol}), solar material protection factor (SMPF), solar skin protection factor (SSPF), external visible solar reflectance ($R_{vis,ext}$), internal visible solar reflectance ($R_{vis,int}$), solar reflectance (R_{sol}), solar absorbance (A_{sol}), emissivity (e), solar factor (SF), and color rendering factor (CRF). In summary, comparison of these important solar quantities for various ECM and ECW combinations and configurations benefits the selection of the most appropriate ones for specific smart window and building applications.

Paper 5. Measurements of ionic liquids thermal conductivity and thermal diffusivity

Ionic liquids (ILs) are a hot research topic and have been utilized in many scientific research fields. They have also been utilized in devices of energy saving, energy conversion, and energy storage, including electrochromic smart windows, solar cells, batteries, and supercapacitors. Thermal conductivity and thermal diffusivity of ILs are crucial to utilize ILs in electrochromic smart windows. However, the thermal conductivity and thermal diffusivity of most ILs are often unknown.

Accordingly, the thermal conductivity and thermal diffusivity of ILs were investigated in the work reported in Paper 5. A hot disk method for ILs thermal conductivity and thermal diffusivity measurement was developed. Firstly, thermal conductivity of water was measured to check the reliability of the new method developed in this work. Secondly, thermal conductivity of five pure ILs, including $BmimBF_4$, $BmimPF_6$, OmimCl, $BmimFeCl_4$, and $OmimFeCl_4$, was measured. It was found that the thermal conductivity measurement of ILs using the hot disk method had high reliability compared with the thermal conductivity measurement values of water, $BmimBF_4$, and $BmimPF_6$ reported in the literature. In addition, the experimental results showed that all average thermal conductivity values of the five pure ILs were no more than 0.1898 $Wm^{-1}K^{-1}$, which is much lower than the average measured thermal conductivity of water, namely 0.6033 $Wm^{-1}K^{-1}$. Moreover, thermal diffusivity of the five pure ILs was measured. All average thermal diffusivity values of ILs of $BmimBF_4$, $BmimPF_6$, $BmimFeCl_4$, OmimCl and $OmimFeCl_4$ were no more than 0.1185 mm^2s^{-1}. The thermal diffusivity of water is reported as 0.143 mm^2s^{-1} in the literature [111].

The results showed that ILs resulted in less energy loss than water in energy storage. This also demonstrated that ILs has better performance than water based ion conductors for less energy loss and consumption in electrochromic smart windows. It is concluded that the thermal conductivity and

thermal diffusivity measurements of ionic liquids can make ILs beneficial when they are utilized as electrolytes in the preparation of smart glass films.

Paper 6. Ionic liquid based electrolytes preparation and characterization of density, viscosity, crystallization temperature, decomposition temperature, ionic conductivity, and electrochemical window

In this work, density, viscosity, heat capacity, decomposition temperature, ionic conductivity, and electrochemical window of IL based electrolytes (ion conductor) were measured. These physical and chemical properties of ILs are important when ILs are utilized as electrolytes (ion conductor) in the fabrication of electrochromic smart window and electric devices. Initially, density of ILs was measured using a density meter. Thereafter, viscosity of various ILs was investigated using a rheological method. In addition, crystalline temperature of various ILs samples was investigated using DSC. Moreover, decomposition temperature of ILs was investigated using TGA. Furthermore, ionic conductivity and electrochemical window of ILs samples were measured using electrochemical instruments. The measurement results showed that ILs had good physical and chemical properties and can be utilized to produce high performance electrical devices and electrochromic devices (for example, electrochromic smart windows).

Paper 7. Rechargeable iron-ion battery using pure ionic liquid electrolyte

In this work, a pure ionic liquid of 1-butyl-3-methylimidazolium tetrachloroferrate ($BmimFeCl_4$), which was synthesized and utilized as electrolyte (ion conductor) in this work. Chemical structure, physical and thermal stability properties, including density, viscosity, melting point and decomposition temperature, of $BmimFeCl_4$ were investigated. In addition, electrochemical properties of the prepared ionic liquids, including electrochemical window and ionic conductivity, were investigated. Moreover, $BmimFeCl_4$ is utilized as an electrolyte in an electric device, iron-ion battery, for further application of IL based ion conductors in electrochromic smart windows. The experimental results showed that IL $BmimFeCl_4$ has good physical and electrochemical properties as electrolyte. The reason why $BmimFeCl_4$ was utilized in this paper is that: (1) Easy to synthesize; (2) Not water or oxygen sensitive; (3) Low cost; (4) Non-flammable; (5) Good thermal, physical and chemical properties, including low melting point, high decomposition temperature, and low viscosity. Due to good properties of ILs mentioned above, $BmimFeCl_4$ and other transparent ILs will be further utilized to produce electrochromic glass for electrochromic smart windows development.

Chapter 5. Conclusions

Electrochromic WO_3 films were prepared by RF sputtering method. Microstructures of the as-prepared WO_3 thin films were characterized using XRD, SEM, and FTIR. In addition, electrochromic properties of the as-prepared WO_3 films were investigated using CV analysis and UV-VIS-NIR spectroscopy. The results showed that the prepared WO_3 thin films had good electrochromic properties.

WO_3 thin films with various thicknesses were prepared to investigate the effect of film thickness on the performance of prepared WO_3 thin films. WO_3 films with various thicknesses of 36 nm, 72 nm, 108 nm, and 180 nm were prepared. They showed various transmittance values in their colored and bleached states. The results showed that the transmittance values of the colored samples decreased with increasing thickness, whereas the transmittance values of the bleached samples were unrelated to their thicknesses. The films showed different colors in their bleached states. The film with the largest transmittance modulation had a thickness of 108 nm.

In addition, the effect of oxygen presence during the RF sputtering process, and the effect of heat treatment of sputtered films on the electrochromic performance of the WO_3 thin films were investigated. WO_3 thin films with thickness of 72 nm prepared under different conditions showed amorphous or crystalline structure. They showed different transmittance modulation and aging durability. The results also showed that the electrochromic performance of the WO_3 samples was improved by applying O_2 during the RF sputtering process. Furthermore, it was found that the heat treatment might cause a crystalline transition from amorphous to monoclinic structure for the RF sputtered WO_3 thin films. The aging durability demonstrated a large improvement after the crystalline transition. In addition, the crystalline transition led to an increased transmittance modulation value. The results showed that both oxygen and heat treatment could improve the electrochromic properties of the WO_3 films prepared using the RF sputtering method.

The research work on electrochromic windows (ECWs) showed that they can dynamically control daylight and solar radiation energy in buildings. Such control may be readily characterized by the following solar radiation glazing factors: ultraviolet solar transmittance (T_{uv}), visible solar transmittance (T_{vis}), solar transmittance (T_{sol}), solar material protection factor (SMPF), solar skin protection factor (SSPF), external visible solar reflectance ($R_{vis,ext}$), internal visible solar reflectance ($R_{vis,int}$), solar reflectance (R_{sol}), solar absorbance (A_{sol}), emissivity (ε), solar factor (SF), and color rendering factor (CRF). In this thesis, three different ECWs were investigated, all of them

demonstrating a large solar radiation modulation. The solar radiation glazing and modulation factors were calculated for selected two-layer and three-layer ECW windowpane configurations.

Moreover, the thermal conductivity and thermal diffusivity of ionic liquids (ILs) were investigated. A hot disk method for measuring ILs' thermal conductivity and thermal diffusivity was utilized. The thermal conductivity of pure ILs, including $BmimBF_4$, $BmimPF_6$, OmimCl, $BmimFeCl_4$, and $OmimFeCl_4$, was measured. It was found that thermal conductivity measurement values of water, $BmimBF_4$, and $BmimPF_6$ using the hot disk method had high reliability when compared with literature values. The results showed that ILs resulted in less energy loss than water in energy storage. This also demonstrated that ILs have better performance than water based ion conductors for less energy loss and consumption in electrochromic smart windows. Thermal conductivity and thermal diffusivity measurements of ILs may benefit the utilization of ILs as electrolytes in electrochromic devices.

Furthermore, density, viscosity, crystallization temperature, thermal stability, and ionic conductivity of IL-based electrolytes were investigated. The measurement results showed that ILs had good physical and chemical properties and can be utilized to produce high performance electrical devices and electrochromic devices (for example, electrochromic smart windows).

In the end, a pure ionic liquid of 1-butyl-3-methylimidazolium tetrachloroferrate ($BmimFeCl_4$), which was synthesized and utilized as electrolyte (ion conductor) in this work. Chemical structure, physical and thermal stability properties, including density, viscosity, melting point and decomposition temperature, of $BmimFeC1_4$ were investigated. In addition, electrochemical properties of the prepared ionic liquids, including electrochemical window and ionic conductivity, were investigated. Moreover, $BmimFeCl_4$ is utilized as an electrolyte in an electric device, iron-ion battery, for further application of IL based ion conductors in electrochromic smart windows. The experimental results showed that IL $BmimFeCl_4$ has good physical and electrochemical properties as electrolyte. Due to good physical and chemical properties, $BmimFeCl_4$ and other transparent ILs will be further utilized to produce electrochromic glass for electrochromic smart windows development.

Chapter 6. Suggestions for Further Work

Current smart window technologies have a large potential to reduce the energy consumption in buildings. However, the efficiency of the smart windows available today is still relatively low in this respect. Therefore, it is crucial and important to further improve the smart window technologies. More research work should be carried out to improve properties of the electrochromic thin films and devices. Color change response time should be decreased, value of modulation of transmittance should be larger, cyclic stability should be improved for both electrochromic films and devices.

In this thesis, WO_3 thin film was prepared by RF sputtering technology with an AJA E-Beam evaporator & Sputter. The target utilized was a WO_3 target. Research work about utilizing oxygen during the sputtering process was done. In the future, the W target should be utilized instead of WO_3 target. Oxygen influence during sputteration should be researched. The WO_3 film can be prepared by RF sputter，with W target and has oxygen during sputteration. And WO_3 film can also be prepared by RF sputter, with W target and without Oxygen during sputteration, but carried heat treatment to sputtered films.

The research within this thesis demonstrated that the WO_3 thin film with a thickness of 108 nm had the best electrochromic properties compared with other WO_3 thin films with other thicknesses. Therefore, it is recommended that in further work WO_3 films are prepared with a thickness close to 108 nm.

Electrochromic properties of newly prepared WO_3 films will be compared to find the one which has the largest value of modulation of transmittance.

To increase the color changing speed of the WO_3 thin film, it should be tried to add some transparent conductive agent when preparing the electrochromic film.

Furthermore, research work on electrochromic devices using ionic liquid based electrolytes may also be carried out with models of electrochromic devices in the future. This future research can focus on how to replace the utilization of aqueous electrolytes in WO_3 electrochromic devices with ionic liquid based electrolytes in order to decrease response time, increase the cyclic stability and improve the thermal stability of the devices.

Further research should be carried out on complete electrochromic devices based on new prepared WO_3 films which have the best electrochromic properties. The electrolyte layer will be prepared by selected ionic liquids in above future work.

References

1. Dounis, A. I.; Caraiscos, C., Advanced control systems engineering for energy and comfort management in a building environment-A review. *Renewable and Sustainable Energy Reviews* **2009,** *13* (6), 1246-1261.
2. Li, B.; Yao, R., Urbanisation and its impact on building energy consumption and efficiency in China. *Renewable Energy* **2009,** *34* (9), 1994-1998.
3. Pérez-Lombard, L.; Ortiz, J.; Pout, C., A review on buildings energy consumption information. *Energy and Buildings* **2008,** *40* (3), 394-398.
4. Zhao, D.; McCoy, A. P.; Du, J.; Agee, P.; Lu, Y., Interaction effects of building technology and resident behavior on energy consumption in residential buildings. *Energy and Buildings* **2017,** *134*, 223-233.
5. Phase Change Composite Materials for Energy Efficient Building Envelopes. https://www.seas.ucla.edu/~pilon/PCMIntro.html (accessed 20 October).
6. Granqvist, C. G., Electrochromics for smart windows: Oxide-based thin films and devices. *Thin Solid Films* **2014,** *564*, 1-38.
7. Jelle, B. P.; Hynd, A.; Gustavsen, A.; Arasteh, D.; Goudey, H.; Hart, R., Fenestration of today and tomorrow: A state-of-the-art review and future research opportunities. *Solar Energy Materials and Solar Cells* **2012,** *96*, 1-28.
8. Warren L. MaCabe, J. C. S., Peter Harriott, *Unit Operations of Chemical Engineering*. McGRAW+Hill Interational Edition: 2005.
9. Wikipedia https://en.wikipedia.org/wiki/Thermal_conduction (accessed 12 April, **2021**).
10. Heat transfer. https://en.wikipedia.org/wiki/Heat_transfer (accessed 12 April, **2021**).
11. Thermal radiation. https://en.wikipedia.org/wiki/Thermal_radiation (accessed 15 April, **2021**).
12. Trermal transmittance. https://en.wikipedia.org/wiki/Thermal_transmittance (accessed 01 August, 2022).
13. Doctor, G. What Are Double-Pane Windows. https://glassdoctor.com/expert-tips/all-about-window-glass/double-pane-windows (accessed 27 July, 2022).
14. Jensen, K. I.; Schultz, J. M.; Kristiansen, F. H., Development of windows based on highly insulating aerogel glazings. *Journal of Non-Crystalline Solids* **2004,** *350*, 351-357.
15. Marchese, K. Aerogel is only twice as dense as air and the lightest solid in the world. https://www.designboom.com/design/aerogel-twice-as-dense-as-air-and-the-lightest-material-in-the-world-06-04-2019/ (accessed 31 July, **2022**).
16. Kalnæs, S. E.; Jelle, B. P., Vacuum insulation panel products: A state-of-the-art review and future research pathways. *Applied Energy* **2014,** *116*, 355-375.
17. Thermal conductivity. http://hyperphysics.phy-astr.gsu.edu/hbase/Tables/thrcn.html (accessed 04 May, **2021**).
18. Thermal Conductivity of Glass. https://www.nuclear-power.com/nuclear-engineering/heat-transfer/thermal-conduction/thermal-conductivity/thermal-conductivity-of-glass/ (accessed 26 August, **2021**).
19. Hung Anh, L. D.; Pásztory, Z., An overview of factors influencing thermal conductivity of building insulation materials. *Journal of Building Engineering* **2021,** *44*, 102604.

20. Huber, M. L.; Harvey, A. H., Thermal conductivity of gases. *CRC Handbook of Chemistry and Physics* **2011,** *92*, 240-241.
21. Midtdal, K.; Jelle, B. P., Self-cleaning glazing products: A state-of-the-art review and future research pathways. *Solar Energy Materials and Solar Cells* **2013,** *109*, 126-141.
22. Hammarberg, E.; Roos, A., Antireflection treatment of low-emitting glazings for energy efficient windows with high visible transmittance. *Thin Solid Films* **2003,** *442* (1), 222-226.
23. Jelle, B. P.; Kalnæs, S. E.; Gao, T., Low-emissivity materials for building applications: A state-of-the-art review and future research perspectives. *Energy and Buildings* **2015,** *96*, 329-356.
24. Jeffrey Rissman, H. K. *Low-emissivity windows*; American Energy innovation council: Case studies on the goverment's role in energy technology innovation, **2012**.
25. Low-e Coatings. https://www.valley-siding.com/low-e-coatings.html (accessed 05 May, **2021**).
26. Wu, L. Y. L.; Zhao, Q.; Huang, H.; Lim, R. J., Sol-gel based photochromic coating for solar responsive smart window. *Surface and Coatings Technology* **2017,** *320*, 601-607.
27. Kamalisarvestani, M.; Saidur, R.; Mekhilef, S.; Javadi, F. S., Performance, materials and coating technologies of thermochromic thin films on smart windows. *Renewable and Sustainable Energy Reviews* **2013,** *26*, 353-364.
28. Aburas, M.; Soebarto, V.; Williamson, T.; Liang, R.; Ebendorff-Heidepriem, H.; Wu, Y., Thermochromic smart window technologies for building application: A review. *Applied Energy* **2019,** *255*, 113522.
29. Xie, Z.; Jin, X.; Chen, G.; Xu, J.; Chen, D.; Shen, G., Integrated smart electrochromic windows for energy saving and storage applications. *Chemical Communications* **2014,** *50* (5), 608-610.
30. Rauh, R. D., Electrochromic windows: an overview. *Electrochimica Acta* **1999,** *44* (18), 3165-3176.
31. Feng, W.; Zou, L.; Gao, G.; Wu, G.; Shen, J.; Li, W., Gasochromic smart window: optical and thermal properties, energy simulation and feasibility analysis. *Solar Energy Materials and Solar Cells* **2016,** *144*, 316-323.
32. Vergaz, R.; Sánchez-Pena, J.-M.; Barrios, D.; Vázquez, C.; Contreras-Lallana, P., Modelling and electro-optical testing of suspended particle devices. *Solar Energy Materials and Solar Cells* **2008,** *92* (11), 1483-1487.
33. Hernandez, T. S.; Alshurafa, M.; Strand, M. T.; Yeang, A. L.; Danner, M. G.; Barile, C. J.; McGehee, M. D., Electrolyte for Improved Durability of Dynamic Windows Based on Reversible Metal Electrodeposition. *Joule* **2020,** *4* (7), 1501-1513.
34. Baetens, R.; Jelle, B. P.; Gustavsen, A., Properties, requirements and possibilities of smart windows for dynamic daylight and solar energy control in buildings: A state-of-the-art review. *Solar Energy Materials and Solar Cells* **2010,** *94* (2), 87-105.
35. Cheng, Y.; Zhang, X.; Fang, C.; Chen, J.; Wang, Z., Discoloration mechanism, structures and recent applications of thermochromic materials via different methods: A review. *Journal of Materials Science & Technology* **2018,** *34* (12), 2225-2234.
36. Gao, Y.; Luo, H.; Zhang, Z.; Kang, L.; Chen, Z.; Du, J.; Kanehira, M.; Cao, C., Nanoceramic VO2 thermochromic smart glass: A review on progress in solution processing. *Nano Energy* **2012,** *1* (2), 221-246.

37. Granqvist, C. G.; Lansåker, P. C.; Mlyuka, N. R.; Niklasson, G. A.; Avendaño, E., Progress in chromogenics: New results for electrochromic and thermochromic materials and devices. *Solar Energy Materials and Solar Cells* **2009,** *93* (12), 2032-2039.
38. Warwick, M. E. A.; Binions, R., Advances in thermochromic vanadium dioxide films. *Journal of Materials Chemistry A* **2014,** *2* (10), 3275-3292.
39. Tällberg, R.; Jelle, B. P.; Loonen, R.; Gao, T.; Hamdy, M., Comparison of the energy saving potential of adaptive and controllable smart windows: A state-of-the-art review and simulation studies of thermochromic, photochromic and electrochromic technologies. *Solar Energy Materials and Solar Cells* **2019,** *200*, 109828.
40. Kim, J.-H.; Han, S.-H., Indoor daylight performances of optimized transmittances with electrochromic-applied kinetic louvers. *Buildings* **2022,** *12* (3), 263.
41. Sageglass. https://www.sageglass.com/en/products/sageglass (accessed 05 May, **2021**).
42. Wittwer, V.; Datz, M.; Ell, J.; Georg, A.; Graf, W.; Walze, G., Gasochromic windows. *Solar Energy Materials and Solar Cells* **2004,** *84* (1), 305-314.
43. Bonsor, K. How smart windows work. https://chem.beloit.edu/classes/nanotech/smart/smart_windows.pdf (accessed 02 October, **2021**).
44. Yoshimura, K.; Yamada, Y.; Bao, S.; Tajima, K.; Okada, M., Preparation and characterization of gasochromic switchable-mirror window with practical size. *Solar Energy Materials and Solar Cells* **2009,** *93* (12), 2138-2142.
45. How smart windows work. https://home.howstuffworks.com/home-improvement/construction/green/smart-window.htm/printable (accessed 31 July, **2022**).
46. Ghosh, A.; Norton, B.; Duffy, A., Measured overall heat transfer coefficient of a suspended particle device switchable glazing. *Applied Energy* **2015,** *159*, 362-369.
47. Strand, M. T.; Barile, C. J.; Hernandez, T. S.; Dayrit, T. E.; Bertoluzzi, L.; Slotcavage, D. J.; McGehee, M. D., Factors that determine the length scale for uniform tinting in dynamic windows based on reversible metal electrodeposition. *ACS Energy Letters* **2018,** *3* (11), 2823-2828.
48. Zhao, Y. Shut in and restart of waxy crude oil pipelines: gelation, rheology, model development, and application of polymer/ionic liqudi based additive. PhD thesis, NTNU, Trondheim, **2013**.
49. Branco, A.; Branco, L. C.; Pina, F., Electrochromic and magnetic ionic liquids. *Chemical Communications* **2011,** *47* (8), 2300-2302.
50. Hassab, S.; Padilla, J., Chapter 10 - Use of ionic liquids in electrochromic devices. In *Ionic Liquids in Separation Technology*, Pérez De Los Ríos, A.; Hernández Fernández, F. J., Eds. Elsevier: Amsterdam, 2014; pp 301-333.
51. Platt, J. R., Electrochromism, a possible change of color producible in dyes by an electric field. *The Journal of Chemical Physics* **1961,** *34* (3), 862-863.
52. Kobosew, N.; Nekrassow, N. I., Bildung freier Wasserstoffatome bei Kathodenpolarisation der Metalle. *Zeitschrift für Elektrochemie und angewandte physikalische Chemie* **1930,** *36* (8), 529-544.
53. Brimm, E.; Brantley, J.; Lorenz, J.; Jellinek, M., Sodium and potassium tungsten bronzes1, 1a. *Journal of the American Chemical Society* **1951,** *73* (11), 5427-5432.
54. Hjelm, A.; Granqvist, C. G.; Wills, J. M., Electronic structure and optical properties of WO_3, $LiWO_3$, $NaWO_3$, and HWO_3. *Physical Review B* **1996,** *54* (4), 2436-2445.
55. Granqvist, C. G., In *Handbook of inorganic electrochromic materials*, Granqvist, C. G., Ed. Elsevier Science B.V.: Amsterdam, **1995**.

56. Deb, S. K., A novel electrophotographic system. *Applied Optics* **1969,** *8* (S1), 192-195.
57. Deb, S. K., Optical and photoelectric properties and colour centres in thin films of tungsten oxide. *Philosophical Magazine* **1973,** *27* (4), 801-822.
58. Zhang, J. Research on WO_3 electrochromic film and device. Zhejiang University, **2012**.
59. Mehmood, A.; Long, X.; Haidry, A. A.; Zhang, X., Trends in sputter deposited tungsten oxide structures for electrochromic applications: A review. *Ceramics International* **2020,** *46* (15), 23295-23313.
60. Granqvist, C. G.; Avendaño, E.; Azens, A., Electrochromic coatings and devices: survey of some recent advances. *Thin Solid Films* **2003,** *442* (1), 201-211.
61. Electrochromic device. https://en.wikipedia.org/wiki/Electrochromic_device (accessed 12 May, **2021**).
62. Granqvist, C. G., Electrochromic devices. *Journal of the European Ceramic Society* **2005,** *25* (12), 2907-2912.
63. Haacke, G., Transparent conducting coatings. *Material Science* **1977,** *7* (Annual Review).
64. Afre, R. A.; Sharma, N.; Sharon, M.; Sharon, M., Transparent conducting oxide films for various applications: a review. *Reviews on Advanced Materials Science* **2018,** *53* (1), 79-89.
65. Xia, Y.; Sun, K.; Ouyang, J., Solution-processed metallic conducting polymer films as transparent electrode of optoelectronic devices. *Advanced Materials* **2012,** *24* (18), 2436-2440.
66. Buch, V. R.; Chawla, A. K.; Rawal, S. K., Review on electrochromic property for WO_3 thin films using different deposition techniques. *Materials Today: Proceedings* **2016,** *3* (6), 1429-1437.
67. Granqvist, C. G., Electrochromic tungsten oxide films: Review of progress 1993–1998. *Solar Energy Materials and Solar Cells* **2000,** *60* (3), 201-262.
68. Thakur, V. K.; Ding, G.; Ma, J.; Lee, P. S.; Lu, X., Hybrid materials and polymer electrolytes for electrochromic device applications. *Advanced Materials* **2012,** *24* (30), 4071-4096.
69. Abe, Y.; Lee, S.-H.; Zayim, E. O.; Tracy, C. E.; Pitts, J. R.; Deb, S. K., Electrochromic properties of sputtered Ni oxide thin films in neutral KCl electrolytes. *Electrochemical and Solid-State Letters* **2006,** *9* (1), G17.
70. Abe, Y.; Lee, S.-H.; Zayim, E. O.; Tracy, C. E.; Pitts, J. R.; Deb, S. K., Effect of O_2 flow concentration during reactive sputtering of Ni oxide thin films on their electrochemical and electrochromic properties in aqueous acidic and basic electrolyte solutions. *Japanese Journal of Applied Physics* **2006,** *45* (10A), 7780-7783.
71. Abe, Y.; Lee, S.-H.; Tracy, C. E.; Pitts, J. R.; Deb, S. K., Electrochromic Properties of Sputtered Ni Oxide Thin Films in Acidic KCl+H_2SO_4 Aqueous Solutions. *Electrochemical and Solid-State Letters* **2006,** *9* (8), J31.
72. Brazier, A.; Appetecchi, G. B.; Passerini, S.; Surca Vuk, A.; Orel, B.; Donsanti, F.; Decker, F., Ionic liquids in electrochromic devices. *Electrochimica Acta* **2007,** *52* (14), 4792-4797.
73. De Ribamar Martins Neto, J.; Torresi, R. M.; Cordoba de Torresi, S. I., Electrochromic behavior of WO_3 nanoplate thin films in acid aqueous solution and a protic ionic liquid. *Journal of Electroanalytical Chemistry* **2016,** *765*, 111-117.
74. Kraft, A., Electrochromism: a fascinating branch of electrochemistry. *ChemTexts* **2018,** *5* (1), 1.
75. Assis, L. M. N.; Leones, R.; Kanicki, J.; Pawlicka, A.; Silva, M. M., Prussian blue for electrochromic devices. *Journal of Electroanalytical Chemistry* **2016,** *777*, 33-39.
76. Marcel, C.; Tarascon, J. M., An all-plastic $WO_3 \cdot H_2O$/polyaniline electrochromic device. *Solid State Ionics* **2001,** *143* (1), 89-101.

77. Camurlu, P., Polypyrrole derivatives for electrochromic applications. *RSC Advances* **2014,** *4* (99), 55832-55845.
78. Nicho, M. E.; Hu, H.; López-Mata, C.; Escalante, J., Synthesis of derivatives of polythiophene and their application in an electrochromic device. *Solar Energy Materials and Solar Cells* **2004,** *82* (1), 105-118.
79. Gadgil, B.; Damlin, P.; Ääritalo, T.; Kvarnström, C., Electrosynthesis of viologen cross-linked polythiophene in ionic liquid and its electrochromic properties. *Electrochimica Acta* **2014,** *133*, 268-274.
80. Mortimer, R. J., Organic electrochromic materials. *Electrochimica Acta* **1999,** *44* (18), 2971-2981.
81. Sharmoukh, W.; Ko, K. C.; Ko, J. H.; Nam, H. J.; Jung, D.-Y.; Noh, C.; Lee, J. Y.; Son, S. U., 5-Substituted isophthalate-based organic electrochromic materials. *Journal of Materials Chemistry* **2008,** *18* (37), 4408-4413.
82. 3,4-Ethylenedioxythiophene. https://en.wikipedia.org/wiki/3,4-Ethylenedioxythiophene (accessed 16 August, **2022**).
83. Lock, J. P.; Lutkenhaus, J. L.; Zacharia, N. S.; Im, S. G.; Hammond, P. T.; Gleason, K. K., Electrochemical investigation of PEDOT films deposited via CVD for electrochromic applications. *Synthetic Metals* **2007,** *157* (22), 894-898.
84. Zhang, J.; Tu, J.-p.; Xia, X.-h.; Wang, X.-l.; Gu, C.-d., Hydrothermally synthesized WO3 nanowire arrays with highly improved electrochromic performance. *Journal of Materials Chemistry* **2011,** *21* (14), 5492-5498.
85. More, A. J.; Patil, R. S.; Dalavi, D. S.; Suryawanshi, M. P.; Burungale, V. V.; Kim, J. H.; Patil, P. S., Synthesis and characterization of potentiostatically electrodeposited tungsten oxide thin films for smart window application. *Journal of Electronic Materials* **2017,** *46* (2), 974-981.
86. Evecan, D.; Zayim, E., Highly uniform electrochromic tungsten oxide thin films deposited by e-beam evaporation for energy saving systems. *Current Applied Physics* **2019,** *19* (2), 198-203.
87. El-Nahass, M. M.; Saadeldin, M. M.; Ali, H. A. M.; Zaghllol, M., Electrochromic properties of amorphous and crystalline WO3 thin films prepared by thermal evaporation technique. *Materials Science in Semiconductor Processing* **2015,** *29*, 201-205.
88. Badilescu, S.; Ashrit, P. V., Study of sol–gel prepared nanostructured WO_3 thin films and composites for electrochromic applications. *Solid State Ionics* **2003,** *158* (1), 187-197.
89. Kalagi, S. S.; Mali, S. S.; Dalavi, D. S.; Inamdar, A. I.; Im, H.; Patil, P. S., Transmission attenuation and chromic contrast characterization of R.F. sputtered WO_3 thin films for electrochromic device applications. *Electrochimica Acta* **2012,** *85*, 501-508.
90. Karuppasamy, A., Electrochromism in surface modified crystalline WO_3 thin films grown by reactive DC magnetron sputtering. *Applied Surface Science* **2013,** *282*, 77-83.
91. Quero, J. M.; Perdigones, F.; Aracil, C., Microfabrication technologies used for creating smart devices for industrial applications. In *Smart Sensors and Mems*, Elsevier: 2018; pp 291-311.
92. Li, W.; Zhang, X.; Chen, X.; Zhao, Y.; Wang, L.; Chen, M.; Li, Z.; Zhao, J.; Li, Y., Lithiation of WO_3 films by evaporation method for all-solid-state electrochromic devices. *Electrochimica Acta* **2020,** *355*, 136817.
93. Rao, M.; Hussain, O., Optical properties of vacuum evaporated WO_3 thin films. *Res. J. Chem. Sci.* **2011,** *2231*, 606X.
94. Joraid, A. A.; Alamri, S. N., Effect of annealing on structural and optical properties of WO3 thin films prepared by electron-beam coating. *Physica B: Condensed Matter* **2007,** *391* (2), 199-205.

95. Agrawal, A.; Habibi, H., Effect of heat treatment on the structure, composition and electrochromic properties of evaporated tungsten oxide films: I. *Thin Solid Films* **1989,** *169* (2), 257-270.
96. Beydaghyan, G.; Renaud, J.-L. M.; Bader, G.; Ashrit, P. V., Enhanced electrochromic properties of heat treated nanostructured tungsten trioxide thin films. *Journal of Materials Research* **2008,** *23* (1), 274-280.
97. Marszalek, K., Magnetron-sputtered WO_3 films for electrochromic devices. *Thin Solid Films* **1989,** *175*, 227-233.
98. Rydosz, A.; Dyndał, K.; Kollbek, K.; Andrysiewicz, W.; Sitarz, M.; Marszałek, K., Structure and optical properties of the WO_3 thin films deposited by the GLAD magnetron sputtering technique. *Vacuum* **2020,** *177*, 109378.
99. Chananonnawathorn, C.; Pudwat, S.; Horprathum, M.; Eiamchai, P.; Limnontakul, P.; Salawan, C.; Aiempanakit, K., Electrochromic property dependent on oxygen gas flow rate and films thickness of sputtered WO_3 films. *Procedia Engineering* **2012,** *32*, 752-758.
100. DC sputtering vs RF sputtering. https://www.aemdeposition.com/sputtering-targets-news/dc-sputtering-vs-rf-sputtering.html (accessed 10 August, **2022**).
101. Meenakshi, M.; Sivakumar, R.; Perumal, P.; Sanjeeviraja, C., Studies on electrochromic properties of RF sputtered vanadium oxide: Tungsten oxide thin films. *Materials Today: Proceedings* **2016,** *3*, S30-S39.
102. Habib, M. A.; Glueck, D., The electrochromic properties of chemically deposited tungsten oxide films. *Solar Energy Materials* **1989,** *18* (3), 127-141.
103. Deepa, M.; Srivastava, A. K.; Sharma, S. N.; Govind; Shivaprasad, S. M., Microstructural and electrochromic properties of tungsten oxide thin films produced by surfactant mediated electrodeposition. *Applied Surface Science* **2008,** *254* (8), 2342-2352.
104. Alberti, S.; Jágerská, J., Sol-gel thin film processing for integrated waveguide sensors. *Frontiers in Materials* **2021,** *8*.
105. Vankova, S.; Zanarini, S.; Amici, J.; Cámara, F.; Arletti, R.; Bodoardo, S.; Penazzi, N., WO3 nanorolls self-assembled as thin films by hydrothermal synthesis. *Nanoscale* **2015,** *7* (16), 7174-7177.
106. Piccolo, A.; Simone, F., Performance requirements for electrochromic smart window. *Journal of Building Engineering* **2015,** *3*, 94-103.
107. He, T.; Ma, Y.; Cao, Y.; Yang, W.; Yao, J., Enhanced electrochromism of WO3 thin film by gold nanoparticles. *Journal of Electroanalytical Chemistry* **2001,** *514* (1-2), 129-132.
108. Meng, L.-j.; dos Santos, M. P., Properties of indium tin oxide (ITO) films prepared by r.f. reactive magnetron sputtering at different pressures. *Thin Solid Films* **1997,** *303* (1), 151-155.
109. Meng, L.-j.; dos Santos, M. P., Properties of indium tin oxide films prepared by rf reactive magnetron sputtering at different substrate temperature. *Thin Solid Films* **1998,** *322* (1), 56-62.
110. Hu, P.; Ma, J.; Wang, T.; Qin, B.; Zhang, C.; Shang, C.; Zhao, J.; Cui, G., NASICON-Structured $NaSn_2(PO_4)_3$ with excellent high-rate properties as anode material for lithium ion batteries. *Chemistry of Materials* **2015,** *27* (19), 6668-6674.
111. Balderas-López, J. A.; Mandelis, A.; Garcia, J. A., Thermal-wave resonator cavity design and measurements of the thermal diffusivity of liquids. *Review of Scientific Instruments* **2000,** *71* (7), 2933-2937.

Collection of Scientific Papers

Paper 1

Synthesis and Characterization of Tungsten Oxide Electrochromic Thin Films

IEEE-NANO, 2018, DOI: 10.1109/NANO.2018.8626293. (Accepted and published on line)

Synthesis and Characterization of Tungsten oxide Electrochromic Thin Films

Yingpeng Zhen[1]*, Tao Gao[1], and Bjørn Petter Jelle[1,2]
[1]Department of Civil and Environmental Engineering, Norwegian University of Science and Technology (NTNU), NO-7491 Trondheim, Norway.
[2]Department of Materials and Structures, SINTEF Building and Infrastructure, NO-7465 Trondheim, Norway.
*Corresponding author: yingpeng.zhen@ntnu.no

***Abstract*—**A radio frequency sputtering method was utilized and developed for tungsten oxide film preparation. The thickness of tungsten oxide film can be controlled at nano scale. Tungsten oxide thin films with thickness of ~36 nm was prepared and investigated. The morphologies and microstructures of the as-prepared tungsten oxide thin films were characterized using X-ray diffraction, scanning electron microscopy, and Flourier transform infrared spectroscopy. Tungsten oxide films utilized in the laboratory changed color from colorless to blue during electrochemical cycles, showing a potential for assembling electrochromic smart windows to modulate the transmitted solar radiations.

I. Introduction

Electrochromic (EC) smart windows are windows whose optical properties can be adjusted with the change of an external electrical field strength. In the presence of an external voltage, the EC materials can change from a dark colored state (e.g., dark blue) to a transparent state with no color tints. EC smart windows have been developed and utilized in energy-efficient buildings. Using EC smart windows, the amount of solar radiation transmitted through windows can be controlled. Consequently, the energy usage by heating and cooling in buildings can be reduced.

Typically, an EC device (e.g., EC smart windows) consists of five functional layers: two transparent electrical conductor layers to inject and extract charge, an active EC layer, an electrolyte, and an ion storage layer, which may in some cases be another complementary EC layer. This sandwich configuration allows a reversible electrochemical reaction to cycle between the EC layer and the ion storage media, with simultaneous injection of electrons/holes and cations/anions. The overall transparency of the EC layer is changed due to the formation of color centers (or defect complexes) or due to an electrochemical reaction that produces a colored compound; a voltage pulse with opposite polarity makes the device regain its original properties [1].

Tungsten oxide (WO_3) is probably the most studied EC material for smart window applications. We have been working on EC smart windows by using WO_3 [2-5] among others. In this work, we developed a radio frequency sputtering method for WO_3 film preparation. This method can accurately control the thickness of WO_3 films at nano scale. WO_3 thin films with a thickness of about 36 nm were prepared by using radio frequency sputtering. Subsequently, WO_3 films were utilized to form a working electrode in our laboratory. We found that the WO_3 films exhibit good electrochemical performance.

II. Sample Preparation

2.1 Materials

WO_3 sputtering target (diameter 5.08 cm, thickness 0.32 cm) was purchased from AJA International Inc., USA. Substrates for the growth of WO_3 thin films were ITO (tin doped indium oxide, In_2O_3(Sn)) glass slides purchased from Sigma-Aldrich. ITO glass slides have a typical transmittance of about 86% at 550 nm and a surface resistivity of about 70-100 Ω/square. The ITO glass slides were cut to small pieces with typical sizes of about 9.2 mm × 25 mm × 1.1 mm in the laboratory for this work. Reagent grade sulfuric acid (H_2SO_4, 96 wt%) and potassium chloride (KCl, 99%) were also purchased from Sigma-Aldrich. Distilled water was utilized throughout the experiments.

2.2 Sputter Process

WO_3 films with thickness of 36 nm were prepared by radio frequency (RF) magnetron sputtering technique using an AJA sputter and evaporator (model: Custom ATC-2200V, AJA International Inc. USA). Argon (Ar) flow was set as 67 sccm (standard cubic centimeter per minute). Plasma strike pressure was 30 mTorr (≈ 4.0 Pa), and strike power was 50 W. After the plasma was strike on, the pressure was changed and maintained at 3 mTorr (≈ 0.4 Pa) during the deposition process. The sputter rate was about 0.05 nm/s.

2.3 Heat Treatment

Heat treatment is necessary for the WO_3 films. Heat treatment was performed and the as-deposited WO_3 film samples were annealed in air at 400 °C for 5 h in an oven.

III. Characterization

3.1 XRD

X-ray diffraction (XRD) analysis was performed using a Bruker D8 A25 Davinci X-ray Diffractometer (Bruker, Germany) with Cu–Kα radiation and LynxEye™ SuperSpeed Detector for 30 minute. XRD data were collected in the range of 15° - 75° with a step size of 0.013°. The structures of the samples were analyzed using the DIFFRAC.EVA V4.2 software (Bruker AXS, Germany).

978-1-5386-5336-4/18/$31.00 ©2018 IEEE

3.2 SEM

A scanning electron microscope (SEM) was utilized to check the surface topography of the samples. The SEM Apreo purchased from Thermo Fisher Scientific (FEI), USA, was utilized in this work.

3.3 FTIR

Attenuated total reflectance (ATR) Fourier transform infrared (FTIR) spectra were recorded on a Nicolet 8700 FTIR Spectrometer (Thermo Scientific, USA). The transmittance of the samples were recorded in the wavenumber range 4000 cm^{-1} to 400 cm^{-1}.

3.4. Cyclic Voltammetry Test

The electrochemical properties of the WO_3 films were characterized by cyclic voltammetry (CV) on an AutoLab electrochemical workstation PGSTAT302N (Metrohm Autolab B.V., Netherlands). The WO_3 films were applied as working electrodes (WE). The counter electrode (CE) was a Pt wire. The reference electrode (RE) was Ag/AgCl (3 M KCl). The electrolyte was 0.5 M H_2SO_4.

3.5. UV-VIS-NIR Spectroscopy

Transmittance of samples was measured in the ultraviolet (UV), visible (VIS) and near infrared (NIR) solar radiation wavelength range (280 -1300 nm) on a UV-VIS-NIR spectrophotometer (PerkinElmer 1050 WB, USA).

In situ coloration and bleaching of the samples were also performed, and a constant potential of -0.3 V and 0.3 V (vs. Ag/AgCl (3 M KCl)) was used to color and bleach the samples, respectively. Firstly, the potential of -0.3V was applied in the 1st hour. Subsequently, the potential of +0.3 V was applied in the 2nd hour. Furthermore, the recycled potentials of -0.3 V and +0.3 V were applied for 1h alternately. The coloration and bleaching state processes were recorded at the wavelength of 555 nm.

IV. Results and Discussion

4.1 XRD

Fig. 1 shows XRD results of the as-prepared samples. Fig. 1a is almost identical to Fig. 1b, which suggests that the WO_3 films deposited on the ITO glass were probably amorphous, e.g., no new peaks appearing compared to the ones for the ITO substrate. However, after the heat treatment the XRD pattern in Fig. 1c showed several new peaks, indicating the recrystallization of WO_3 at elevated temperatures. The newly formed crystalline phase may be assigned to monoclinic WO_3 (PDF 00-043-1035) based on the observed strong reflections.

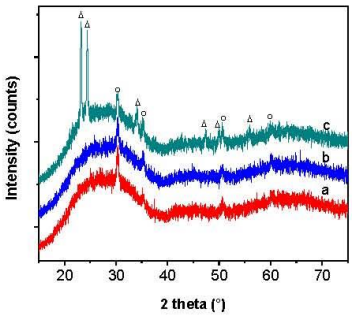

Fig. 1. XRD results of (a) ITO glass substrate, (b) WO_3 films before heat treatment, and (c) WO_3 films after heat treatment. Open circles (□○) denote the reflections of ITO (PDF 04-019-3926). Open triangles (Δ) denote the reflections of monoclinic WO_3 (PDF 00-043-1035).

4.2 SEM

The SEM results are shown in Fig. 2. Fig. 2a shows that the as-prepared WO_3 film before heat treatment had a flat, smooth surface. After the heat treatment, window ice-like crystals were formed (Fig. 2b). That means heat treatment can help the crystal formation on the surface of the ITO glass.

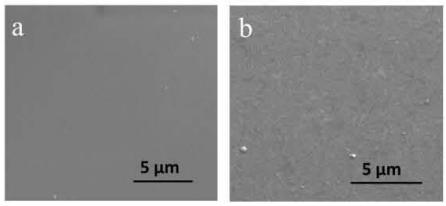

Fig. 2. SEM images of samples. (a) WO_3 thin films deposited on ITO glass substrates before heat treatment, (b) WO_3 thin films deposited on ITO glass substrates after heat treatment.

4.3 FTIR

FTIR results of the samples are shown in Fig. 3. Fig. 3a is the FTIR spectrum of the ITO glass, which is in agreement with previous reports [6]. Fig. 3b shows no new absorbance from the FTIR spectrum of the WO_3 films before the heat treatment. The WO_3 films after heat treatment showed two new absorptions at about 980 and 710 cm^{-1} (Fig. 3c), which are corresponding to W=O and O-W-O stretching vibrations from the newly formed crystalline WO_3 [7]. These absorptions only happened in the crystalline WO_3 film, which is not seen in amorphous WO_3 films.

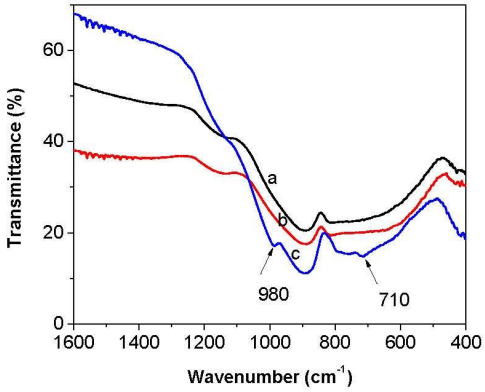

Fig. 3. FTIR spectra of (a) ITO glass, (b) WO_3 film coated on ITO glass before heat treatment, and (c) WO_3 film coated on ITO glass after heat treatment.

4.4 Cyclic Voltammetry

1) Influence of Scan Rate

The kinetic and thermodynamic behaviors of as-prepared WO_3 films after heat treatment were investigated by cyclic voltammetry (CV), which was carried out between -0.3 V and 0.3 V vs. Ag/AgCl at scan rates ranging from 5 to 100 mV/s.

Fig. 4 shows the CV curves. A cathodic current peak emerged at around -0.2 V and an anodic current peak appeared at around 0.05 V when the scan rate was 20 mV/s. These two potentials were accompanied by the coloration (from colorless to blue) and bleaching (from blue to colorless) of the WO_3 films, respectively.

With an increasing scan rate, the anodic potential shifted to higher voltages and the cathodic potential shifted to lower voltages, indicating an increased polarization at higher sweep rates due to kinetic limitations associated with the H^+ diffusion through the active material [8]. The cathodic current peak turned to be hard to find when the scan rate was higher than 60 mV/s.

2) Durability of As-Prepared WO_3 Films

Cycling stability of the as-prepared WO_3 films was evaluated and the results were shown in Fig. 5. No obvious changes were observed during the first 200 scans, whereas the film began to decompose after about 250 scans. The decomposition is due to the acidic environment with oxygen in the electrolyte. Increasing the cycling voltage to 0.5 V reduce stability of the WO_3 films. For example, the film began to decompose after about 120 scans.

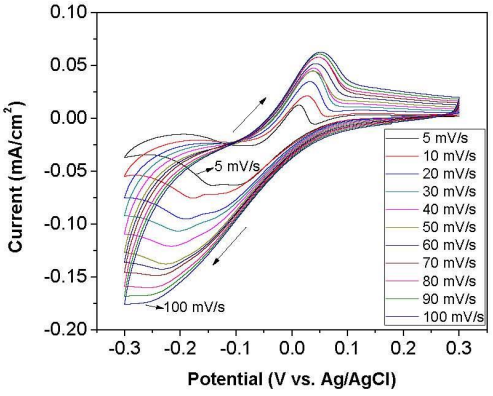

Fig. 4. CV scans of a WO_3 thin film deposited on ITO glass substrate after heat treatment. WE: WO_3 films, CE: Pt wire, RE: Ag/AgCl (3 M KCl), electrolyte: 0.5 M H_2SO_4. Scan rates were 5, 10, 20, 30, 40, 50, 60, 70, 80, 90 and 100 mV/s.

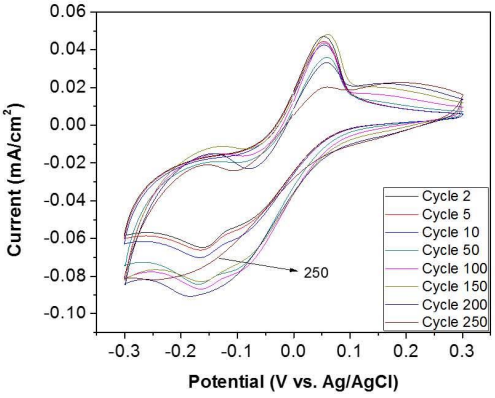

Fig. 5. CV scans of a WO_3 thin film after heat treatment. Scan rate is 20 mV/s.

4.5 UV-VIS-NIR Spectroscopy

UV-VIS-NIR spectroscopy was utilized to characterize the WO_3 films. As shown in Fig. 6, the transmittance spectrum in the wavelength range 280 to 1300 nm of the WO_3 thin film at the colored state was compared with that of the bleached state. The colored and bleached samples were obtained from as-prepared samples after Autolab procedure chrono amperometry experiments. A potential of -0.3 V was applied to the colored samples for 3600 s. Similarly, a potential of +0.3 V was applied to the bleached samples for

3600 s. Fig. 6 shows the spectrum of the bleached state (a) and the colored state (b) in the 4th cycle. The largest transmittance difference ΔT was 59.1% at wavelength λ=1300 nm, whereas ΔT was around 20% at λ=555 nm.

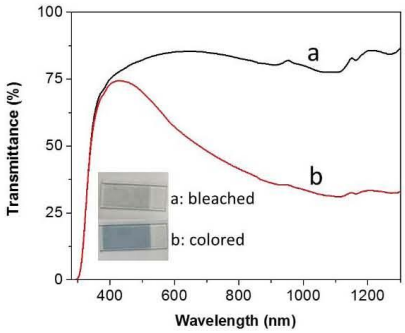

Fig. 6. Transmittance spectra of a WO_3 thin film electrode at (a) bleached state at +0.3 V and (b) colored state at -0.3 V. Inset shows an optical photo of the corresponding sample states.

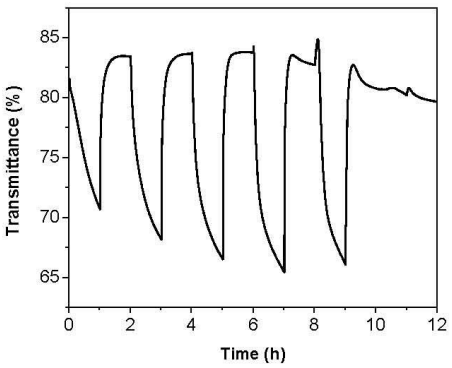

Fig. 7. Transmittance of 36 nm WO_3 thin film electrode response to Autolab procedure chronoamperometry: potentials -0.3 V for 1 h and 0.3 V for 1 h. Transmittance spectra was recorded at 555 nm.

Fig. 7 shows the colored and bleached process which was recorded at λ=555 nm from 0 to 12 h. Firstly, the potential of -0.3V was applied in the 1st hour. Subsequently, the potential of +0.3 V was applied in the 2nd hour. Furthermore, the recycled potentials of -0.3 V and +0.3 V were applied from the third hour to the 12th hour. The WO_3 film changed color from colorless to blue by the negative potential and was bleached by the positive potential. The bleached transmittance reached a steady value (84%) for each cycle, whereas the colored transmittance value turned to be lower and lower from first to the 4th cycle. That is, the colored process had not completed during 1 h. The 5th transmittance value was higher than its former one due to influence of some degradation, which happened after around 8 h. The film lost its color changing properties almost completely after 10 hours, i.e. the film has been degraded. It seems the system can not stand the acidic environment with oxygen in the electrolyte for a prolonged time. However, this may be solved by fabricating an oxygen-free EC device (e.g. using a glovebox in the laboratory).

V. Conclusions

In this work, a radio frequency sputtering method was developed for WO_3 film preparation in order to control the thickness of films accurately at nano scale. WO_3 thin films with a typical thickness of about 36 nm were prepared and their structural and physical properties were investigated. The films before heat treatment were amorphous. However, crystals were formed during heat treatment. The amorphous films could not change color under applied potential, whereas the crystalline films demonstrated good EC abilities.

The EC properties were investigated using cyclic voltammetry analysis and UV-VIS-NIR spectroscopy. At a scan rate of 20 mV/s, the color of the WO_3 films changed at around -0.2 V and bleached at around 0.05 V. The WO_3 films could be cycled for 200 times between the potentials -0.3 V to 0.3 V.

Acknowledgments

This work has been supported by the Research Council of Norway and several partners through "The Research Centre on Zero Emission Buildings" (ZEB) (project no. 193830). The authors gratefully acknowledge The Research Council of Norway for the support to the Norwegian Micro- and Nano-Fabrication Facility, NorFab (project no. 245963/F50).

References

[1] T. Gao, B.P. Jelle and A. Gustavsen, "Nanoelectrochromics with applied materials and methodologies", *Zero Emission Buildings–Proceedings of the Renewable Energy Research Conference*, Trondheim, Norway, pp. 61-71, 2010.

[2] B. P. Jelle and G. Hagen, "Transmission spectra of an electrochromic window based on polyaniline, prussian blue and tungsten oxide", *Journal of the Electrochemical Society*, vol.140, pp. 3560-3564, 1993.

[3] T. Gao, B. P. Jelle and A. Gustavsen, "Synthesis and characterization of sodium tungsten bronze nanorods for electrochromic smart window applications", in *Nanotechnology (IEEE-NANO), 13th IEEE Conference*, pp. 1093-1096, 2013.

[4] T. Gao and B. P. Jelle, "Visible-light-driven photochromism of hexagonal sodium tungsten bronze nanorods," *Journal of Physical Chemistry C*, vol. 140, pp.13753-13761, 2013.

[5] B. P. Jelle, G. Hagen and Ø. Birketveit, "Transmission properties for individual electrochromic layers in solid state devices based on polyaniline, prussian blue and tungsten oxide", *Journal of Applied Electrochemistry*, vol. 28, pp. 483-489, 1998.

[6] L. Meng and M. P. Dos Santos, "Properties of indium tin oxide (ITO) films prepared by r.f. reactive magnetron sputtering at different pressures", *Thin Solid Films*, vol. 303, pp. 151-155, 1997.

[7] M. F. Daniel, B. Desbat, J. C. Lassegues, B. Gerand and M. Figlarz, "Infrared and Raman study of WO_3 tungsten trioxides and WO_3, xH_2O tungsten trioxide tydrates", *Journal of Solid State Chemistry*, vol. 67, pp. 235-247, 1987.

[8] P. Hu, J. Ma, T. Wang, B. Qin, C. Zhang, C. Shang, J. Zhao and G. Cui, "NASICON-structured $NaSn_2(PO_4)_3$ with excellent high-rate properties as anode material for lithium ion batteries", *Chemistry of Materials*, vol. 27, pp. 6668-6674, 2015.

Paper 2

Electrochromic Properties of WO_3 Thin Films: The Role of Film Thickness

Analytical science Advances 2020, 1 (2), 124–131.

Received: 9 June 2020 | Revised: 2 July 2020 | Accepted: 6 July 2020

DOI: 10.1002/ansa.202000072

ANALYTICAL SCIENCE ADVANCES

WILEY-VCH

FULL ARTICLE

Electrochromic properties of WO_3 thin films: The role of film thickness

Yingpeng Zhen[1] | Bjørn Petter Jelle[1,2] | Tao Gao[1]

[1] Department of Civil and Environmental Engineering, Norwegian University of Science and Technology (NTNU), Trondheim, Norway

[2] Department of Materials and Structures, SINTEF Community, Trondheim, Norway

Correspondence
Yingpeng Zhen, Department of Civil and Environmental Engineering, Norwegian University of Science and Technology (NTNU), NO-7491 Trondheim, Norway.
Email: ypzhen521@gmail.com; yingpeng.zhen@ntnu.no

Funding information
the Research Centre on Zero Emission Buildings, Grant/Award Number: 193830; the Research Council of Norway for the support to the Norwegian Micro- and Nano-Fabrication Facility, NorFab, Grant/Award Number: 245963/F50

Abstract

Tungsten oxide (WO_3) thin films with various thicknesses of approximately 36, 72, 108, and 180 nm were prepared using radio frequency sputtering method. Film thickness can be controlled at nanoscale. In addition, X-ray diffraction, scanning electron microscopy, and Fourier transform infrared spectroscopy were utilized for investigating morphologies and microstructures of as-prepared WO_3 thin films. Moreover, optical properties of the WO_3 nanofilms were characterized using ultraviolet-visible-near infrared spectroscopy. Transmittance of WO_3 films changed during the electrochemical cycles. WO_3 films with various thicknesses give various transmittance modulation between colored and bleached states. WO_3 films with a thickness of approximately 108 nm had the largest transmittance modulation among various film thicknesses, about 66% measured at 550 nm. Results showed that the value of transmittance of colored samples decreased with increasing film thickness. However, transmittance of bleached samples was not influenced significantly by their thickness.

KEYWORDS
electrochromic windows, nanofilm thickness, smart windows, thin nanofilm, tungsten oxide

1 | INTRODUCTION

Energy consumption and greenhouse gas emission of buildings account for a large part of total energy consumption and CO_2 emissions in both developed and developing countries in the world. A building may lose about 30% of its heat or air conditioning energy through its windows, because windows have usually poor thermal insulation properties and high radiation transmittance. Windows with low *U*-value (*U*-value of window can be utilized to measure heat transfer rate through window; normally, window with a lower *U*-value will have a lower amount of heat loss, and will also have a better thermal insulation property) have been widely used in buildings to prevent heat loss by heat transfer (thermal conduction, thermal convection, and radiation). Chromogenic smart windows have been used for regulating solar radiation transmitted through the windows into buildings. Therefore, energy consumption of buildings can be reduced. However, nowadays, chromogenic smart windows are not widely utilized in normal buildings.

Chromogenic smart windows can adjust solar radiation transmitted through windows by regulating transmittance value. Glass with functional film of chromogenic smart windows can change windows transmittance value if functional film materials of glass are sensitive to voltage, solar radiation, heat, and so on. Different chromogenic smart windows are made of different chromogenic materials. Based on various chromogenic materials, there are photochromic smart windows, thermochromic smart windows, gasochromic smart windows, and electrochromic smart windows.

Electrochromic material is a type of chromogenic material. Electrochromic material is sensitive to an external applied voltage. The most popular electrochromic material is transition metal oxide, which may be divided into two types: (a) anodic coloration materials and (b) cathodic coloration materials. Anodic coloration materials include NiO,[1] Co_2O_3,[2] $Ir(OH)_3$,[3] V_2O_5,[4] and so forth. The cathodic coloration materials include tungsten oxide (WO_3),[5] MoO_3,[5,6] TiO_2,[7] and so forth. Many different electrochromic polymers have also been investigated.[8–10]

WO_3 is one of the most studied electrochromic materials for electrochromic smart window applications. There are many kinds of methods utilized for WO_3 film preparation, such as evaporation,[11] sputtering,[12] electrodeposition,[13] chemical vapor deposition,[14] and sol-gel deposition.[15]

Electrochromic materials and devices[16–22] were investigated in our previous work. WO_3 thin films were prepared using a radio frequency (RF) sputtering technology, which enables to control the film thickness accurately at nanometer scale. WO_3 thin films with various thicknesses were prepared. The role of the film thickness on structural and optical properties of WO_3 films was investigated. Microstructure of as-prepared WO_3 thin films was characterized using X-ray diffraction (XRD), scanning electron microscope (SEM), and Fourier transform infrared (FTIR) spectroscopy. Electrochemical properties of as-prepared WO_3 films were characterized using cyclic voltammetry (CV). Ultraviolet-visible-near infrared (UV-Vis-NIR) spectroscopy was utilized to analyze optical properties of WO_3 films.

2 | EXPERIMENTAL SECTION

2.1 | Materials

WO_3 sputtering target (diameter = 5.08 cm; thickness = 0.32 cm) was purchased from AJA International Inc., USA. Substrates for growth of WO_3 thin films were ITO (tin doped indium oxide, In_2O_3(Sn)) glass slides, which have been purchased from Sigma-Aldrich (Transmittance: approximately 86% at 550 nm; Surface resistivity: about 70-100 Ω/square; Size: about 25 mm × 25 mm × 1.1 mm). The ITO glass slides were cut to small pieces with sizes of about 9.2 mm × 25 mm × 1.1 mm in this work. Reagent grade sulfuric acid (H_2SO_4, 96 wt%) and potassium chloride (KCl, 99%) were also purchased from Sigma-Aldrich. Distilled water from our laboratory was utilized in this work.

2.2 | Preparation of WO_3 films

First, ITO glass slides were washed with ethanol under ultrasonic irradiation. And then ITO glass slides were washed with distilled water. In the end, ITO glass slides were dried using nitrogen gas. Preparation process of WO_3 films was similar to our previous work.[23] In brief, WO_3 films were prepared by RF magnetron sputtering via an AJA sputter and evaporator (model: Custom ATC-2200V, AJA International Inc. USA). RF power was set to 120 W and the ramp up time was 210 s. Sputtering rate has been checked as 0.05 nm/s before the sample sputtering process. ITO glass substrates were loaded into sample holder. Argon (Ar) flow was 67 sccm (standard cubic centimeter per minute). Plasma strike pressure was 30 mTorr (approximately 4.0 Pa) Ar pressure. Strike power is 50 W. After plasma was strike on, Ar pressure was changed and maintained at 3 mTorr (approximately 0.4 Pa) during plasma processes. After RF power reached set value, 1 min was spent to wait for the stability of plasma. Subsequently, the shutter that covered the target is opened during sputtering process. And then the shutter was closed as long as the desired film thickness was reached, for example, 720 s for film with thickness as 36 nm. In the end, after the power was decreased to 50 W, the plasma was turned off.

Heat treatment was also performed to the sputtered films in air at 400°C for 5 h. By this way, as-prepared samples were obtained in this work for further investigation.

2.3 | Characterization

XRD patterns of as-prepared samples were collected on a D8 A25 DaVinci X-ray diffractometer (Bruker, Germany) with Cu-Kα radiation. XRD data were collected in the range of 15°-75° with a step size of 0.013°. The surface topography of samples was investigated using an Apreo SEM from Thermo Fisher Scientific (FEI, USA). Attenuated total reflectance (ATR) FTIR spectra were recorded on a Nicolet 8700 FTIR Spectrometer (Thermo Scientific, USA). A horizontal single-bounce ATR diamond accessory was utilized for FTIR characterization. The spectra were recorded in wavenumbers ranging from 400 to 4000 cm^{-1} at a spectral resolution of 2 cm^{-1}.

CV measurements were conducted using a potentiostatic procedure at a scan rate of 20 mV/s in the potential range from −0.5 to 1.0 V versus Ag/AgCl on an AutoLab PGSTAT302N electrochemical workstation (Metrohm Autolab B.V., Netherlands). A standard three-electrode electrochemical cell was assembled, where a WO_3 film, a Pt film, and a reference electrode (Ag/AgCl, 3 M KCl) were used as working electrode, counter electrode, and reference electrode, respectively. The electrolyte was 0.5 M H_2SO_4 aqueous solution. Experiments were performed under atmospheric environment.

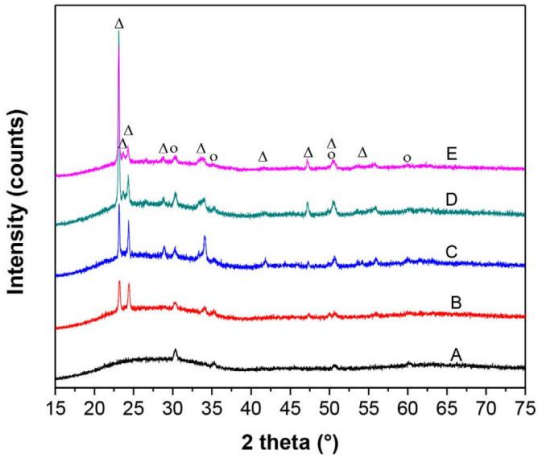

FIGURE 1 XRD results of as-prepared WO_3 nanofilm samples: (A) ITO glass, (B) 36-nm WO_3 nanofilm, (C) 72-nm WO_3 nanofilm, (D) 108-nm WO_3 nanofilm, and (E) 180-nm WO_3 nanofilm. Open circles (O) denote the reflections of ITO (Powder Diffraction File [PDF] 04-019-3926). Open triangles (Δ) denote the reflections of monoclinic WO_3 (PDF 00-043-1035)

Transmittance of samples was measured in the wavelength ranging from 280 to 1300 nm using a UV-Vis-NIR spectrophotometer (PerkinElmer 1050 WB, USA). Samples were measured in situ when they were utilized as working electrodes in an electrochemical system. Because H_2SO_4 solution electrolyte had a strong absorption to light with wavelength above 1350 nm. Transmittance spectra were recorded from 280 to 1300 nm. A constant potential of −0.5 and +1.0 V (vs Ag/AgCl, 3 M KCl) was used to color and bleach samples, respectively.

3 | RESULTS AND DISCUSSIONS

3.1 | X-ray diffraction

Figure 1 depicts XRD patterns of WO_3 films with four various thicknesses, namely, 36, 72, 108, and 180 nm. XRD peaks of ITO substrates (Figure 1A) matched well with the work of Kim et al.[24] All WO_3 films showed similar diffraction peaks (Figure 1B-E). The peaks at 23.1°, 23.6°, and 24.4° can be assigned to (002), (020), and (200) reflections of the monoclinic WO_3 (Powder Diffraction File 00-043-1035), respectively. XRD results showed that as-prepared WO_3 films with various thickness of 36, 72, 108, and 180 nm had the same monoclinic crystal structure.

3.2 | Fourier transform infrared spectroscopy

Chemical structure of the obtained films was also characterized using FTIR (as shown in Figure 2). FTIR results showed that there were absorption peaks at approximately 900 and 760 cm^{-1} for ITO glass, which was in agreement with the work of Meng and Santos.[25] The absorption peak at about 980 cm^{-1} is related to W = O stretching vibrations, whereas the absorption peak at about 585 cm^{-1} is corresponding to O-W-O stretching vibrations from the crystalline WO_3.[18,26] FTIR results showed that as-prepared WO_3 films with various thickness of 36, 72, 108, and 180 nm had similar crystalline structure. The FTIR result was in agreement with XRD result.

3.3 | Scanning electron microscope

Morphology of WO_3 films was investigated using SEM. As shown in Figure 3, crystals were formed in all the as-prepared WO_3 films. These films showed different colors, including light gray, light blue, lemon green, and brown. The crystals did not cover the whole substrate completely when the WO_3 film thickness was 36 and 72 nm (as shown in Figures 3A and 3B). However, as was shown in samples of WO_3 film with thickness of 108 and 180 nm, with the increase of film thickness, crystals covered almost the whole substrate (Figures 3C and 3D).

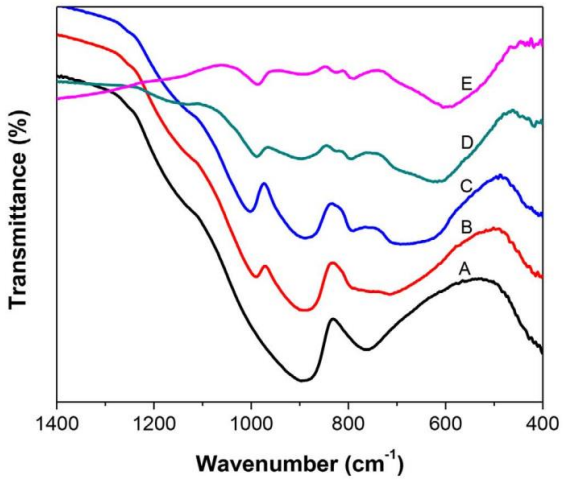

FIGURE 2 FTIR spectra of as-prepared WO_3 nanofilm samples: (A) ITO glass, (B) 36-nm WO_3 nanofilm, (C) 72-nm WO_3 nanofilm, (D) 108-nm WO_3 nanofilm, and (E) 180-nm WO_3 nanofilm

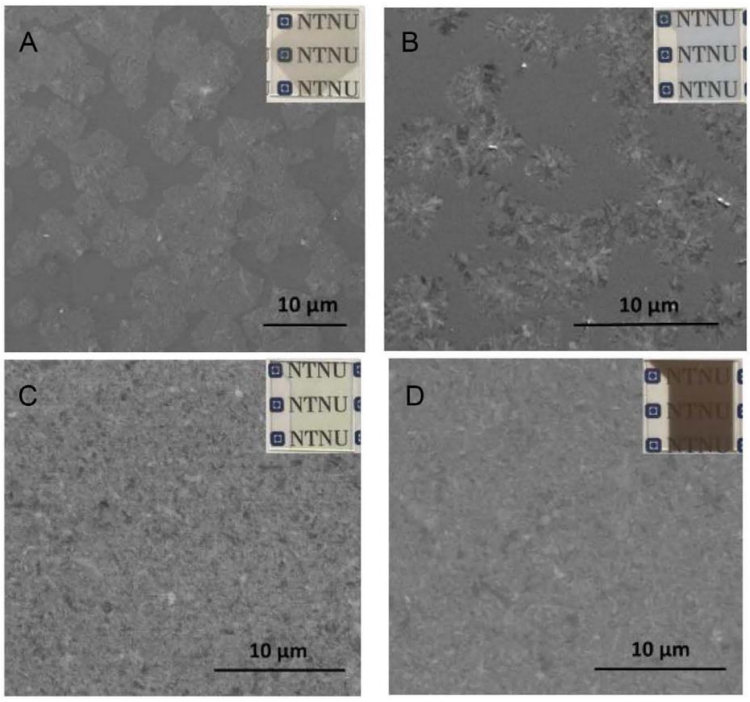

FIGURE 3 Photos of glass with as-prepared WO_3 films and SEM images of as-prepared WO_3 films with various thicknesses: (A) 36 nm, (B) 72 nm, (C) 108 nm, and (D) 180 nm WO_3 film

3.4 | Cyclic voltammetry

Electrochemical properties of as-prepared WO_3 films were investigated by CV method, which was carried out between −0.5 and 1.0 V versus Ag/AgCl (3 M KCl) at a scan rate of 20 mV/s. Figure 4 showed the CV curves experimental results. WO_3 thin films with various thicknesses exhibited similar CV curves. A cathodic current peak emerged at around −0.1 V and an anodic current peak appeared at around 0.1 V. The two peaks were

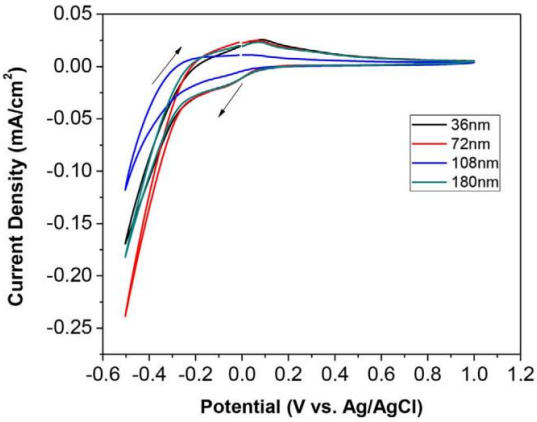

FIGURE 4 CV curves of WO_3 thin films with various film thicknesses of 36, 72, 108, and 180 nm at a scanning rate of 20 mV/s

TABLE 1 Transmittance of WO_3 films at colored and bleached states at a wavelength of $\lambda = 550$ nm (measured in 0.5 M H_2SO_4 aqueous electrolyte solution)

WO_3 film thickness (nm)	$T_{550\,nm}$ bleached state (%)	$T_{550\,nm}$ colored state (%)	$\Delta T_{550\,nm}$ between bleached and colored state (%)
36	82	66	16
72	85	44	41
108	94	28	66
180	29	8	21

accompanied by the coloration (from colorless to blue, ie, $W^{6+} \rightarrow W^{5+}$) and bleaching (from blue to colorless, ie, $W^{5+} \rightarrow W^{6+}$) of the WO_3 films, respectively. The redox peaks were not influenced by the film thickness of WO_3.

3.5 | UV-Vis-NIR spectroscopy

UV-Vis-NIR spectroscopy was utilized to characterize WO_3 films. The colored samples were obtained by applying an external potential voltage of −0.5 V to as-prepared samples for 5 h, whereas the transmittance of bleached samples were obtained from as-prepared samples before any external potential voltage was applied. Bleached experiments were performed by applying an external potential voltage of +1.0 V to as-prepared samples for 5 h. However, it was found that the transmittance of bleached samples after an external potential voltage of +1.0 V was applied for 5 h was almost the same as they were before an external potential voltage of +1.0 V was applied. Transmittance spectra of WO_3 films were shown in Figure 5. The samples were measured in a self-made cuvette filled with 0.5 M H_2SO_4. As shown in Figure 5A, at a wavelength of $\lambda = 550$ nm, the transmittance value (T) of the 36 nm sample was about 66% at the colored state and 82% at the bleached state. This resulted in a transmittance modulation (ΔT) of about 16% at 550 nm ($\Delta T_{550\,nm}$).

The transmittance spectra of the colored and bleached samples with thicknesses of 72, 108, and 180 nm were shown in Figures 5B, 5C, and 5D, respectively. T of the samples in the bleached state and colored state at a wavelength of $\lambda = 550$ nm were obtained and given in Table 1. $\Delta T_{550\,nm}$ of the samples with thickness of 36, 72, 108, and 180 nm were 16%, 41%, 66%, and 21%, respectively. From these results, it can be seen that the as-prepared WO_3 film with thickness of 108 nm had the largest ΔT of about 66% at 550 nm.

The largest T of bleached samples was obtained from WO_3 film with thickness of 108 nm. It is shown that the WO_3 coating thickness increase did not always make T decrease with the increasing of nanofilm thickness from 36 nm to 180 nm. $T_{550\,nm}$ of bleached films decreased with nanofilm thickness of 108 nm (highest transmittance), 72 nm, 36 nm and 180 nm (lowest transmittance).

To further prove results above, transmittance of bleached samples (as prepared WO_3 films without further treatment) were measured in air. The transmittance curves of the bleached samples were shown in figure 6.

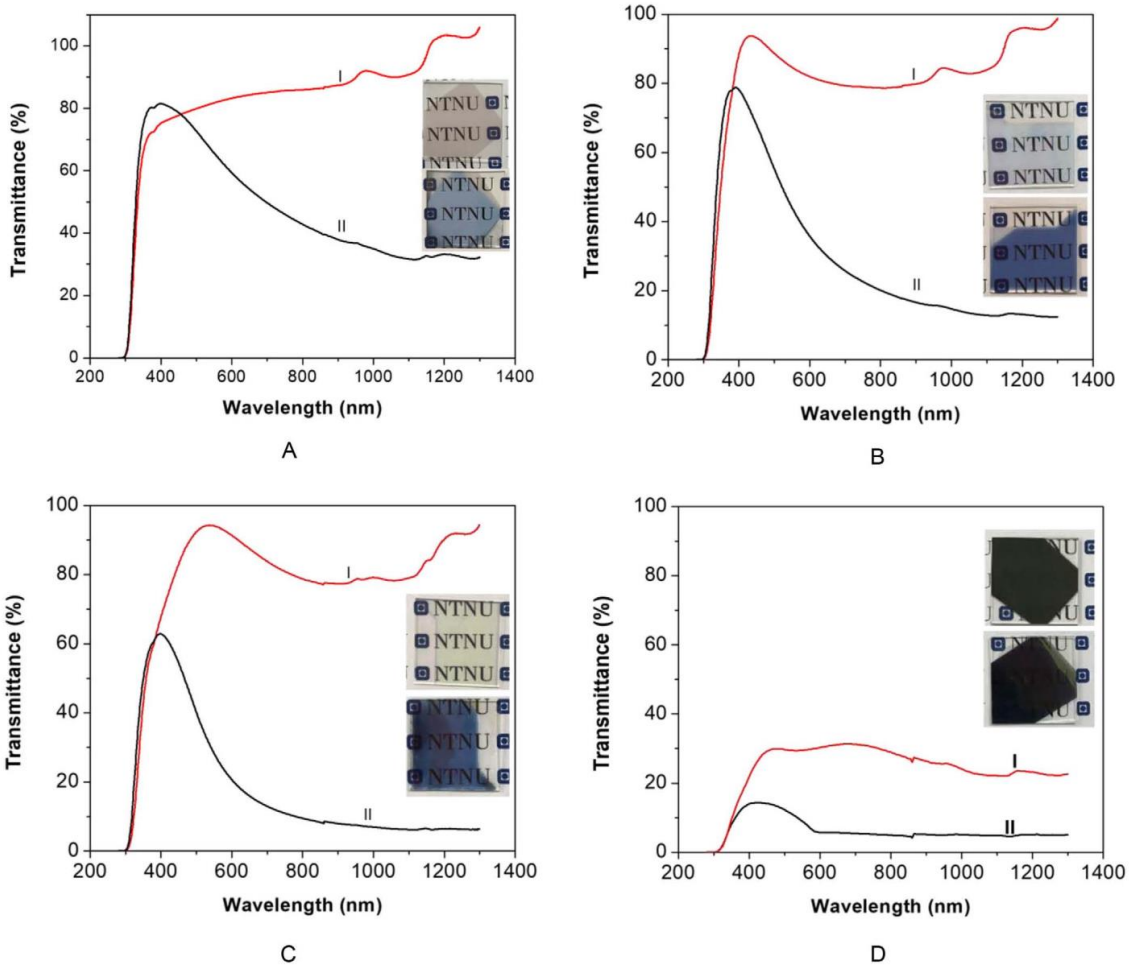

FIGURE 5 Transmittance spectra of WO_3 thin-film samples with various film thicknesses: (A) 36 nm, (B) 72 nm, (C) 108 nm, and (D) 180 nm in the bleached state (I) and colored state (II). Inset shows the corresponding photos of as-prepared WO_3 films at bleached (up) and colored (down) state (measured in 0.5 M H_2SO_4)

Figure 6 depicts the transmittance spectra of bleached WO_3 films in the wavelength ranging from 280 to 3300 nm, which were measured in a standard optical glass cuvette with no liquid filled. It was shown that the transmittance order was different at different range of wavelength. Transmittance of bleached films decreased by the increase of thickness in the wavelength ranging from 935 to 3300 nm. However, in the wavelength ranging from 390 to 495 nm, the film with thickness of 72 nm had the highest transmittance among all the films utilized in this work. At wavelength ranging from 495 to 740 nm, the film with thickness of 108 nm had the highest transmittance compared to the other films. From Figure 6, the order of transmittance values of various bleached films at wavelength of 550 nm was 108-nm film (highest transmittance), 72-nm film, 36-nm film, and 180-nm film (lowest transmittance). These results were in agreement with results showed in Table 1.

4 | CONCLUSIONS

In this work, WO_3 thin films with various thicknesses of approximately 36, 72, 108, and 180 nm were prepared. Morphologies and microstructures of as-prepared WO_3 thin films were characterized using XRD, SEM, and FTIR. In addition, UV-Vis-NIR spectroscopy was utilized for transmittance investigations of WO_3 films. The bleached WO_3 films showed color as light gray, light blue, lemon green, and brown, whereas the colored films

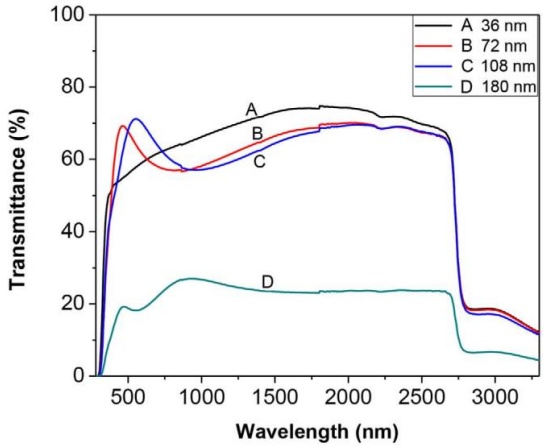

FIGURE 6 Transmittance spectra of WO_3 thin film with various film thicknesses: (A) 36 nm, (B) 72 nm, (C) 108 nm, and (D) 180 nm at the bleached state (measured in air)

showed color as blue with different transmittance levels. WO_3 films with various thicknesses lead to various transmittance values at the colored and bleached state. Among WO_3 film samples with thickness of 36, 72, 108, and 180 nm, the largest transmittance modulation $\Delta T_{550\,nm}$ was obtained from sample with thickness of 108 nm, which was approximately 66% when measured in 0.5 M H_2SO_4. It showed that the value of transmittance of colored samples decreased with increasing of their thickness, whereas the transmittance of bleached samples was not affected by their thicknesses. This work will benefit electrochromic smart window development.

CONFLICT OF INTEREST

The authors declare no conflict to declare.

ACKNOWLEDGMENTS

This work has been supported by the Research Council of Norway and several partners through "the Research Centre on Zero Emission Buildings" (ZEB) (project no. 193830). The authors gratefully acknowledge the Research Council of Norway for the support to the Norwegian Micro- and Nano-Fabrication Facility, NorFab (project no. 245963/F50).

ORCID

Yingpeng Zhen https://orcid.org/0000-0001-5238-5131

REFERENCES

1. Xia XH, Tu JP, Zhang J, Wang XL, Zhang WK, Huang H. Electrochromic properties of porous NiO thin films prepared by a chemical bath deposition. *Sol Energy Mater Sol Cells*. 2008;92(6):628-633.
2. Xia XH, Tu JP, Zhang J, Xiang JY, Wang XL, Zhao XB. Cobalt oxide ordered bowl-like array films prepared by electrodeposition through monolayer polystyrene sphere template and electrochromic properties. *ACS Appl Mater Interfaces*. 2010;2(1):186-192.
3. Gottesfeld S, McIntyre JDE, Beni G, Shay JL. Electrochromism in anodic iridium oxide films. *Appl Phys Lett*. 1978;33(2):208-210.
4. Li Y-M, Kudo T. Properties of mixed-oxide MoO_3/V_2O_5 electrochromic films coated from peroxo-polymolybdovanadate solutions. *Sol Energy Mater Sol Cells*. 1995;39(2):179-190.
5. Faughnan BW, Crandall RS. Optical properties of mixed-oxide WO_3/MoO_3 electrochromic films. *Appl Phys Lett*. 1977;31(12):834-836.
6. Hsu C-S, Chan C-C, Huang H-T, Peng C-H, Hsu W-C. Electrochromic properties of nanocrystalline MoO_3 thin films. *Thin Solid Films*. 2008;516(15):4839-4844.
7. Yoshimura K, Miki T, Tanemura S. TiO_2 electrochromic thin films by reactive direct current magnetron sputtering. *J Vac Sci Technol A*. 1997;15(5):2673-2676.
8. Natera J, Otero L, Sereno L, et al. A novel electrochromic polymer synthesized through electropolymerization of a new donor—acceptor bipolar system. *Macromolecules*. 2007;40(13):4456-4463.
9. Mortimer RJ, Dyer AL, Reynolds JR. Electrochromic organic and polymeric materials for display applications. *Displays*. 2006;27(1):2-18.
10. DeLongchamp DM, Kastantin M, Hammond PT. High-contrast electrochromism from layer-by-layer polymer films. *Chem Mater*. 2003;15(8):1575-1586.
11. Reichman B, Bard AJ. The electrochromic process at WO_3 electrodes prepared by vacuum evaporation and anodic oxidation of W. *J Electrochem Soc*. 1979;126(4):583-591.

12. Washizu E, Yamamoto A, Abe Y, Kawamura M, Sasaki K. Optical and electrochromic properties of RF reactively sputtered WO_3 films. *Solid State Ion.* 2003;165(1):175-180.
13. Srivastava AK, Deepa M, Singh S, Kishore R, Agnihotry SA. Microstructural and electrochromic characteristics of electrodeposited and annealed WO_3 films. *Solid State Ion.* 2005;176(11):1161-1168.
14. White CM, Gillaspie DT, Whitney E, Lee S-H, Dillon AC. Flexible electrochromic devices based on crystalline WO_3 nanostructures produced with hot-wire chemical vapor deposition. *Thin Solid Films.* 2009;517(12):3596-3599.
15. Deepa M, Sharma N, Varshney P, Varma SP, Agnihotry SA. FTIR investigations of solid precursor materials for sol-gel deposition of WO_3 based electrochromic films. *J Mater Sci.* 2000;35(21):5313-5318.
16. Jelle BP, Hagen G. Transmission spectra of an electrochromic window based on polyaniline, Prussian blue and tungsten oxide. *J Electrochem Soc.* 1993;140(12):3560-3564.
17. Gao T, Jelle BP, Gustavsen A, eds. *Synthesis and Characterization of Sodium Tungsten Bronze Nanorods for Electrochromic Smart Window Applications.* 13th IEEE International Conference on Nanotechnology (IEEE-NANO 2013); 5-8 Aug 2013.
18. Gao T, Jelle BP. Visible-light-driven photochromism of hexagonal sodium tungsten bronze nanorods. *J Phys Chem C.* 2013;117(26):13753-13761.
19. Jelle BP, Hagen G, Birketveit Ø. Transmission properties for individual electrochromic layers in solid state devices based on polyaniline, Prussian blue and tungsten oxide. *J Appl Electrochem.* 1998;28(5):483-489.
20. Jelle BP, Gustavsen A, Nilsen TN, Jacobsen T. Solar material protection factor (SMPF) and solar skin protection factor (SSPF) for window panes and other glass structures in buildings. *Sol Energy Mater Sol Cells.* 2007;91(4):342-354.
21. Jelle BP. Solar radiation glazing factors for window panes, glass structures and electrochromic windows in buildings-measurement and calculation. *Sol Energy Mater Sol Cells.* 2013;116:291-323.
22. Gao T, Jelle BP. Electrochromism of hexagonal sodium tungsten bronze nanorods. *Sol Energy Mater Sol Cells.* 2018;177:3-8.
23. Zhen Y, Gao T, Jelle BP, eds. *Synthesis and Characterization of Tungsten Oxide Electrochromic Thin Films.* 2018 IEEE 18th International Conference on Nanotechnology (IEEE-NANO); 23-26 July 2018.
24. Kim H, Gilmore CM, Piqué A, et al. Electrical, optical, and structural properties of indium–tin–oxide thin films for organic light-emitting devices. *J Appl Phys.* 1999;86(11):6451-6461.
25. Meng L-j, dos Santos MP. Properties of indium tin oxide (ITO) films prepared by r.f. reactive magnetron sputtering at different pressures. *Thin Solid Films.* 1997;303(1):151-155.
26. Balázsi C, Pfeifer J. Long-term behaviour of tungsten oxide hydrate gels in an alkali containing aqueous environment. *Sol Energy Mater Sol Cells.* 2003;76(4):577-590.

How to cite this article: Zhen Y, Jelle BP, Gao T. Electrochromic properties of WO_3 thin films: The role of film thickness. *Anal Sci Adv.* 2020;1:124–131. https://doi.org/10.1002/ansa.202000072

Paper 3

Influence of O_2 on Electrochromic WO_3 Thin Films Preparation Using Radio Frequency Sputtering

(Under Review)

Paper 4

Electrochromic Materials and their Characterization by Solar Radiation Glazing Factors for Smart Window Applications

International Conference on Smart Materials and Surfaces - SMS Bangkok 2014

Smart Materials and Surfaces

SMS Bangkok 2014 International Conference Proceeding

www.setcor.org/conferences/SMS-Bangkok-2014

Table of contents

Smart Materials and Surfaces: Fabrication, Characterization & Properties

Smart Materials and Surfaces for Energy and Environment

	O. Abbes, A. Portavoce, C. Girardeaux, A. Spiesser, and V. Le Thanh GREMI CNRS-Université d'Orléans, Aix-Marseille Université, CNRS, IM2NP-UMR 6242 and Aix-Marseille Université, CNRS, CINaM-UMR 7325, Marseille, **France**
10	**Strength and Ductility of SGFRP Confined Concrete**
	Q. Hussain, A. Pimanmas and **L. Lalin**, Sirindhorn International Institute of Technology, Thammasat University, Thailand.
11	**Smart Focused-Ion-Beam-fabricated Nanostructures for Improving Sur-face Enhanced Raman Scattering on Trace Detection of Single Molecules**
	K. Sivashanmugan, J-D Liao and C-K Yao Department of Materials Science and Engineering, Center for Micro/Nano Science and Technology, Nation-al Cheng Kung University, **Taiwan**.
12	**Nanostructured metal oxides: catalyst-free synthesis, characterization and Integration with MEMS processing for gas sensor**
	S. Chandra and B. Behera Centre for applied Research in Electronics, Indian Institute of Technology Delhi, India
13	**A Microscale Piezoelectric Harvester for Mechanical Energy from Fluid Flow**
	K. Koyvanich, N. Muensit and P. Smithmaitrie Center of Excellence in Nanotechnology for Energy (CENE), Physics Department, Faculty of Science and Department of Mechanical Engineering, Faculty of Engineering, Prince of Songkla University (PSU), HatYai, Songkla, **Thailand.**
14	**Effect of electron beam on thermal, morphological and anti-oxidant properties of kraft lignin**
	T.Venkatappa Rao, N.Rajeswara Rao, SVS Ramana Reddy and B.Sanjeeva Rao National Institute of Technology, Warangal, **India**
15	**Facile growth of carbon nanotube electrode from electroplated Ni catalyst for supercapacitors**
	V. Yordsri, **W. Wongwiriyapan** and C. Thanachayanont College of Nanotechnology, King Mongkut's Institute of Technology Ladkrabang/ Nanotec-KMITL Center of Excellence on Nanoelectronic Device/ Thailand Center of Excellence in Physics/ National Metal and Materials Technology Center, **Thailand**

Smart Materials and Surfaces for life science

1.	**Immobilization of Urease Based on Adsorption in Eggshell Membrane for Urea Biosensor Application**
	T. Suwanchaituch, S. Imthong and **K. Panpae** Department of Chemistry, Faculty of Science, King Mongkut's University of Technology Thonburi, KMUTT, Bangkok, **Thailand**
2.	**Needle-less Jet Injection System with Multi-Pore Nozzle for Viscous Drug Delivery Applications**
	Y. C. Jo, H. K. Hong, Y. S. Choi and H. S. Kim Korea Electronics Technology Institute, Medical IT Convergence Research Center, SeongNam-Si and Korea Electronics Technology Institute, Contents Research Center, SeongNam-Si, **South Korea**

Electrochromic Materials and their Characterization by Solar Radiation Glazing Factors for Smart Window Applications

Bjørn Petter Jelle [ab]*, Tao Gao [c], Yingpeng Zhen [b] and Arild Gustavsen [c]

[a] SINTEF Building and Infrastructure,
Department of Materials and Structures, NO-7465 Trondheim, Norway.

[b] Norwegian University of Science and Technology (NTNU),
Department of Civil and Transport Engineering, NO-7491 Trondheim, Norway.

[c] Norwegian University of Science and Technology (NTNU),
Department of Architectural Design, History and Technology, NO-7491 Trondheim, Norway.

* Corresponding author: bjorn.petter.jelle@sintef.no (e-mail), +47-73593377 (phone).

Abstract

Electrochromic materials (ECM) and windows (ECW) are able to regulate the solar radiation throughput by application of an external electrical voltage. Hence, as smart window applications, the ECWs may decrease heating, cooling and electricity loads in buildings by admitting the optimum level of solar energy and daylight into the buildings at any given time, e.g. cold winter climate versus warm summer climate demands. In order to achieve as dynamic and flexible solar radiation control as possible, the ECWs may be characterized by solar radiation glazing factors, i.e. ultraviolet solar transmittance (T_{uv}), visible solar transmittance (T_{vis}), solar transmittance (T_{sol}), solar material protection factor (SMPF), solar skin protection factor (SSPF), external visible solar reflectance ($R_{vis,ext}$), internal visible solar reflectance ($R_{vis,int}$), solar reflectance (R_{sol}), solar absorbance (A_{sol}), emissivity (ε), solar factor (SF) and colour rendering factor (CRF). Comparison of these important solar quantities for various ECM and ECW combinations and configurations enables one to select the most appropriate ones for specific smart window and building applications.

Keywords: Electrochromic, Smart, Material, Window, Solar radiation, Solar factor, Solar heat gain coefficient.

Introduction

The application of electrochromic materials (ECM) in electrochromic windows (ECW) aims at controlling the solar radiation throughput at the earth's surface, which is roughly located between 300 nm and 3000 nm. Such windows are often denoted smart windows. The ECW solar control is achieved by application of an external voltage. The visible (VIS) light lies between 380 and 780 nm. Ultraviolet (UV) and near infrared (NIR) radiation are located below and above the VIS region, respectively. Above 3000 nm, and not part of the direct solar radiation, lies the thermal radiation called infrared (IR) radiation, which all materials radiate above 0 K, peaking around 10 000 nm (10 μm) at room temperature. However, the ECWs are not aimed at controlling the IR radiation. Normally, as low as possible heat loss through windows is desired, i.e. low U-value, which is accomplished by the application of various static low emissivity coatings on the window glass panes. Miscellaneous ECMs and ECWs and their various properties are investigated in the literature [1-10]. Some commercial ECWs are also already on the market [8,9]. ECMs and ECWs may also be used together with other materials and technologies, e.g. self-cleaning glazing materials and building integrated photovoltaics (BIPV) like solar cell glazing [11-15]. In general, it is of major importance to investigate the durability of building materials and components, also newly developed ones like e.g. ECMs and ECWs, which may be performed by carrying out accelerated climate ageing in the laboratory [16]. Thus, conducting a robustness assessment of these materials and components may also be found to be beneficial [17]. Hence, a durability and robustness evaluation of the new ECMs and ECWs should be carried out. This work presents two ECWs and their readily characterization by solar radiation glazing factors, i.e. ultraviolet solar transmittance (T_{uv}), visible solar transmittance (T_{vis}), solar transmittance (T_{sol}), solar material protection factor (SMPF), solar skin protection factor (SSPF), external visible solar reflectance ($R_{vis,ext}$), internal visible solar reflectance ($R_{vis,int}$), solar reflectance (R_{sol}), solar absorbance (A_{sol}), emissivity (ε), solar factor (SF) and colour rendering factor (CRF). The solar factor (SF), which is the total solar energy transmittance, is also often denoted as the solar heat gain coefficient (SHGC) and the g-value. Further details about the solar radiation glazing factors are given in the literature [10,18,19].

Experimental

For various experimental details concerning the synthesis and manufacturing of the ECMs and ECWs, and their electrochemical and spectroscopical characterization, it is referred to the studies by Jelle [10], Jelle and Hagen [20-22] and Jelle et al. [23]. In short, the ECMs polyaniline (PANI), prussian blue (PB)

and tungsten oxide (WO_3) were deposited electrochemically onto transparent conducting glass plates coated with indium-tin-oxide (ITO), i.e. indium oxide doped with tin ($In_2O_3(Sn)$), whereas solid state ECWs were then constructed by applying the solid state polymer electrolyte poly(2-acrylamido-2-methyl-propane-sulphonic acid) (PAMPS) as an ionic conductor, see Fig.1 for a schematic drawing of the two ECWs presented here (denoted as ECW1 and ECW3).

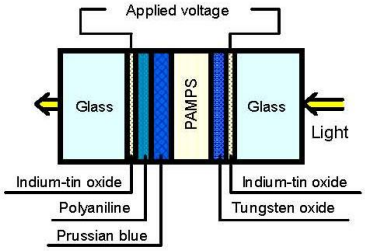

Figure 1. Schematic drawing of the ECW configuration used for ECW1 and ECW3 based on the ECMs polyaniline (PANI), prussian blue (PB) and tungsten oxide (WO_3).

Furthermore, for the spectroscopical measurements, a Cary 5 UV-VIS-NIR spectrophotometer, with an absolute reflectance accessory (Strong-type, VW principle), was used to measure the transmittance and reflectance of the ECWs, whereas emissivity measurements were performed with a SOC-100 HDR Hemispherical Directional Reflectometer from Surface Optics Corporation connected to a Thermo Nicolet 8700 Fourier transform infrared (FTIR) Spectrometer.

Results and Discussion

Measured transmittance spectra for two different ECWs at various applied electrical potentials (voltages) are given in Fig.2, with corresponding calculated solar radiation glazing factors and factor modulations in Table 1 and Table 2, respectively.

As to show an example how to calculate the solar radiation glazing factors, the solar transmittance (T_{sol}) is given by the following expression [9]:

$$T_{sol} = \frac{\sum_{\lambda=300nm}^{2500nm} T(\lambda) S_\lambda \Delta\lambda}{\sum_{\lambda=300nm}^{2500nm} S_\lambda \Delta\lambda} \quad (1)$$

where S_λ is the relative spectral distribution of solar radiation, $T(\lambda)$ is the spectral transmittance of the glass, λ is the wavelength, $\Delta\lambda$ is the wavelength interval, and the $S_\lambda\Delta\lambda$ values at different wavelengths are given as tabulated values [10,18]. The T_{sol} value will thus be a number between 0 and 1 (or 0 and 100 %), calculated in the main part of the solar spectrum, i.e. 300-2500 nm. A low number indicates a low transmission of solar radiation, whereas a high number represents a high solar radiation transmission. Note that the whole solar spectrum is not covered in the (standard) calculation of T_{sol}, and in future versions the wavelength range may favourably be extended to cover an even larger part of the solar radiation, e.g. from 290 nm to 3000 nm. In similar ways the other solar radiation glazing factors may be calculated, except the ε, SF and CRF values which follow other calculation procedures [10,18]. The ECW modulation level given in Table 2 is calculated by subtracting the solar radiation glazing factors for the same ECW at the high and low potentials given in Table 1, e.g. as for ΔT_{sol}:

$$\Delta T_{sol} = T_{sol}(\text{bleached}) - T_{sol}(\text{coloured}) \quad (2)$$

where the T_{sol} values in Table 1 are calculated from Eq.1 and likewise for the other solar radiation glazing factors.

From Table 1 it is observed that various solar radiation glazing factors may obtain both high and low values depending upon the applied electrical potential in the ECWs, e.g. changing the T_{vis} value from 0.78 to 0.17 for the ECW1 device and from 0.69 to 0.09 for the darker ECW3 device. It is also noted that these ECWs contain solar radiation absorbing electrochromic materials, i.e. not reflecting materials, as the changes with applied potential occur in the transmittance (e.g. T_{sol}) and absorbance (e.g. A_{sol}) values, and not in the reflectance (e.g. R_{sol}) values. As expected, the highest colouration level gives the largest SMPF values, i.e. the best protection of materials is achieved with the darkest ECW, e.g.

compare a SMPF value of 0.71 for ECW1 and 0.83 for ECW3 in the coloured state, with 0.43 (ECW1) and 0.59 (ECW3) in the transparent (bleached) state, respectively. The CRF values are very high, i.e. a very good colour rendering, for both ECW configurations in the transparent (bleached) state, with CRF values ranging from 0.96 to 0.99. However, in the coloured state, the CRF values are substantially reduced for both ECWs. ECW1 has CRF = 0.68 and ECW3 has CRF = 0.59 in the coloured state.

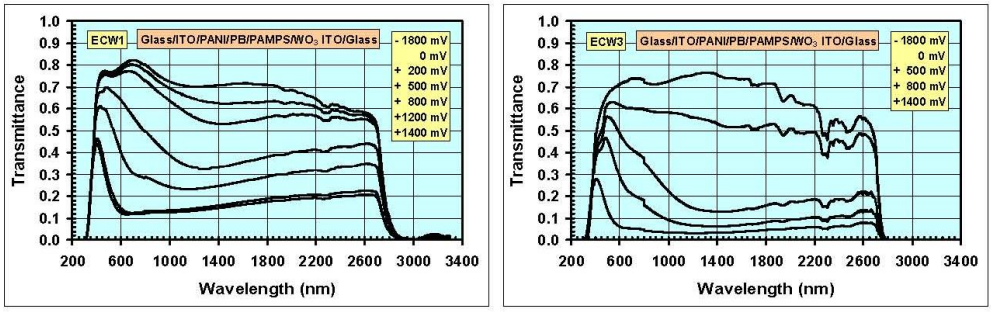

Figure 2. Transmittance versus wavelength in the whole solar spectrum measured for two different ECWs at various applied potentials [10,21,23]. Highest colouration level is at +1400 mV.

Table 1. Calculated solar radiation glazing factors for two different ECWs at various colouration levels (with transparent and dark coloured as the extremes), i.e. at various applied potentials (e.g. Eq.1). Corresponding transmittance spectra are given in Figure 2.

Glass Configuration	n	T_{uv}	T_{vis}	T_{sol}	SMPF	SSPF	$R_{vis,ext}$	$R_{vis,int}$	R_{sol}	A_{sol}	ε	SF	CRF
ECW1 (-1800 mV)	1	0.23	0.78	0.74	0.43	0.93	0.09	0.09	0.08	0.18	0.836	0.79	0.98
ECW1 (0 mV)	1	0.23	0.77	0.72	0.43	0.93	0.09	0.09	0.08	0.21	0.836	0.77	0.98
ECW1 (+200 mV)	1	0.24	0.75	0.68	0.44	0.93	0.09	0.09	0.08	0.24	0.836	0.74	0.99
ECW1 (+500 mV)	1	0.25	0.66	0.52	0.48	0.93	0.09	0.09	0.08	0.40	0.836	0.62	0.95
ECW1 (+800 mV)	1	0.26	0.47	0.36	0.54	0.92	0.09	0.09	0.08	0.56	0.836	0.51	0.82
ECW1 (+1200 mV)	1	0.24	0.19	0.19	0.68	0.93	0.09	0.09	0.08	0.73	0.836	0.38	0.68
ECW1 (+1400 mV)	1	0.23	0.17	0.17	0.71	0.93	0.09	0.09	0.08	0.75	0.836	0.37	0.68
ECW3 (-1800 mV)	1	0.08	0.69	0.67	0.59	0.97	0.09	0.09	0.08	0.25	0.836	0.74	0.96
ECW3 (+1400 mV)	1	0.12	0.09	0.08	0.83	0.97	0.09	0.09	0.08	0.84	0.836	0.30	0.59

Table 2. Calculated solar radiation glazing factor modulations for two different ECWs. The modulation level is calculated by subtracting the solar radiation glazing factors for the same ECW at the high and low potentials given in Table 1 (e.g. Eq.2).

Glass Configuration	n	ΔT_{uv}	ΔT_{vis}	ΔT_{sol}	ΔSMPF	ΔSSPF	$\Delta R_{vis,ext}$	$\Delta R_{vis,int}$	ΔR_{sol}	ΔA_{sol}	ε	ΔSF	ΔCRF
ECW1 (-1800 mV) ECW1 (+1400 mV)	1	0.00	0.61	0.57	-0.28	0.00	0.00	0.00	0.00	-0.57	-	0.42	0.30
ECW3 (-1800 mV) ECW3 (+1400 mV)	1	-0.04	0.60	0.59	-0.24	0.00	0.00	0.00	0.00	-0.59	-	0.44	0.37

The ECW1 and ECW3 devices have rather large solar radiation modulation abilities, e.g. ΔT_{vis} = 0.61 and ΔT_{sol} = 0.57 for ECW1, and ΔT_{vis} = 0.60 and ΔT_{sol} = 0.59 for ECW3, where the transmittance modulation is assumed to be due to absorbance regulation, i.e. ΔA_{sol} = -0.57 for ECW1 and ΔA_{sol} = -0.59 for ECW3. Note that reflectance values of the ECWs have not been measured, but as the (absorbing) electrochromic coatings are located between two glass plates, the (low) reflectance values will be close to the values for float glass, and these are hence employed in the current calculations. Although the solar factor modulations are lower than their solar transmission counterparts for the ECWs, the solar factor modulations are still quite high, i.e. ΔSF = 0.42 for ECW1 and ΔSF = 0.44 for ECW3. Thus, these ECWs are able to regulate large parts of the solar radiation, and their regulation may be readily characterized by the solar radiation glazing factors. Applying the ECWs into two-layer and three-layer window pane configurations reduces the total solar energy throughput modulation in the windows, which may also be seen in the ΔT_{sol} and ΔSF values, as several layers of glass and coatings will increase the total reflectance and absorbance (not depicted here, for examples it is referred to the work by Jelle [10]), i.e. less solar radiation left for the ECWs to modulate (regulate). That is, the solar radiation

modulation by an ECW will decrease with the number of glass panes and low emittance coatings added to the total window configuration.

Conclusions

Electrochromic windows (ECW) may dynamically control daylight and solar energy in buildings. This control may be readily characterized by solar radiation glazing factors, i.e. ultraviolet solar transmittance (T_{uv}), visible solar transmittance (T_{vis}), solar transmittance (T_{sol}), solar material protection factor (SMPF), solar skin protection factor (SSPF), external visible solar reflectance ($R_{vis,ext}$), internal visible solar reflectance ($R_{vis,int}$), solar reflectance (R_{sol}), solar absorbance (A_{sol}), emissivity (ε), solar factor (SF) and colour rendering factor (CRF). Two ECWs have been presented, demonstrating a large solar radiation modulation.

Acknowledgements

This work has been supported by the Research Council of Norway and several partners through "*The Research Centre on Zero Emission Buildings*" (ZEB).

References

1. B.P. Jelle, G. Hagen and S. Nødland, "Transmission spectra of an electrochromic window consisting of polyaniline, prussian blue and tungsten oxide", *Electrochimica Acta*, **38**, 1497-1500, 1993.
2. B.P. Jelle, G. Hagen, S.M. Hesjevik and R. Ødegård, "Reduction factor for polyaniline films on ITO from cyclic voltammetry and visible absorption spectra", *Electrochimica Acta*, **38**, 1643-1647, 1993.
3. C.G. Granqvist, "Handbook of inorganic electrochromic materials", Elsevier, Amsterdam, 1995.
4. P.M.S. Monk, R.J. Mortimer and D.R. Rosseinsky, "Electrochromism: Fundamentals and applications", VCH, 1995.
5. B.P. Jelle and G. Hagen, "Electrochemical multilayer deposition of polyaniline and prussian blue and their application in solid state electrochromic windows", *Journal of Applied Electrochemistry*, **28**, 1061-1065, 1998.
6. B.P. Jelle and G. Hagen, "Correlation between light absorption and electric charge in solid state electrochromic windows", *Journal of Applied Electrochemistry*, **29**, 1103-1110, 1999.
7. R.J. Mortimer, "Organic electrochromic materials", *Electrochimica Acta*, **44**, 2971-2981, 1999.
8. R. Baetens, B.P. Jelle and A. Gustavsen, "Properties, requirements and possibilities of smart windows for dynamic daylight and solar energy control in buildings: A state-of-the-art review", *Solar Energy Materials and Solar Cells*, **94**, 87-105, 2010.
9. B.P. Jelle, A. Hynd, A. Gustavsen, D. Arasteh, H. Goudey and R. Hart, "Fenestration of today and tomorrow: A state-of-the-art review and future research opportunities", *Solar Energy Materials and Solar Cells*, **96**, 1-28, 2012.
10. B.P. Jelle, "Solar radiation glazing factors for window panes, glass structures and electrochromic windows in buildings - Measurement and calculation", *Solar Energy Materials and Solar Cells*, **116**, 291-323, 2013.
11. S.K. Deb, S.-H. Lee, C.E. Tracy, J.R. Pitts, B.A. Gregg and H.M. Branz, "Stand-alone photovoltaic-powered electrochromic smart window", *Electrochimica Acta*, **46**, 2125-2130, 2001.
12. C.M. Lampert, "Large-area smart glass and integrated photovoltaics", *Solar Energy Materials and Solar Cells*, **76**, 489-499, 2003.
13. B.P. Jelle, C. Breivik and H.D. Røkenes, "Building integrated photovoltaic products: A state-of-the-art review and future research opportunities", *Solar Energy Materials and Solar Cells*, **100**, 69-96, 2012.
14. K. Midtdal and B.P. Jelle, "Self-cleaning glazing products: A state-of-the-art review and future research pathways", *Solar Energy Materials and Solar Cells*, **109**, 126-141, 2013.
15. B.P. Jelle, "The challenge of removing snow downfall on photovoltaic solar cell roofs in order to maximize solar energy efficiency - Research opportunities for the future", *Energy and Buildings*, **67**, 334-351, 2013.
16. B.P. Jelle, "Accelerated climate ageing of building materials, components and structures in the laboratory", *Journal of Materials Science*, **47**, 6475-6496, 2012.
17. B.P. Jelle, E. Sveipe, E. Wegger, A. Gustavsen, S. Grynning, J.V. Thue, B. Time and K.R. Lisø, "Robustness classification of materials, assemblies and buildings", *Journal of Building Physics*, **37**, 213-245, 2014.
18. ISO 9050:2003(E), "Glass in building - Determination of light transmittance, solar direct transmittance, total solar energy transmittance, ultraviolet transmittance and related glazing factors", 2003.
19. B.P. Jelle, A. Gustavsen, T.-N. Nilsen and T. Jacobsen, "Solar material protection factor (SMPF) and solar skin protection factor (SSPF) for window panes and other glass structures in buildings", *Solar Energy Materials and Solar Cells*, **91**, 342-354, 2007.
20. B.P. Jelle and G. Hagen, "Transmission spectra of an electrochromic window based on polyaniline, prussian blue and tungsten oxide", *Journal of Electrochemical Society*, **140**, 3560-3564, 1993.
21. B.P. Jelle and G. Hagen, "Solar modulation in an electrochromic window using polyaniline, prussian blue and tungsten oxide", in *Electrochromic Materials II*, (PV 94-2), K. C. Ho and D. A. MacArthur (eds.), pp. 324-338, *Proceedings of the Symposium on Electrochromic Materials, The 184th Meeting of The Electrochemical Society*, New Orleans, Louisiana, U.S.A., 10-15 October, 1993, The Electrochemical Society, Pennington, NJ, 1994.
22. B.P. Jelle and G. Hagen, "Performance of an electrochromic window based on polyaniline, prussian blue and tungsten oxide", *Solar Energy Materials and Solar Cells*, **58**, 277-286, 1999.
23. B.P. Jelle, G. Hagen and Ø. Birketveit, "Transmission properties for individual electrochromic layers in solid state devices based on polyaniline, prussian blue and tungsten oxide", *Journal of Applied Electrochemistry*, **28**, 483-489, 1998.

Paper 5

Measurements of Ionic Liquids Thermal Conductivity and Thermal Diffusivity

Journal of Thermal Analysis and Calorimetry 2017, 128, 279–288.

J Therm Anal Calorim (2017) 128:279–288
DOI 10.1007/s10973-016-5881-0

Measurements of ionic liquids thermal conductivity and thermal diffusivity

Yansong Zhao[1] · Yingpeng Zhen[2] · Bjørn Petter Jelle[2,3] · Tobias Boström[1]

Received: 28 January 2016 / Accepted: 1 October 2016 / Published online: 2 November 2016

Abstract Thermal conductivity and thermal diffusivity of ionic liquids (ILs) are investigated in this work. A hot disk method for ILs thermal conductivity and thermal diffusivity measurement is utilized. Firstly, the thermal conductivity of water is measured to check the reliability of the hot disk method. In addition, the thermal conductivity of pure ILs, including $BmimBF_4$, $BmimPF_6$, OmimCl, $BmimFeCl_4$, and $OmimFeCl_4$, is measured. By comparison with thermal conductivity values of water, $BmimBF_4$, and $BmimPF_6$ in the literatures, it is found that the thermal conductivity values of ILs using hot disk method have high reliability. Therefore, the hot disk method is utilized for thermal conductivity measurement of ILs in this work. The experimental results also show that all the average thermal conductivity values of the five pure ILs are no more than 0.1898 $W\,m^{-1}\,K^{-1}$, which is much lower than the average measured thermal conductivity of water, namely 0.6033 $W\ m^{-1}\ K^{-1}$. Effect of nanoparticles (NPs) on thermal conductivity of ILs is also investigated. It is shown that the thermal conductivity of $BmimBF_4$ does not change significantly in the presence of Fe_2O_3 NPs. However, the thermal conductivity of $BmimPF_6$ decreases somewhat in the presence of R711 NPs. In addition, the thermal diffusivity of pure ILs, including $BmimBF_4$, $BmimPF_6$, $BmimFeCl_4$, OmimCl, and $OmimFeCl_4$, is measured. All the average thermal diffusivity values of the ILs of $BmimBF_4$, $BmimPF_6$, $BmimFeCl_4$, OmimCl, and $OmimFeCl_4$ are no more than 0.1185 $mm^2\ s^{-1}$. The thermal diffusivity of water is 0.143 $mm^2\ s^{-1}$ in the literature. It illustrates that the ILs also have a better thermal property than water for energy storage. ILs may be utilized as novel materials for energy storage. Effect of NPs on thermal diffusivity of ILs is also investigated. The results are similar to how NPs influence thermal conductivity of $BmimBF_4$ and $BmimPF_6$. In the presence of Fe_2O_3 NPs, thermal diffusivity of $BmimBF_4$ does not change significantly. However, in the presence of R711 NPs, thermal diffusivity of $BmimPF_6$ decreases somewhat.

Keywords Ionic liquid · Nanoparticle · Thermal conductivity · Thermal diffusivity · Thermal property · Hot disk

Introduction

Ionic liquids (ILs) are environmentally friendly materials. ILs have many excellent properties, which currently are hot research topics. Due to the excellent properties, ILs have been utilized as novel and promising materials in many research fields. For example, ILs can be utilized in energy conversion and energy storage, including solar cells [1–7], batteries [8–16], and supercapacitors [17–28].

Thermal properties of ILs are important [29–31]. Thermal conductivity is the ability of a material to conduct heat, which is an important parameter for utilization of ILs [32–34]. Thermal conductivity and thermal diffusivity are crucial for application of ILs in real energy conversion and energy storage processes. However, there is scant literature

✉ Yansong Zhao
yansong.zhao2004@gmail.com; yansong.zhao@uit.no

[1] Energy and Climate Group, Department of Physics and Technology, UiT The Arctic University of Norway, 9037 Tromsø, Norway

[2] Department of Civil and Transport Engineering, Norwegian University of Science and Technology (NTNU), 7491 Trondheim, Norway

[3] Department of Materials and Structures, SINTEF Building and Infrastructure, 7465 Trondheim, Norway

that can be found for thermal conductivity measurement of ILs. Frez et al. [35] utilized the transient grating method for the thermal conductivity measurement of 7 ILs. In the work of Ge et al., the transient hot-wire method was utilized to measure the thermal conductivity of 11 pure ILs [36]. Fröba et al. [37] measured the thermal conductivity of ILs using parallel plate method. The thermal conductivity data of ILs are limited in the current literatures. Therefore, the thermal conductivity of ILs is measured using a hot disk method in this work. In addition, the effect of nanoparticles (NPs) on the thermal conductivity of ILs is investigated.

Thermal diffusivity is the ability of a material to conduct thermal energy relative to its ability to store thermal energy [38]. The definition of thermal diffusivity α is as follows:

$$\alpha = \frac{\kappa}{\rho c_p} \tag{1}$$

where α, κ, ρ, and c_p are thermal diffusivity, thermal conductivity, mass density, and specific heat capacity, respectively. Thermal diffusivity is also an important parameter for utilization of ILs. However, the thermal diffusivity measurement of ILs is extremely scant. Frez et al. [35] are the only researchers who experimentally measured the thermal diffusivity of pure ILs according to our own knowledge. In the work of Frez et al. [35], transient grating technique was utilized for measurement of pure ILs thermal diffusivity. We found the thermal diffusivity data of ILs are rarely known in the current literatures. Therefore, in this work the thermal diffusivity of ILs is measured using hot disk method. In addition, the effect of NPs on thermal diffusivity of ILs is investigated.

Theory

The theory of hot disk method is introduced in this part based on the Introduction Manual of Hot Disk Thermal Constants Analyser [39]. The hot disk is electrically heated for the thermal conductivity and thermal diffusivity measurement. The resistance increase can be described as a function of time as follows:

$$R(t) = R_0\{1 + \beta[\Delta T_i + \Delta T_a(\tau)]\} \tag{2}$$

where $R(t)$ is disk resistance at time t, R_0 is disk resistance at time $t = 0$, β is temperature coefficient of resistivity, ΔT_i is the constant temperature difference, and $\Delta T_a(\tau)$ is time dependent temperature increase [39]. The time dependent temperature increase can be obtained by the theory as follows:

$$\Delta T_a(\tau) = \frac{P_0}{\pi^{3/2} \cdot a \cdot \kappa} \cdot D(\tau) \tag{3}$$

where P_0 is the total power output of the sensor, a is the overall radius of the disk, κ is the testing thermal conductivity of the sample, and $D(\tau)$ is a dimensionless time dependent function, [39] where τ is given by the following:

$$\tau = \sqrt{\frac{t}{\Theta}} \tag{4}$$

where t is the time measured from the start of the transient recording, and Θ is the characteristic time which can be defined as follows [39]:

$$\Theta = \frac{\alpha^2}{\kappa} \tag{5}$$

During the experiment process, the experimental curve of temperature increase versus elapsed time can be obtained. Subsequently, the curve of temperature increase versus $D(\tau)$ can be obtained by calculation. Then, the curve of temperature increase versus $D(\tau)$ can be fitted using a linear line. The slope of the linear fitting line can be obtained. As is shown in Eq. 3, the slope of the linear fitting line is $\frac{P_0}{\pi^{3/2} \cdot a \cdot \kappa}$. As known, in the experiments of this work, the total power P_0 is 0.02 W, and the overall radius of the disk a is 3.189 mm. Therefore, the thermal conductivity κ can be calculated [39]. In addition, the value of thermal diffusivity can be calculated based on Eqs. 3–5.

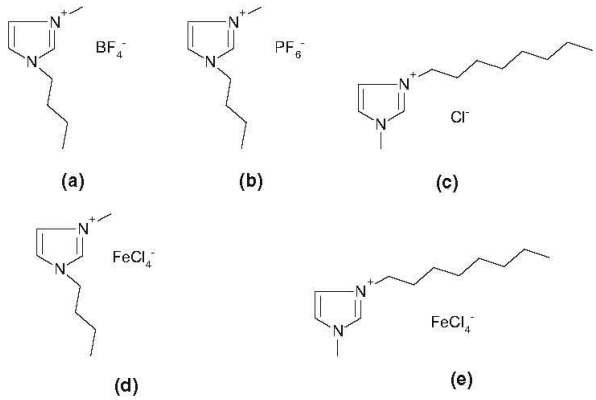

Scheme 1 Structure of $BmimBF_4$ (**a**), $BmimPF_6$ (**b**), OmimCl (**c**), $BmimFeCl_4$ (**d**), and $OmimFeCl_4$ (**e**)

Experimental

Materials

ILs of 1-butyl-3-methylimidazolium tetrafluoroborate (CAS R.N. 174501-65-6, $BmimBF_4$), 1-butyl-3-methylimidazolium hexafluorophosphate (CAS R.N. 174501-64-5, $BmimPF_6$), and 1-methyl-3-octylimidazolium chloride (CAS R.N. 64697-40-1, OmimCl) are obtained from Sigma-Aldrich. The mass fractions purity of the three ILs are ≥97 %. Fe_2O_3 nanoparticles (NPs) (Average size: <50 nm) are also purchased from Sigma-Aldrich and utilized in this work. R711 NPs are received from Evonik Industries AG, Germany. ILs of $BmimFeCl_4$ and $OmimFeCl_4$ are synthesized in our laboratory and utilized in this work. The synthesis procedure of $BmimFeCl_4$ can be found from our previous work [40]. The chemical structures of the ILs utilized in this work are shown in Scheme 1. Samples of $BmimPF_6$ + R711 NPs and $BmimBF_4$ + Fe_2O_3 NPs are also prepared in this work. The two samples are treated using ultrasound instrument at 30 °C for at least 30 min before the measurement. The ultrasound can enhance the NPs dispersed in the ILs. It is found the dispersed ability of R711 NPs in $BmimPF_6$ is excellent. However, the dispersed ability of Fe_2O_3 NPs is not as good as the former one. The Fe_2O_3 NPs can be precipitated from the bulk $BmimBF_4$ after a long time quiescent process.

Thermal conductivity measurements

Thermal conductivity of ILs is measured using hot disk method. The experimental procedure is given as follows. The hot disk instrument should be turned on at least 1 h before the thermal conductivity measurement experiments

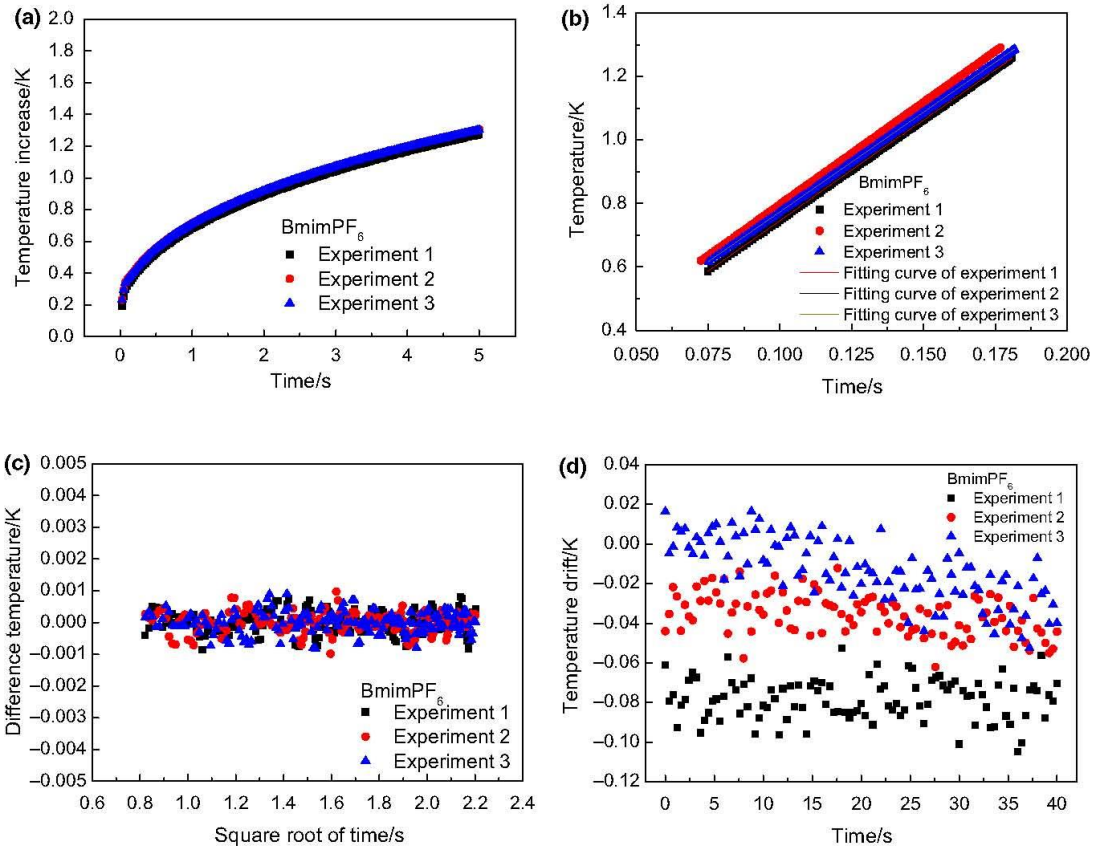

Fig. 1 Thermal conductivity and thermal diffusivity measurement of $BmimPF_6$. **a** Temperature increase versus time, **b** temperature increase versus $D(\tau)$ (the *slopes* of the fitting curves of experiments 1, 2, and 3 are 6.3337, 6.4415, and 6.2822, respectively. The R^2 of all the fitting curves of experiments 1, 2, and 3 are 1), **c** difference temperature versus square root of time, **d** temperature drift versus time

are performed. A sample is added into a beaker. Subsequently, the sensor is put into the sample. There should be sample material at least 25 mm around the senor. The total power and measurement time for the given experiments are 0.02 W and 5 s, respectively. The experimental data of the temperature increase versus elapsed time are recorded during the process. Finally, the thermal conductivity of the sample can be calculated based on Eqs. 3–5.

Thermal diffusivity measurements

Thermal diffusivity of ILs is also measured using hot disk method. The thermal diffusivity measurement procedure is the same as the experimental procedure for thermal conductivity measurement. The thermal diffusivity can be calculated based on the experimental data and Eqs. 3–5. Hot disk method is a new method for ILs thermal diffusivity measurement.

Results and discussions

Thermal conductivity and thermal diffusivity measurements of ILs using hot disk method

The thermal conductivity and thermal diffusivity measurement process using the hot disk method is shown as follows. In order to demonstrate the procedure, the method on determination of the thermal conductivity and thermal diffusivity of $BmimBF_6$ is shown as an example. The experiments for thermal conductivity and thermal diffusivity measurement of $BmimBF_6$ are repeated for three times. As shown in Fig. 1a, the experimental curve

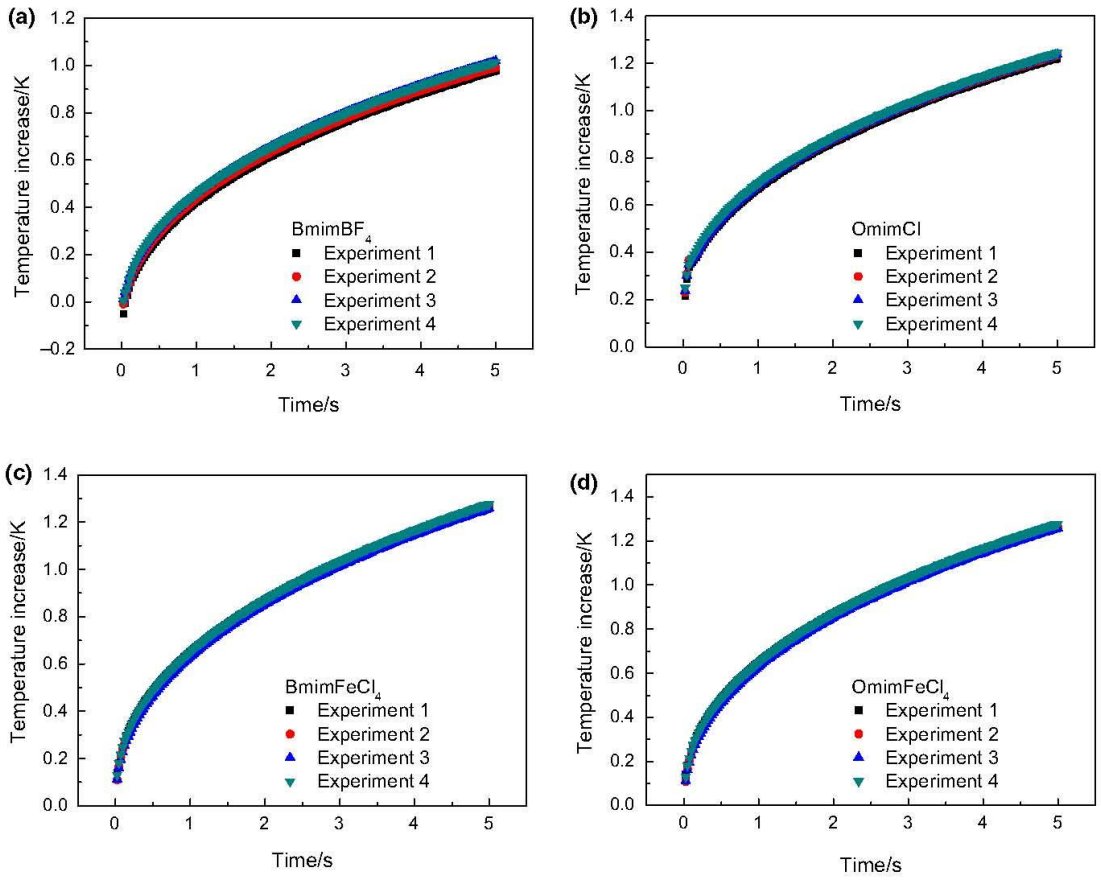

Fig. 2 Temperature increase versus time during the measurement process in $BmimBF_4$, OmimCl, $BmimFeCl_4$, and $OmimFeCl_4$

of temperature increase versus elapsed time can be obtained directly during the process. Subsequently, the curve of temperature increase versus $D(\tau)$ can be calculated and obtained, which is shown in Fig. 1b. In addition, the curve of temperature increase versus $D(\tau)$ can be fitted using a linear line. The linear line fitting results are also shown in Fig. 1b. The slope of the linear fitting line can be obtained. Based on Eqs. 3–5, the thermal conductivity and thermal diffusivity of $BmimPF_6$ can be calculated. Moreover, the experimental data of difference temperature versus square root of time are obtained and shown in Fig. 1c. Furthermore, the experimental data of temperature drift versus time can be obtained during the process and are shown for $BmimPF_6$ in Fig. 1d. This curve can be utilized to check the temperature drift during the process, which is important as to whether the experimental data are reliable or not.

Thermal conductivity measurements

Reliability of hot disk method

The thermal conductivity of water is measured using the hot disk method at 21 °C. The experimental results are shown in Table 1. The average measured thermal conductivity value of water is 0.6033 W m^{-1} K^{-1} at 21 °C in this work. The reference thermal conductivity value of water at 20 °C is 0.6 W m^{-1} K^{-1} [34]. In addition, the measured thermal conductivity values of pure ILs $BmimBF_4$ and $BmimPF_6$ are 0.1898 and 0.1733 W m^{-1} K^{-1} at 21 °C, respectively. The

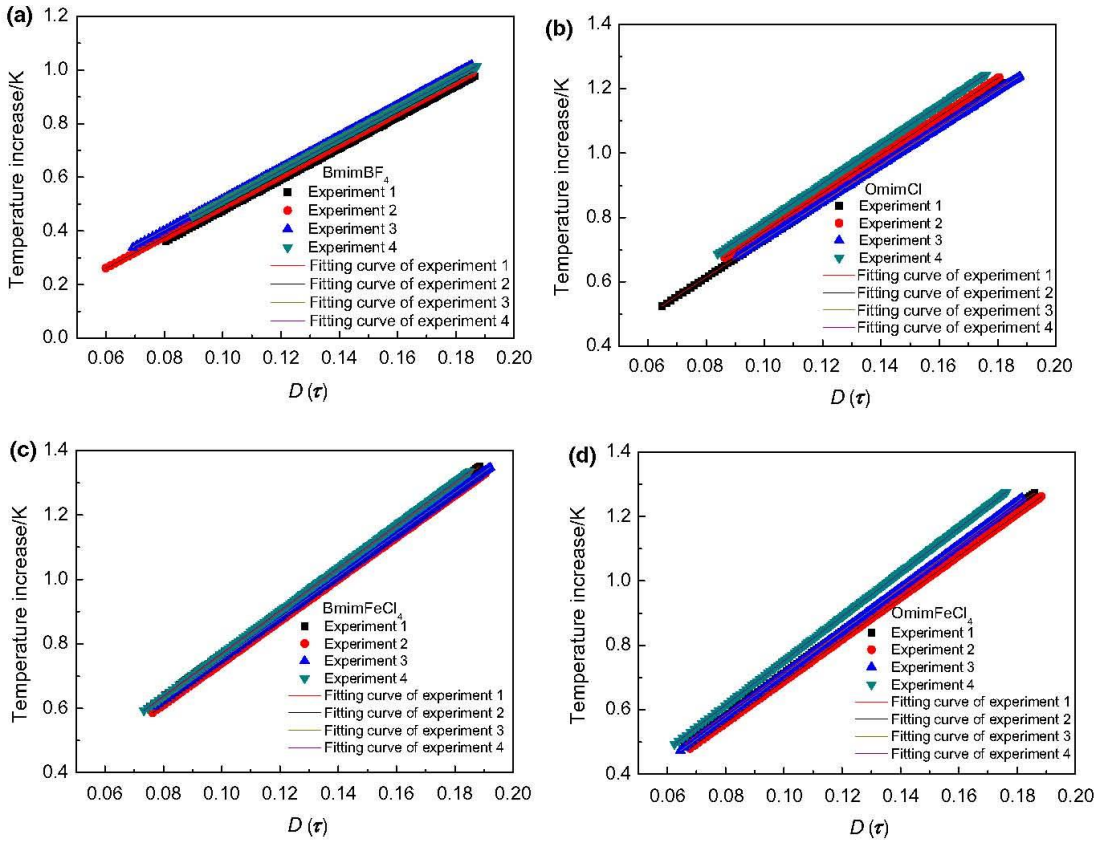

Fig. 3 Temperature increase versus $D(\tau)$ curves and the linear fitting lines of temperature increase versus $D(\tau)$ in $BmimBF_4$ (**a** the *slopes* of the fitting curves of experiments 1, 2, 3, and 4 are 5.8127, 5.8035, 5.8376, and 5.7915, respectively. The R^2 of all the fitting curves of experiments 1, 2, 3, and 4 are 1). OmimCl (**b** the *slopes* of the fitting curves of experiments 1, 2, 3, and 4 are 5.8625, 5.9399, 5.7662, and 6.0480, respectively. The R^2 of all the fitting curves of experiments 1, 2, 3, and 4 are 1), $BmimFeCl_4$ (**c** the *slopes* of the fitting curves of experiments 1, 2, 3, and 4 are 6.5846, 6.5063, 6.4654, and 6.6489, respectively. The R^2 of all the fitting curves of experiments 1, 2, 3, and 4 are 1) and $OmimFeCl_4$ (**d** the *slopes* of the fitting curves of experiments 1, 2, 3, and 4 are 6.4980, 6.4942, 6.6907, and 6.8855, respectively. The R^2 of all the fitting curves of experiments 1, 2, 3, and 4 are 1)

reference values of thermal conductivity of $BmimBF_4$ and $BmimPF_6$ are 0.186 and 0.145 W m^{-1} K^{-1} at 25 °C, respectively [41]. The measurement results are in good agreements with the reference values. Therefore, the hot disk method is utilized to measure the thermal conductivity of ILs based materials in this work.

Pure ILs thermal conductivity measurements

Thermal conductivity of pure ILs, including $BmimBF_4$, $BmimPF_6$, OmimCl, $BmimFeCl_4$, and $OmimFeCl_4$, is measured at 21 °C. The curve of temperature increase versus elapsed time of $BmimPF_6$ is shown in Fig. 1a. The curves of temperature increase versus time of the other 4 ILs are shown in Fig. 2. Based on the temperature increase versus time curves, the temperature increase versus $D(\tau)$ curves of the ILs can be obtained, which are shown in Figs. 1b and 3. Subsequently, based on Eqs. 3–5, the thermal conductivity of ILs can be calculated. The results are shown in Table 2. It is found that the measurement thermal conductivity values of the five pure ILs are no more than 0.1898 W m^{-1} K^{-1}. However, the measurement thermal conductivity value of water is 0.6033 W m^{-1} K^{-1}. The thermal conductivity of the five pure ILs is thus much lower than that of water.

Table 1 Thermal conductivity of water at 21 °C

Water	Experiment number	Test value/ W m $^{-1}$ K $^{-1}$	Average value/ W m $^{-1}$ K $^{-1}$
	1	0.6080	
	2	0.6022	
	3	0.6147	
	4	0.6010	
	5	0.5906	
			0.6033

Table 2 Thermal conductivity of $BmimBF_4$, $BmimPF_6$, OmimCl, $BmimFeCl_4$, and $OmimFeCl_4$ at 21 °C

Sample	Experiment number	Test value/ W m $^{-1}$ K $^{-1}$	Average value/ W m $^{-1}$ K $^{-1}$
$BmimBF_4$	1	0.1900	
	2	0.1891	
	3	0.1890	
	4	0.1909	
			0.1898
$BmimPF_6$	1	0.1738	
	2	0.1709	
	3	0.1753	
			0.1733
OmimCl	1	0.1881	
	2	0.1862	
	3	0.1918	
	4	0.1829	
			0.1873
$BmimFeCl_4$	1	0.1671	
	2	0.1692	
	3	0.1703	
	4	0.1655	
			0.1680
$OmimFeCl_4$	1	0.1692	
	2	0.1692	
	3	0.1642	
	4	0.1596	
			0.1656

Effect of NPs on thermal conductivity of ILs

The effect of NPs on thermal conductivity of ILs is investigated. The two samples of $BmimBF_4$ + Fe_2O_3 NPs

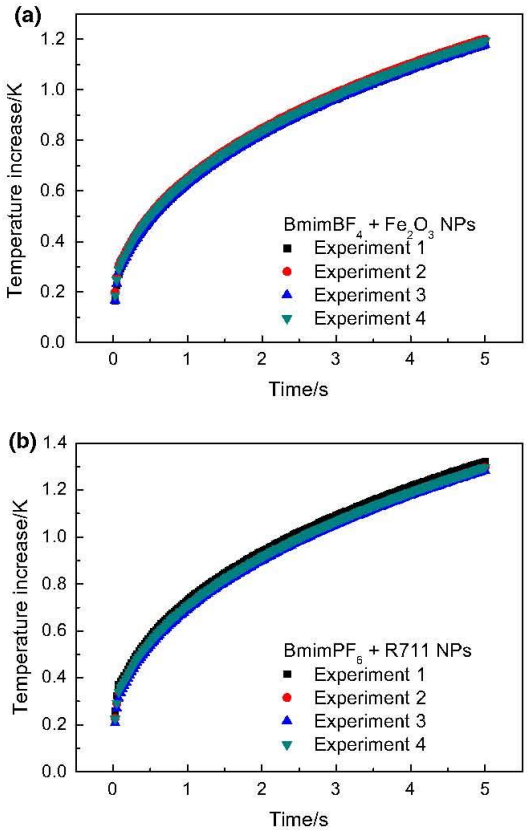

Fig. 4 Temperature increase versus time during the measurement process in $BmimBF_4$ + Fe_2O_3 NPs and $BmimPF_6$ + R711 NPs samples

and $BmimPF_6$ + R711 NPs are utilized. The curves of temperature increase versus elapsed time are obtained and shown in Fig. 4. The curves of temperature increase versus $D(\tau)$ are obtained and shown in Fig. 5. Subsequently, the thermal conductivity values of the samples can be calculated. The results are shown in Table 3. As shown in Table 2, the thermal conductivity of $BmimBF_4$ is 0.1898 W m^{-1} K^{-1} at 21 °C. As shown in Table 3, the thermal conductivity of the $BmimBF_4$ + Fe_2O_3 NPs sample becomes 0.1895 W m^{-1} K^{-1} at 21 °C. Hence, it is shown that the thermal conductivity of $BmimBF_4$ does not change significantly in the presence of Fe_2O_3 NPs.

However, as shown in Table 2, the thermal conductivity of $BmimPF_6$ is 0.1733 W m^{-1} K^{-1} at 21 °C. As shown in Table 3, the thermal conductivity of the $BmimPF_6$ + R711 NPs sample becomes 0.1670 W m^{-1} K^{-1} at 21 °C. Hence, it illustrates that the thermal conductivity of $BmimPF_6$ decreases about 3.6 % in the presence of R711 NPs.

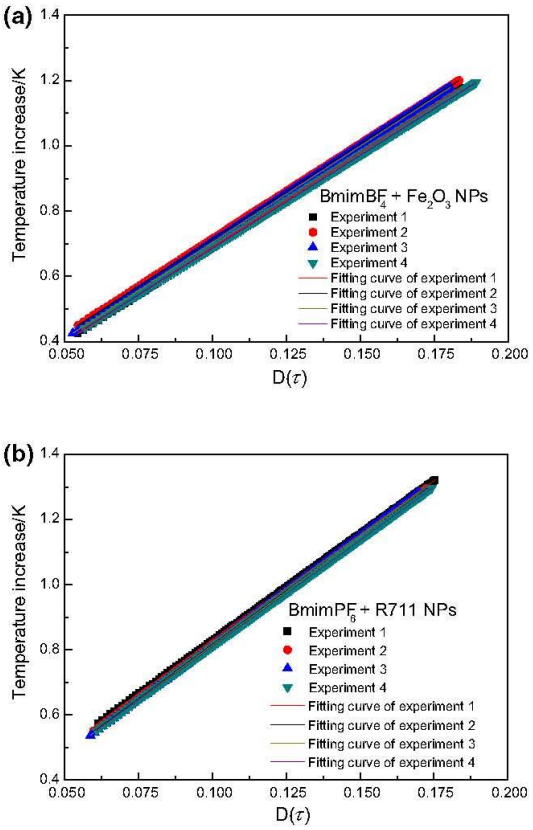

Fig. 5 Temperature increase versus $D(\tau)$ curves and the linear fitting lines of temperature increase versus $D(\tau)$ in the sample of $BmimBF_4$ + Fe_2O_3 NPs (**a** the *slopes* of the fitting curves of experiments 1, 2, 3, and 4 are 5.8176, 5.8230, 5.9036, and 5.6990, respectively. The R^2 of all the fitting curves of experiments 1, 2, 3, and 4 are 1) and $BmimPF_6$ + R711 NPs (**b** the slopes of the fitting curves of experiments 1, 2, 3, and 4 are 6.5338, 6.5939, 6.6943, and 6.5609, respectively. The R^2 of all the fitting curves of experiments 1, 2, 3, and 4 are 1)

Thermal diffusivity measurements

Pure ILs thermal diffusivity measurements

Thermal diffusivity of pure ILs, including $BmimBF_4$, $BmimPF_6$, $BmimFeCl_4$, OmimCl, and $OmimFeCl_4$, is measured. The results are shown in Table 4. The thermal diffusivity values of the ILs are no more than 0.1185 mm^2 s^{-1}. This value is less than the thermal diffusivity of water 0.143 mm^2 s^{-1} [42]. It illustrates that the ILs also have a better property than water for energy storage. Therefore, ILs may be considered as a type of novel materials for energy storage.

Effect of NPs on thermal diffusivity of ILs

The effect of NPs on thermal diffusivity of ILs is investigated. The results are shown in Table 5. Similar to the effect of NPs on thermal conductivity, the samples of $BmimBF_4$ + Fe_2O_3 NPs and $BmimPF_6$ + R711 NPs are utilized. As shown in Table 4, the thermal diffusivity of $BmimBF_4$ is 0.1140 mm^2 s^{-1} at 21 °C. As shown in Table 5, the thermal diffusivity of the $BmimBF_4$ + Fe_2O_3 NPs sample becomes 0.1116 mm^2 s^{-1} at 21 °C. Hence, it is shown that the thermal diffusivity of $BmimBF_4$ does not change significantly in the presence of Fe_2O_3 NPs.

For $BmimPF_6$, as shown in Table 4, the thermal diffusivity is 0.1082 mm^2 s^{-1} at 21 °C. As shown in Table 5,

Table 3 Thermal conductivity of samples of $BmimBF_4$ + Fe_2O_3 NPs and $BmimPF_6$ + R711 NPs at 21 °C

Sample	Experiment number	Test value/ W m^{-1} K^{-1}	Average value/ W m^{-1} K^{-1}
$BmimBF_4$ + Fe_2O_3 NPs	1	0.1892	
	2	0.1890	
	3	0.1864	
	4	0.1934	
			0.1895
$BmimPF_6$ + R711 NPs	1	0.1685	
	2	0.1670	
	3	0.1645	
	4	0.1678	
			0.1670

the thermal conductivity of the $BmimPF_6$ + R711 NPs sample becomes 0.09673 $mm^2 s^{-1}$ at 21 °C. Hence, the thermal diffusivity of $BmimPF_6$ decreases about 10.6 % in the presence of R711 NPs.

Table 4 Thermal diffusivity of $BmimBF_4$, $BmimPF_6$, OmimCl, $BmimFeCl_4$, and $OmimFeCl_4$ at 21 °C

Sample	Experiment number	Test value/ $mm^2 s^{-1}$	Average value/ $mm^2 s^{-1}$
$BmimBF_4$	1	0.1142	
	2	0.1141	
	3	0.1126	
	4	0.1151	
			0.1140
$BmimPF_6$	1	0.1096	
	2	0.1041	
	3	0.1109	
			0.1082
OmimCl	1	0.1105	
	2	0.1055	
	3	0.1149	
	4	0.1000	
			0.1077
$BmimFeCl_4$	1	0.1174	
	2	0.1208	
	3	0.1229	
	4	0.1129	
			0.1185
$OmimFeCl_4$	1	0.1140	
	2	0.1177	
	3	0.1085	
	4	0.1017	
			0.1105

Table 5 Thermal diffusivity of samples of $BmimBF_4$ + Fe_2O_3 NPs and $BmimPF_6$ + R711 NPs at 21 °C

Sample	Experiment number	Test value/ $mm^2 s^{-1}$	Average value/ $mm^2 s^{-1}$
$BmimBF_4$ + Fe_2O_3 NPs	1	0.1111	
	2	0.1106	
	3	0.1062	
	4	0.1183	
			0.1116
$BmimPF_6$ + R711 NPs	1	0.09929	
	2	0.09635	
	3	0.09298	
	4	0.09829	
			0.09673

Conclusions

ILs represent a hot research topic and have thus been utilized in many scientific research fields. For example, ILs may be utilized in energy devices, including solar cells, batteries, and supercapacitors. Thermal conductivity and thermal diffusivity of ILs are crucial for real energy conversion and energy storage processes. However, the thermal conductivity and thermal diffusivity of ILs are often unknown. Therefore, in this work, the thermal conductivity and thermal diffusivity of ILs are investigated. A thermal conductivity and thermal diffusivity measurement method for ILs are developed.

Thermal conductivity of pure ILs $BmimBF_4$, $BmimPF_6$, OmimCl, $BmimFeCl_4$, and $OmimFeCl_4$ is measured. It is found that the thermal conductivity of the five pure ILs is much lower than the thermal conductivity of water. The effect of NPs on thermal conductivity of ILs is also investigated. It is shown that the thermal conductivity of $BmimBF_4$ does not change significantly in the presence of Fe_2O_3 NPs. However, the thermal conductivity of $BmimPF_6$ decreases somewhat in the presence of R711 NPs.

Furthermore, thermal diffusivity of ILs is measured in this work. Thermal diffusivity of five pure ILs, including $BmimBF_4$, $BmimPF_6$, $BmimFeCl_4$, OmimCl, and $OmimFeCl_4$, is measured. The thermal diffusivity of the ILs is no more than 0.1185 $mm^2 s^{-1}$ at 21 °C. The thermal diffusivity of water is 0.143 $mm^2 s^{-1}$ at 25 °C, which means ILs have a better property than water for energy storage. Therefore, ILs may be considered as a type of novel materials for energy storage. The effect of NPs on the thermal diffusivity of ILs is also investigated. It is shown that the thermal diffusivity of $BmimBF_4$ does not change significantly in the presence of Fe_2O_3 NPs. However, the thermal diffusivity of $BmimPF_6$ decreases about 10.6 % in the presence of R711 NPs.

Acknowledgements The authors acknowledge UiT The Arctic University of Norway for financial support.

References

1. Bidikoudi M, Perganti D, Karagianni C-S, Falaras P. Solidification of ionic liquid redox electrolytes using agarose biopolymer for highly performing dye-sensitized solar cells. Electrochim Acta. 2015;179:228–36.
2. Erten-Ela S, Ocakoglu K. Iridium dimer complex for dye sensitized solar cells using electrolyte combinations with different ionic liquids. Mater Sci Semicond Process. 2014;27:532–40.

3. Hashmi SG, Ozkan M, Halme J, Misic KD, Zakeeruddin SM, Paltakari J, Grätzel M, Lund PD. High performance dye-sensitized solar cells with inkjet printed ionic liquid electrolyte. Nano Energy. 2015;17:206–15.
4. Khanmirzaei MH, Ramesh S, Ramesh K. Polymer electrolyte based dye-sensitized solar cell with rice starch and 1-methyl-3-propylimidazolium iodide ionic liquid. Mater Des. 2015;85:833–7.
5. Lin B, Shang H, Chu F, Ren Y, Yuan N, Jia B, Zhang S, Yu X, Wei Y, Ding J. Ionic liquid-tethered graphene oxide/ionic liquid electrolytes for highly efficient dye sensitized solar cells. Electrochim Acta. 2014;134:209–14.
6. Ng HM, Ramesh S, Ramesh K. Efficiency improvement by incorporating 1-methyl-3-propylimidazolium iodide ionic liquid in gel polymer electrolytes for dye-sensitized solar cells. Electrochim Acta. 2015;175:169–75.
7. Apostolopoulou A, Nagygyörgy V, Madarász J, Stathatos E, Pokol G. Thermal stability and electrical studies on hybrid and composite sol–gel quasi-solid-state electrolytes for dye-sensitized solar cells. J Therm Anal Calorim. 2015;121:371–80.
8. Ding C, Nohira T, Hagiwara R, Matsumoto K, Okamoto Y, Fukunaga A, Sakai S, Nitta K, Inazawa S. Na[FSA]-[C3C1pyrr][FSA] ionic liquids as electrolytes for sodium secondary batteries: effects of Na ion concentration and operation temperature. J Power Sources. 2014;269:124–8.
9. Ejigu A, Greatorex-Davies PA, Walsh DA. Room temperature ionic liquid electrolytes for redox flow batteries. Electrochem Commun. 2015;54:55–9.
10. Guisao JPT, Romero AJF. Interaction between Zn^{2+} cations and n-methyl-2-pyrrolidone in ionic liquid-based gel polymer electrolytes for Zn batteries. Electrochim Acta. 2015;176:1447–53.
11. He X, Wang J, Jia H, Kloepsch R, Liu H, Beltrop K, Li J. Ionic liquid-assisted solvothermal synthesis of hollow Mn_2O_3 anode and $LiMn_2O_4$ cathode materials for Li-ion batteries. J Power Sources. 2015;293:306–11.
12. Hofmann A, Schulz M, Indris S, Heinzmann R, Hanemann T. Mixtures of ionic liquid and sulfolane as electrolytes for Li-ion batteries. Electrochim Acta. 2014;147:704–11.
13. Jiang M, Wang X, Shen Y, Hu H, Fu Y, Yang X. New iron-based fluoride cathode material synthesized by non-aqueous ionic liquid for rechargeable sodium ion batteries. Electrochim Acta. 2015;186:7–15.
14. Krummacher J, Passerini S, Balducci A. Ionic liquid assisted solid-state synthesis of lithium iron oxide nanoparticles for rechargeable lithium ion batteries. Solid State Ionics. 2015;280:37–43.
15. Kuo P-L, Tsao C-H, Hsu C-H, Chen S-T, Hsu H-M. A new strategy for preparing oligomeric ionic liquid gel polymer electrolytes for high-performance and nonflammable lithium ion batteries. J Membr Sci. 2016;499:462–9.
16. Wu F, Zhu Q, Chen R, Chen N, Chen Y, Ye Y, Qian J, Li L. Ionic liquid-based electrolyte with binary lithium salts for high performance lithium–sulfur batteries. J Power Sources. 2015;296:10–7.
17. Arbizzani C, Beninati S, Lazzari M, Soavi F, Mastragostino M. Electrode materials for ionic liquid-based supercapacitors. J Power Sources. 2007;174:648–52.
18. Awale DV, Bhise SC, Patil SK, Vadiyar MM, Jadhav PR, Navathe GJ, Kim JH, Patil PS, Kolekar SS. Nanopetals assembled copper oxide electrode for supercapacitor using novel 1-(1′-methyl-2′-oxo-propyl)-2,3-dimethylimidazolium chloride ionic liquid as an electrolyte. Ceram Int. 2016;42:2699–705.
19. Balducci A, Bardi U, Caporali S, Mastragostino M, Soavi F. Ionic liquids for hybrid supercapacitors. Electrochem Commun. 2004;6:566–70.
20. Huang P-L, Luo X-F, Peng Y-Y, Pu N-W, Ger M-D, Yang C-H, Wu T-Y, Chang J-K. Ionic liquid electrolytes with various constituent ions for graphene-based supercapacitors. Electrochim Acta. 2015;161:371–7.
21. Maiti S, Pramanik A, Chattopadhyay S, De G, Mahanty S. Electrochemical energy storage in montmorillonite K10 clay based composite as supercapacitor using ionic liquid electrolyte. J Colloid Interface Sci. 2016;464:73–82.
22. Pandey GP, Hashmi SA. Performance of solid-state supercapacitors with ionic liquid 1-ethyl-3-methylimidazolium tris(pentafluoroethyl) trifluorophosphate based gel polymer electrolyte and modified MWCNT electrodes. Electrochim Acta. 2013;105:333–41.
23. Sathyamoorthi S, Suryanarayanan V, Velayutham D. Organo-redox shuttle promoted protic ionic liquid electrolyte for supercapacitor. J Power Sources. 2015;274:1135–9.
24. Shao Q, Tang J, Lin Y, Li J, Qin F, Zhang K, Yuan J, Qin L-C. Ionic liquid modified graphene for supercapacitors with high rate capability. Electrochim Acta. 2015;176:1441–6.
25. Timperman L, Galiano H, Lemordant D, Anouti M. Phosphonium-based protic ionic liquid as electrolyte for carbon-based supercapacitors. Electrochem Commun. 2011;13:1112–5.
26. Wei D, Ng TW. Application of novel room temperature ionic liquids in flexible supercapacitors. Electrochem Commun. 2009;11:1996–9.
27. Yang L, Hu J, Lei G, Liu H. Ionic liquid-gelled polyvinylidene fluoride/polyvinyl acetate polymer electrolyte for solid supercapacitor. Chem Eng J. 2014;258:320–6.
28. Zheng C, Qian W, Yu Y, Wei F. Ionic liquid coated single-walled carbon nanotube buckypaper as supercapacitor electrode. Particuology. 2013;11:409–14.
29. Feng W, Lu Y, Chen Y, Lu Y, Yang T. Thermal stability of imidazolium-based ionic liquids investigated by TG and FTIR techniques. J Therm Anal Calorim. 2016;125:143–54.
30. Jagadeeswara Rao C, Venkata Krishnan R, Venkatesan KA, Nagarajan K, Srinivasan TG. Thermochemical properties of some bis(trifluoromethyl–sulfonyl)imide based room temperature ionic liquids. J Therm Anal Calorim. 2009;97:937–43.
31. Sattari M, Gharagheizi F, Ilani-Kashkouli P, Mohammadi AH, Ramjugernath D. Development of a group contribution method for the estimation of heat capacities of ionic liquids. J Therm Anal Calorim. 2014;115:1863–82.
32. Albert J, Müller K. Thermal conductivity of Ionic Liquids: an estimation approach. Chem Eng Sci. 2014;119:109–13.
33. Lazzús JA. A group contribution method to predict the thermal conductivity $\lambda(T, P)$ of ionic liquids. Fluid Phase Equilib. 2015;405:141–9.
34. Lazzús JA, Pulgar-Villarroel G. Estimation of thermal conductivity of ionic liquids using quantitative structure–property relationship calculations. J Mol Liq. 2015;211:981–5.
35. Frez C, Diebold GJ, Tran CD, Yu S. Determination of thermal diffusivities, thermal conductivities, and sound speeds of room-temperature ionic liquids by the transient grating technique. J Chem Eng Data. 2006;51:1250–5.
36. Ge R, Hardacre C, Nancarrow P, Rooney DW. Thermal Conductivities of Ionic Liquids over the Temperature Range from 293 K to 353 K. J Chem Eng Data. 2007;52:1819–23.
37. Fröba AP, Rausch MH, Krzeminski K, Assenbaum D, Wasserscheid P, Leipertz A. Thermal conductivity of ionic liquids: measurement and prediction. Int J Thermophys. 2010;31:2059–77.
38. Verevkin SP, Emel'yanenko VN, Zaitsau DH, Ralys RV, Schick C. Ionic liquids: differential scanning calorimetry as a new indirect method for determination of vaporization enthalpies. J Phys Chem B. 2012;116:4276–85.

39. Bodirlau R, Teaca C-A, Spiridon I. Influence of ionic liquid on hydrolyzed cellulose material: FT-IR spectroscopy and TG–DTG–DSC analysis. Int J Polym Anal Charact. 2010;15:460–9.
40. Yansong Zhao JHH, Boström T. Extraction of magnetic nanoparticles using magnetic ionic liquids. Micro Nano Lett. 2016;11(5):244–7.
41. Shojaee SA, Farzam S, Hezave AZ, Lashkarbolooki M, Ayatollahi S. A new correlation for estimating thermal conductivity of pure ionic liquids. Fluid Phase Equilib. 2013;354:199–206.

Paper 6

Ionic liquid based electrolytes preparation and characterization of density, viscosity, crystallization temperature, decomposition temperature, ionic conductivity, and electrochemical window

(Under review)

Paper 7

Rechargeable iron-ion battery using pure ionic liquid electrolyte

ACS Omega, 2022, doi: 10.1021/acsomega.1c06170. (*Published*)

Rechargeable iron-ion battery using pure ionic liquid electrolyte

Yansong Zhao*, Yingpeng Zhen, and Tobias Boström

*Corresponding Author:
Yansong Zhao — Department of Safety, Chemistry and Biomedical Laboratory Sciences, Faculty of Engineering and Science, Western Norway University of Applied Sciences (HVL), 5020 Bergen, Norway.

E-mails: yansong.zhao2004@gmail.com; yansong.zhao@hvl.no

Authors

Yingpeng Zhen — Department of Civil and Environmental Engineering, Norwegian University of Science and Technology (NTNU), NO-7491 Trondheim, Norway.
E-mails: ypzhen521@gmail.com; yingpeng.zhen@ntnu.no

Tobias Boström — Renewable Energy Group, Department of Physics and Technology, UiT The Arctic University of Norway, NO-9037 Tromsø, Norway.
E-mail: tobias.bostrom@uit.no

Abstract

A rechargeable iron-ion battery (Fe-ion battery) has been produced in our laboratory using pure ionic liquid electrolyte. Magnetic ionic liquids of 1-butyl-3-methylimidazolium tetrachloroferrate ($BmimFeCl_4$) and 1-methyl-3-octylimidazolium tetrachloroferrate ($OmimFeCl_4$) are synthesized and utilized as electrolytes in this work. Chemical structure of the two ionic liquids (ILs) is investigated using Raman analysis. In addition, physical and thermal stability properties of ionic liquid (IL) $BmimFeCl_4$, including density, viscosity, melting point and decomposition temperature, are investigated using density meter, viscosity meter, differential scanning calorimetry (DSC) and thermogravimetric analysis (TGA). Moreover, electrochemical properties, including electrochemical window, and ionic conductivity of IL $BmimFeCl_4$ are investigated using electrochemical instrument and conductivity meter. It is found that magnetic IL $BmimFeCl_4$ has good physical and electrochemical properties to be utilized as electrolyte for iron-ion battery fabrication. Cathode of Fe-ion battery is iron containing materials, including pure iron foil, carbon coated iron nanoparticles, and iron powder. Anode of Fe-ion battery is graphite. Electrochemical properties of full cells are investigated, including cyclic voltammetry curves, and specific charge-discharge capacity. Fe-ion battery is a unique rechargeable ion battery with magnetic ions. In addition, pure IL $BmimFeCl_4$ is utilized as electrolyte in this Fe-ion battery. IL $BmimFeCl_4$ is stable and almost non-volatile.

Therefore, Fe-ion battery with pure IL electrolyte is safer than organic electrolyte. Fe-ion battery using pure IL electrolyte is a promising battery with many potential applications.

Keywords: Ionic liquid, iron-ion battery, magnetic battery, rechargeable battery.

Introduction

Lithium (Li) based batteries are becoming more and more important as energy storage devices in many applications. However, Li based batteries have some disadvantages, for example, high cost, safety issues, and low abundance in the earth [1,2]. Therefore, many researchers try to develop new types of batteries to solve the problems of Li based batteries, including sodium battery [3], and magnesium battery [4]. However, cost of sodium (Na) battery and magnesium (Mg) battery is still high. Actually, Fe is the cheapest metal among all the metallic materials. In addition, there are plenty of mineable Fe on the earth, ca. 230 billion tons, which is about 15 000 times as high as the amount of mineable Li in the earth. The element abundance of Fe rank No.1 in the universe and No.2 on earth among the metallic elements.[5,6] It means that there are plenty of Fe in the nature for the iron-ion (Fe-ion) battery fabrication. Therefore, Fe is a cheapest metal for new generation battery fabrication. The cost of the Fe-ion battery is potentially much lower than the other batteries mentioned above. In addition, Fe-ion battery is an extremely safe battery. The electrodes inside of Fe-ion battery are not oxygen or water sensitive. Fe-ion battery is highly stable and there is no explosion risk in Fe-ion battery. In this work, we have developed a rechargeable Fe-ion battery. Moreover, for Fe-ion battery obtained in our laboratory, a pure ionic liquid (IL) is utilized as the electrolyte to replace the organic solvent electrolyte in the traditional batteries.

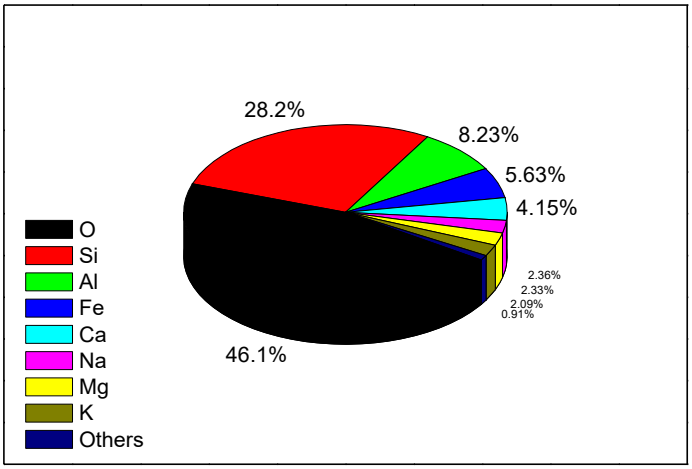

(a)

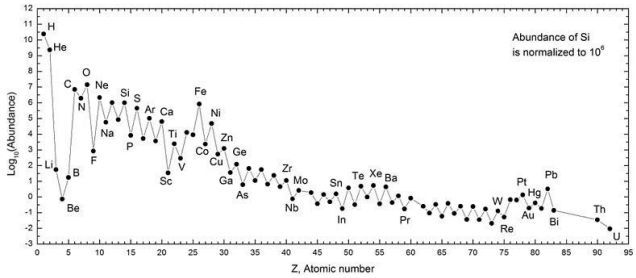

(b)

Figure 1. Abundance of iron in the earth (a) and the universe (b). [5,6]

Reprinted (Adapted or Reprinted in part) with permission from www.wikipedia.org. Copyright 2022, Wikipedia.

ILs are types of salts. Presently, ILs are a hot research topic. Plenty of ILs are liquid at room temperature. Many ILs are liquid at temperatures as low as -60 °C and can be utilized in cold climate areas. ILs are regarded as environmentally friendly materials [7,8]. ILs have been utilized as novel and promising materials in many research fields [9-11], including material science, separation science, catalysis science, medicine science, as well as energy and climate technology. Utilization of ILs in energy conversion and energy storage, including solar cells [12], batteries [13], and supercapacitors [14], is a crucial topic. ILs are utilized as electrolytes in batteries by many researchers to improve the performance of current battery.

In this work, electrolyte and electrode materials are selected for new generation battery fabrication. Pure IL $BmimFeCl_4$ is utilized as electrolyte in rechargeable Fe-ion battery to replace traditional organic solvents. IL $BmimFeCl_4$ can be easily obtained using one step synthesis method [15, 16]. In addition, IL $BmimFeCl_4$ is very stable and is not water or oxygen sensitive. Moreover, IL $BmimFeCl_4$ electrolyte is not flammable, which can increase the safety property of battery significantly. Chemical structure, physical and thermal properties of IL $BmimFeCl_4$ are investigated using Raman analysis, density meter, viscosity meter, differential scanning calorimetry (DSC), and thermogravimetric analysis (TGA). Electrochemical properties are important to utilize ILs as electrolyte. Therefore, in this work, ionic conductivity of $BmimFeCl_4$ is investigated using conductivity meter. Electrochemical window of $BmimFeCl_4$ is investigated using electrochemical instrument.

Fe-ion battery has a lot of potential applications, including in stationary energy storage device, in buildings, railways, wireless charging smart road, electrical cars, electric ships, mobile devices, space technology, as well as large scale renewable energy storage systems.

Experimental Section

Materials. ILs of 1-Butyl-3-methylimidazolium chloride (CAS R.N. 79917-90-1, BmimCl), and 1-methyl-3-octylimidazolium chloride (CAS R.N. 64697-40-1, OmimCl) are obtained from Sigma-Aldrich. Mass fraction purities of the 2 ILs are ⩾ 97 %, 97 %, respectively. $FeCl_3 \cdot 6H_2O$ and Fe_2O_3 nanoparticles (Average size: < 50 nm) are also purchased from Sigma-Aldrich. In addition, carbon coated iron (C-Fe) nanoparticles (NPs) are purchased from Sigma-Aldrich and utilized for cathode preparation.

Sodium carboxymethyl cellulose (CMC, Dow Wolff Cellulosics), the conductive carbon black (Super C45, Super C60, IMER Graphite & Carbon), and graphite are also utilized for electrode preparation. Glass fiber is utilized as a separator in cells.

IL electrolyte preparation and treatment. ILs of $BmimFeCl_4$ and $OmimFeCl_4$ are synthesized in the laboratory according to our previous work [16]. Subsequently, the obtained ILs are dried in the dry room using the method shown as follows. All the ILs are dried using the vacuum pump in a dry room. Water content in the dry room is < 25 ppm. The ILs drying procedure is shown as follows. Firstly, an IL is dried in the dry room using the membrane pump for at least 2 days. The vacuum pressure of the final dried ILs pressure is ca. 10^{-3} mbar. Subsequently, the pre-dried IL is dried further using extremely high vacuum (10^{-7}~10^{-8} mbar) pressure pump to dry for at least 3 days at a certain temperature to remove the water and solvent in the IL. Water content of final obtained $BmimFeCl_4$ and $OmimFeCl_4$ is less than 25 ppm.

Density measurement. Densities of $BmimFeCl_4$ are measured using a density meter (Anton Paar DMA 4100, Anton Paar Co., Austria). The temperature of this study was between (293.15 and 358.15) K, at 5 K intervals. The temperature error is ± 0.01 ºC. The measurement is performed in the dry room (water content of the dry room is < 25 ppm). The absolute room pressure was approximately 101 kPa during the measurement.

Viscosity measurement. Viscosity of $BmimFeCl_4$ is measured using a rheometer (MCR 102, Anton Paar Modular Compact Rheometer). Viscosity of $BmimFeCl_4$ is measured at shear rates ranging from 1 s^{-1} to 100 s^{-1} at various temperatures ranging from 10 ºC to 50 ºC.

DSC (differential scanning calorimetry) curve measurement. Melting point of $BmimFeCl_4$ is measured using DSC (Netzsch, Germany). Measurement procedure is as follow. A sample is loaded in the pan. The sample is cooled to -150 ºC. Subsequently, the sample is kept at -150 ºC for 5 minutes. Afterwards, the sample is heated to -120 °C at a cooling rate of 5 °C/min and maintained at -120 °C

for 5 min. Subsequently, the sample is heated to 20 °C at 1 °C/min and heat flow is measured during the process.

TGA (Thermogravimetric analysis) curve measurement. Thermal stability of ILs based electrolytes is measured using TGA (TA instruments, USA). A sample is loaded in the pan. Subsequently, the sample is maintained at 35 °C for 10 min. The sample is heated to 600 °C at a heating rate of 5 °C/min from 35 °C. Heat flow is measured during the heating process. The weight of pan and sample are needed for the experiments.

Raman analysis. The chemical structure of magnetic ILs of $BmimFeCl_4$ and $OmimFeCl_4$ is characterized using Raman spectroscopy (Vertex 70V, Bruker, Germany). A capillary is utilized for the measurement. One side of the capillary is closed, and the other side of the capillary is open. Firstly, the capillary is kept in an oven at 120 ºC in the dry room for at least 24 hours to remove the possible water inside of the capillary. Subsequently, IL sample is filled into the capillary in the argon-filled glovebox. The water content and oxygen content in the glovebox is below 0.1 ppm. After IL sample is filled into the capillary, the open side of the capillary is closed to form an isolated system. In the end, the capillary with IL sample is moved into Raman spectroscopy from glovebox. By this way, the IL sample filled into the capillary cannot influence by the atmosphere, such as water, O_2, and CO_2. The measurement is performed at room temperature. The sample is filled into a capillary for the measurement.

Ionic conductivity measurement. Ionic conductivity of $BmimFeCl_4$ electrolyte is measured using conductivity meter at temperatures ranging from -30 ºC to 100 ºC. The temperature profile at ionic conductivity measurement is as follows. The temperature is increasing from -30 ºC to 100 ºC. Subsequently, the temperature is decreasing from 100 ºC to 20 ºC.

Electrochemical window measurement. Electrochemical window of magnetic IL $BmimFeCl_4$ is measured using a multichannel potentiostat (Bio-Logic Science Instruments SAS, France). Experiments are performed at potential vs Ag/Ag^+ ranging from -5.0 V to 5.0 V with scanning rate of 0.5 mV/s. The working electrode is Pt wire with cross sectional area of 0.0078 cm^2. Counter electrode is Ni (cross sectional area: 1.13 cm^2). Reference electrode is silver wire.

Cathode materials preparations. 3 various cathodes, including Pure Fe cathode, carbon coated iron nanoparticles cathode (C-Fe cathode), and carbon reduced Fe_2O_3 cathode (Fe powder cathode), are utilized for Fe-ion battery fabrication. The 3 cathode preparation methods are shown as follows.

(a) Pure Fe cathode. Pure Fe (Purity is ⩾99.99% trace metals basis) is purchased from Sigma Aldrich. Pure Fe is utilized as cathode for Fe-ion battery directly.

(b) C-Fe cathode. The C-Fe cathode is prepared as follows. Step 1: CMC is dissolved in H_2O to form a gel-like sample by stirring for at least 2 hours. Step 2: the carbon coated Fe NPs and carbon 45 is added into the gel-like sample. Afterwards, the sample is stirred for at least 12 hours to obtain a slurry. Step 3: The slurry is coated on the surface of Ni foil using a doctor blade to form a 200 μm thin film. Step 4: The Ni foil with thin film is heated at 80 ºC for at least 12 hours to remove the water. Step 5: The Ni foil with thin film is cut to obtain C-Fe electrodes. Afterwards, the C-Fe electrodes are further dried using high vacuum pump. Finally, the C-Fe electrodes are obtained for battery preparation.

(c) Fe powder cathode. The Fe powder cathode is prepared method is similar to the method for C-Fe cathode preparation. However, in Step 2, the Fe powder reduced from Fe_2O_3 by carbon 45 is added into the gel-like sample. The reduced Fe powder is prepared as follow. The mixture of Fe_2O_3, sucrose, and super C65 is burnt at 1000 ºC for 1 hour to get a powder. The powder is utilized for the cathode preparation. The rest steps of Fe powder cathode preparation are similar to that of C-Fe cathode preparation.

Anode materials preparation. Graphite is utilized as anode in Fe-ion battery. The graphite electrode preparation process is as follows. Step 1: CMC is dissolved in H_2O to form a gel-like sample by stirring for at least 2 hours. Step 2: graphite and carbon 45 is added into the gel-like sample. Afterwards, the sample is stirred for at least 12 hours to obtain a slurry. Step 3: The slurry is coated as a 150μm thin film on the surface of Ni foil using a doctor blade. Step 4: The Ni foil with thin graphite film is heated at 80 ºC for at least 12 hours to remove the water. Step 5: The Ni foil with the thin graphite film is cut into graphite electrodes. Afterwards, the graphite electrode is further dried using high vacuum pump. Finally, the graphite electrodes are obtained for battery preparation.

Electrolyte preparation. Magnetic ILs of 1-butyl-3-methylimidazolium tetrachloroferrate ($BmimFeCl_4$) and 1-methyl-3-octylimidazolium tetrachloroferrate ($OmimFeCl_4$) are synthesized in the laboratory according to our previous work [16]. Subsequently, the water content of the ILs is removed in the dry room of our laboratory using high vacuum pump.

Current collector selection. The current collectors for the electrode preparation are chosen between Cu, Ni, and Al foils. A Ni-Ni symmetric cell, Cu-Cu symmetric cell, and Al-Al symmetric cell are prepared. The electrolyte utilized in the cells is $BmimFeCl_4$. All the symmetric cells are fabricated in an argon-filled glovebox (MBraun UNIlab; H_2O content < 0.1 ppm, O_2 content < 0.1 ppm) filled with ultrapure Argon. The cyclic voltammetry (CV) test of the three symmetric cells is performed using

galvanostat/potentiostat VMP (Bio-Logic, France). In addition, graphite-graphite symmetric cell is prepared. The electrolyte in the cell is pure $BmimFeCl_4$. Subsequently, the CV test of the graphite-graphite cell is performed.

Corrosion test. The corrosion effect of $BmimFeCl_4$ on Cu, Al, and Ni foils is investigated in the dry room (water content < 25 ppm) at our laboratory. In this test, firstly, Cu, Al, and Ni foils are put into 3 experimental vials, respectively. Subsequently, 2 drops of $BmimFeCl_4$ are placed on the surface of Cu, Al and Ni foils. In addition, there are reference Cu, Al and Ni foils without $BmimFeCl_4$ on the surface. The foils with and without $BmimFeCl_4$ are kept quiescently on laboratory bench for 40 days at room temperature. In the end, the foil surface photos are taken during the corrosion test.

CV test of Fe-Graphite full cell. The Fe-Fe symmetric cell, C-Fe-C-Fe symmetric cell, and Fe powder-Fe powder symmetric cells are prepared for CV tests. The electrolyte in the symmetric cells is $BmimFeCl_4$. The test is performed using VMP.

Charge and discharge of full cell. All the galvanostatic charge discharge experiments are performed using a Maccor Battery Tester 4300. Three full cells of Fe graphite cell, C-Fe graphite cell, and Fe powder graphite are prepared for charge and discharge test. The electrolyte in the symmetric cells is $BmimFeCl_4$. The reference electrode is Ag.

SEM. The morphology of the electrode materials utilized this work is characterized using SEM (SEM, ZEISS 1550VP Field Emission Scanning Electron Microscope operated at 5 kV). The experiments are performed at room temperature.

Results and Discussion

Density measurement. Density of $BmimFeCl_4$ is measured using a density meter in this work. Density data of the IL are shown in Figure 2 (a). It illustrates that density of the IL decreases with an increase in temperature between 20 ºC to 80 ºC. In addition, it is shown that $BmimFeCl_4$ has a high density. This property is good when ILs is utilized as an electrolyte in a battery. It means that for the same mass, $BmimFeCl_4$ will take up less volume.

Viscosity and rheological property measurement. Viscosity and rheological property of $BmimFeCl_4$, are measured at temperature of 20 ºC. The results are shown in Figure 2 (b). $BmimFeCl_4$ has the lower viscosity values compared with conventional ILs. A low viscosity is advantageous since the ions easier can drift between the electrodes. In addition, as shown in Figure 2(b), the viscosity of IL $BmimFeCl_4$ decreases with an increasing temperature, ranging from 10 ºC to 50 ºC, which is in agreement with the viscosity versus temperature trend of conventional ILs.

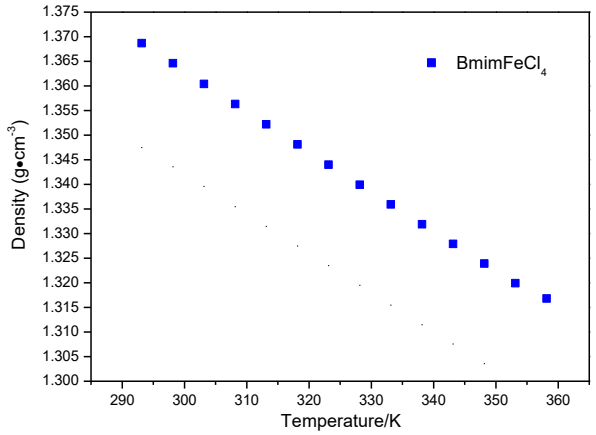

(a)

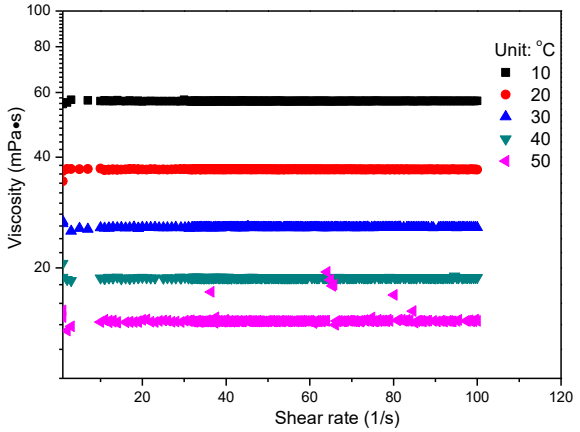

(b)

Figure 2. Density and viscosity of IL BmimFeCl4. (a) Density of BmimFeCl4 at temperatures from 20 ºC to 80 ºC; (b) Viscosity of BmimFeCl4 at temperatures ranging from 10 ºC to 50 ºC.

DSC curve measurement. Melting point of BmimFeCl4 is measured using DSC. DSC curve of BmimFeCl4 is shown in Figure 3. It illustrates that BmimFeCl4 has very low melting point, namely ca. -85 ºC. This means that BmimFeCl4 electrolyte can be utilized in very low temperature areas and applications, for example, in the harsh cold Arctic/Antarctic areas. In addition, low melting point is also good to utilize batty for future space technology development.

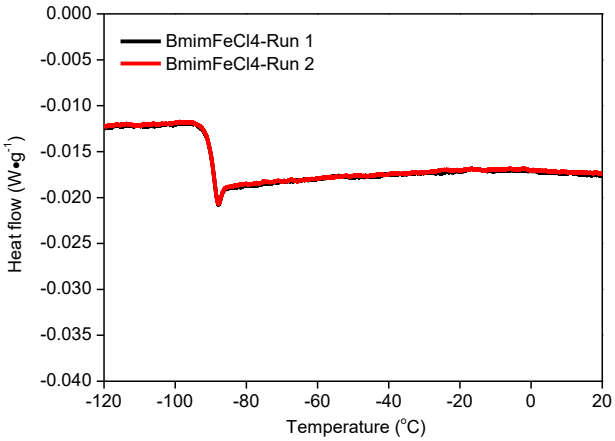

Figure 3. DSC curves for $BimFeCl_4$, crystalline temperature determination.

TGA curve measurement. Thermal stability of $BmimFeCl_4$ electrolytes is measured using TGA. The TGA curves are shown in Figure 4. It is shown that IL $BmimFeCl_4$ has high thermal stability, the decomposition temperature of which is ca. 459 °C. This means that $BmimFeCl_4$ has an excellent thermal stability for electrolyte applications, which leads to $BmimFeCl_4$ based battery has an extremely high safety property. This $BmimFeCl_4$ electrolyte is not oxygen or water sensitive, and not flammable. In addition, the cost of this $BmimFeCl_4$ is low.

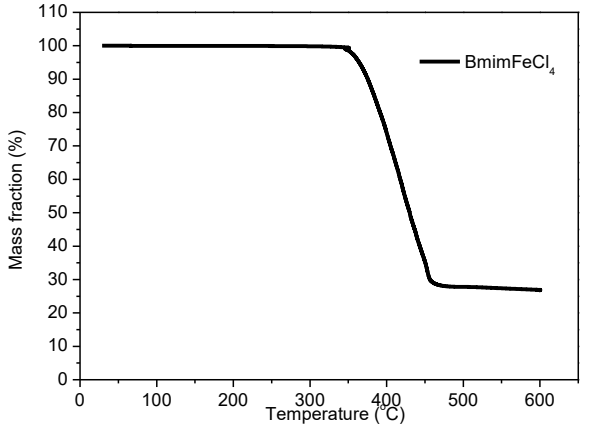

Figure 4. TGA curves of IL $BmimFeCl_4$.

Raman analysis. The chemical structure of magnetic ILs of $BmimFeCl_4$ and $OmimFeCl_4$ is characterized using Raman. The results are shown in Figure 5. The spectrum of $BmimFeCl_4$ and $OmimFeCl_4$ showed a strong band at 330 cm^{-1}, which was assigned to the totally symmetric Fe-Cl stretch variation of $FeCl_4^-$. It illustrates that there is a $FeCl_4^-$ function group in the two ILs. This means that $BmimFeCl_4$ and $OmimFeCl_4$ are synthesized and obtained.

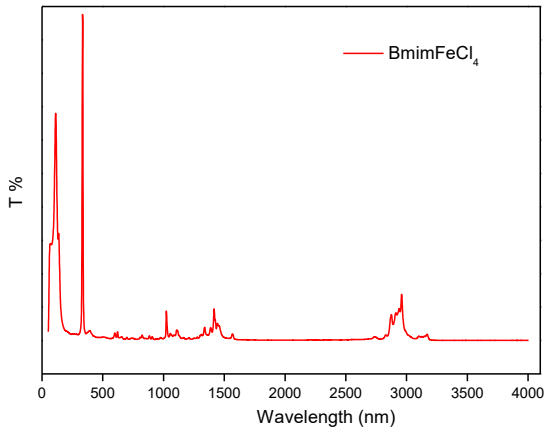

(a)

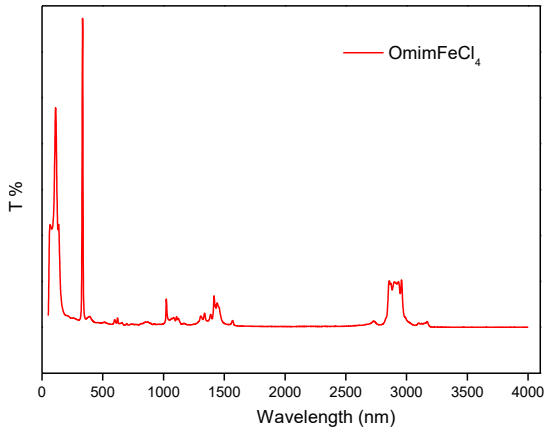

(b)

Figure 5. Raman analysis of magnetic ILs. (a) $BmimFeCl_4$; (b) $OmimFeCl_4$.

Ionic conductivity measurement. Ionic conductivity of magnetic ILs electrolytes is measured using ionic conductivity meter. The results are shown in Figure 6, which illustrates that $BmimFeCl_4$ has a good ionic conductivity. In addition, as shown in Figure 6, the ionic conductivity of $BmimFeCl_4$ is increasing with the increase of temperature.

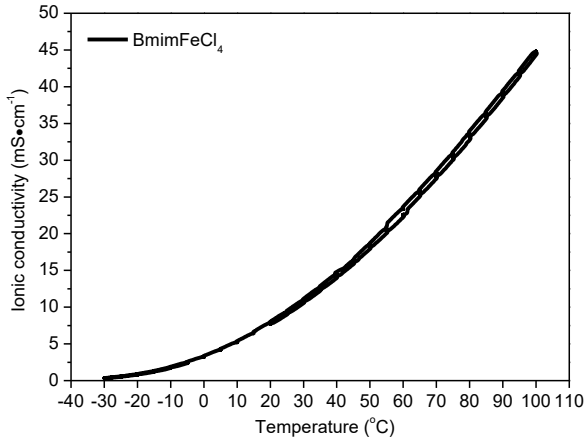

Figure 6. Ionic conductivity measurement of IL $BmimFeCl_4$.

Electrochemical window measurement. Electrochemical window of $BmimFeCl_4$ is measured using VMP. The results are shown in Figure 7. It illustrates that the electrochemical window of $BmimFeCl_4$ is from -2.1 V to 1.9 V versus Ag/Ag^+. Consequently, electrochemical window of $BmimFeCl_4$ is wide enough to be utilized as an electrolyte for Fe-ion battery fabrication.

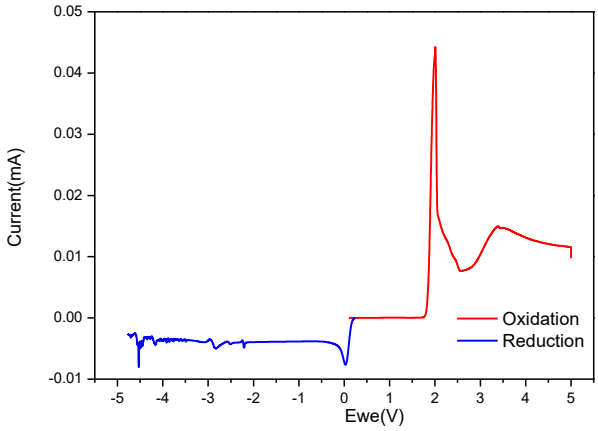

Figure 7. Electrochemical window measurement of IL $BmimFeCl_4$.

Current collector selection. A CV test of a Ni symmetric cell with pure $BmimCl_4$ as the electrolyte is performed. The CV curve are shown in Figure 8. It is shown that the IL $BmimFeCl_4$ is reversible in the Ni symmetric cell. Therefore, this means Ni foil can be an option to utilize as current collector for Fe-ion battery electrodes preparation.

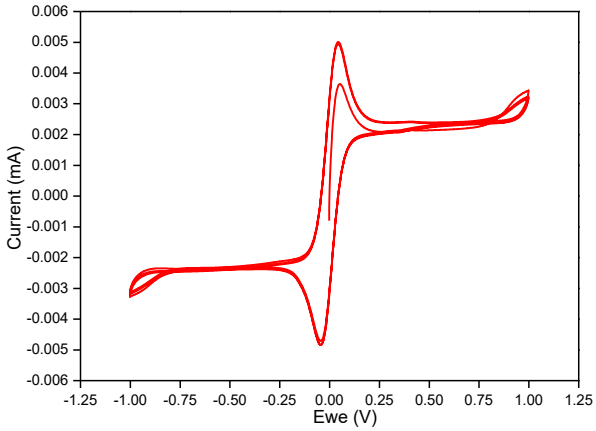

Figure 8. CV test of Ni-Ni symmetric cell.

Corrosion test. The corrosion effect of $BmimFeCl_4$ on Cu, Al, and Ni foils is investigated. The corrosion experiment is performed in a period of 40 days in air and at room temperature. The test results are shown in Figure 9 (a), 9(b) and 9(c). It is shown that $BmimFeCl_4$ can have a chemical reaction with Cu or Al. However, for Ni foil, only a minor chemical reaction can be seen. Therefore, Ni is utilized in the Fe-ion battery fabrication.

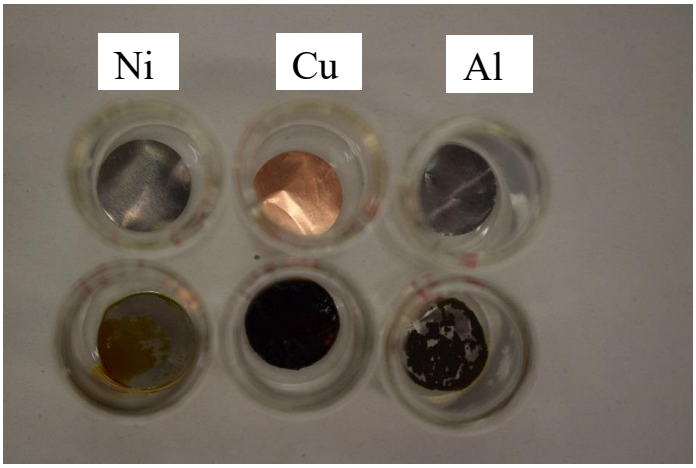

(a)

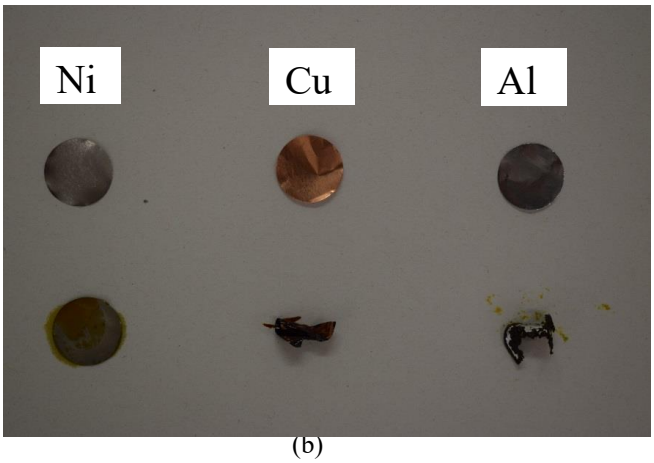

(b)

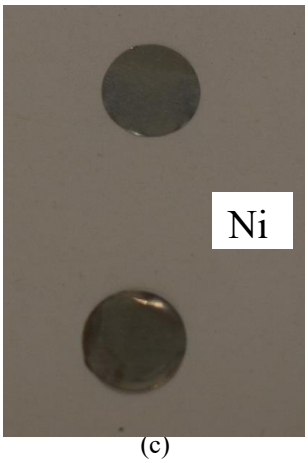

(c)

Figure 9. Corrosion test of $BmimFeCl_4$ on Cu, Al, and Ni. (a) Fresh metal foil without $BmimFeCl_4$ (upper) and with $BmimFeCl_4$ (lower) on the surface. (b) Metal foil without $BmimFeCl_4$ (upper) and with $BmimFeCl_4$ (lower) on the surface after 40 days. (c) Ni foil without $BmimFeCl_4$ (upper) after 40 days and Ni foil treated with $BmimFeCl_4$ for 40 days after cleaning $BmimFeCl_4$ from the surface (lower).

CV test of full cells. Full C-Fe graphite cells are prepared for the CV test. The electrolyte in the full cells is $BmimFeCl_4$. CV test results of the C-Fe graphite full cell are shown in Figures 10. It is shown that C-Fe graphite full cell is completely reversible at -1.5 V to 1.5 V.

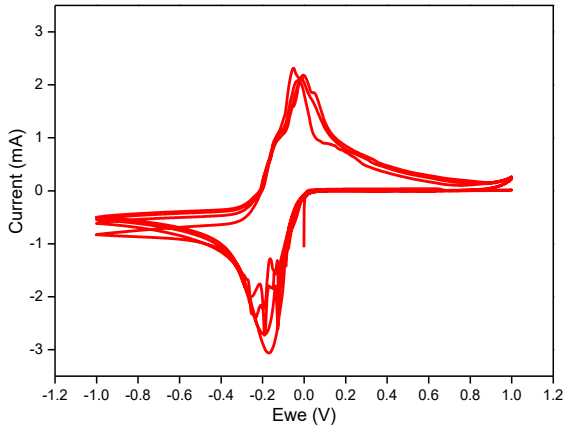

(a)

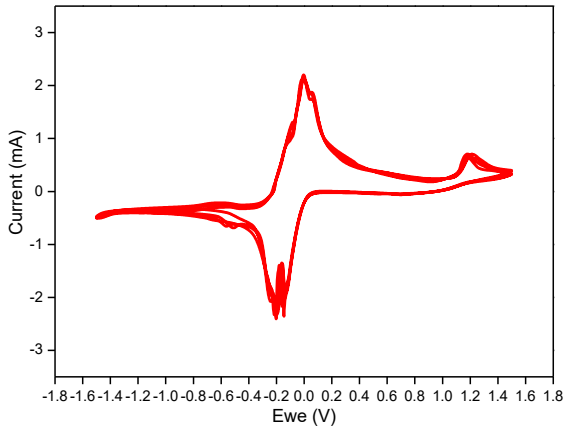

(b)

Figure 10. CV test of a C-Fe graphite full cell. (a) At the voltage ranging from -1 V to 1 V. (b) At the voltage ranging from -1.5 V to 1.5 V. Reference electrode: Ag.

Fe-ion Battery. Structure of a Fe-ion battery is shown in Scheme 1. Electrolyte utilized in battery is magnetic IL BmimFeCl$_4$. Fe element containing materials are utilized as the cathode in this work. Graphite is utilized as the anode in the Fe-ion battery. The proposed working mechanism of Fe-ion battery is due to the movement of Fe^{3+} between the cathode and anode during charge and discharge

processes. This mechanism is similar to Li^+ movement in Li-ion battery during the charge and discharge processes. [17-18]

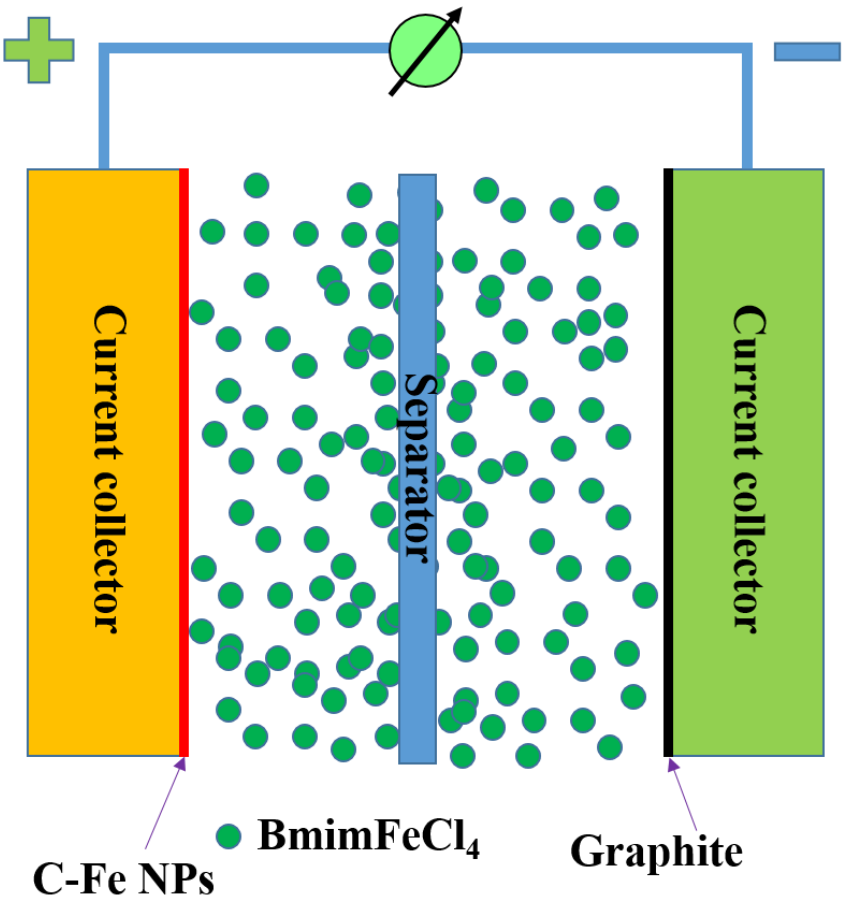

Scheme 1. Structure of a rechargeable Fe-ion battery.

Charge and discharge of full cell. A charge and discharge test of a full Fe-ion battery is performed. The results are shown in Figures 11. The discharge and charge capacity of this cell is around 20-100 mAh/g in the first 100 cycles.

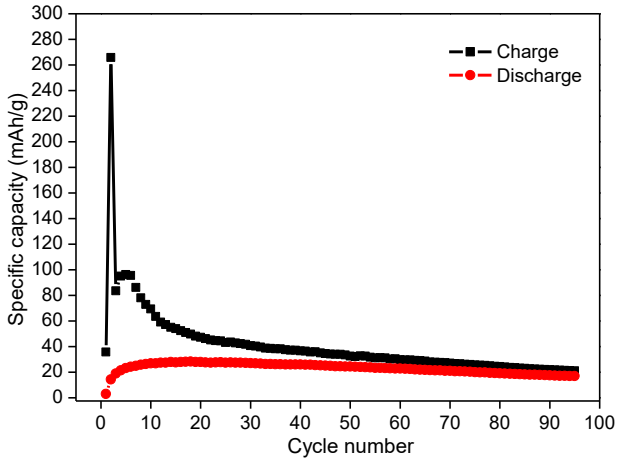

Figure 11. Charge-discharge test of a Fe ion cell.

SEM. SEM pictures of the anode are shown in Figures 12-14. As shown in Figure 12, the C-Fe NPs are found on the surface of the electrode. However, as shown in Figure 13, after charge-discharge cycles the C-Fe NPs are changed and instead form larger sized structures. This means the Fe in the C-Fe NPs is active in the charge and discharge process, which also means that we can utilize C-Fe NPs electrode as cathode. As shown in Figure 14, the surface of the C-Fe NPs anode used as counter electrode in the Swage-type cell, almost does not change. This means that we should use C-Fe NPs electrode as cathode, not anode.

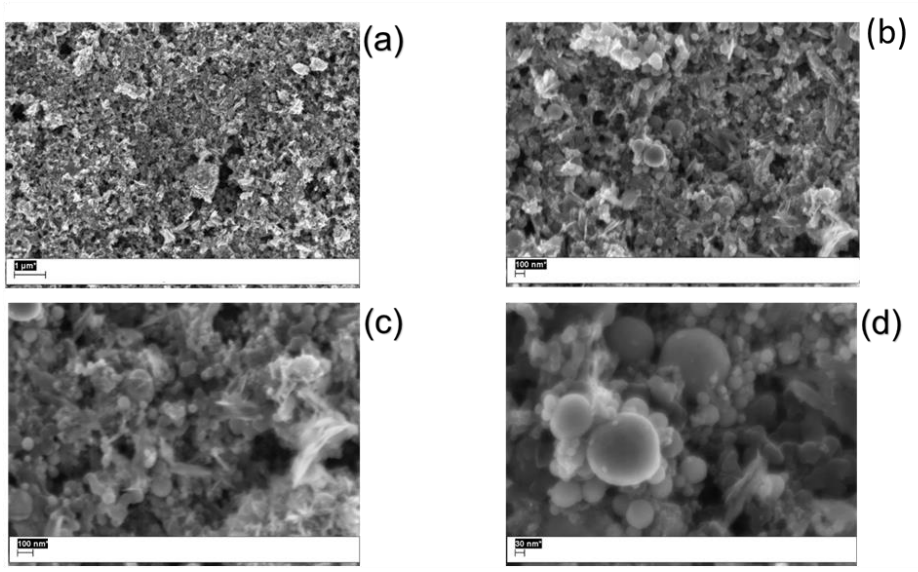

Figure 12. SEM of fresh C-Fe electrode. (a) × 10000; (b) × 30000; (c) × 50000; (d) × 100000.

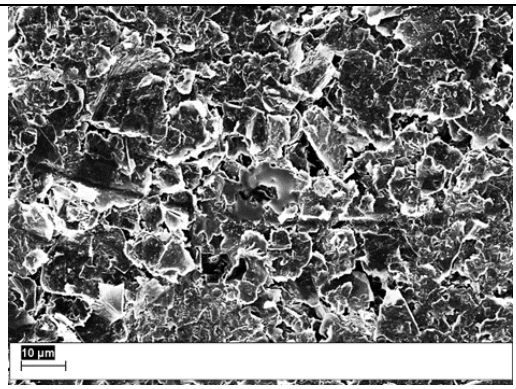

(a)

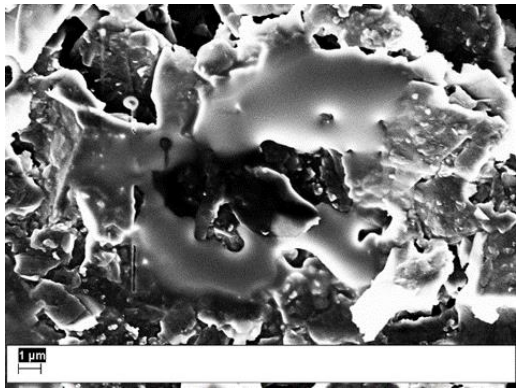

(b)

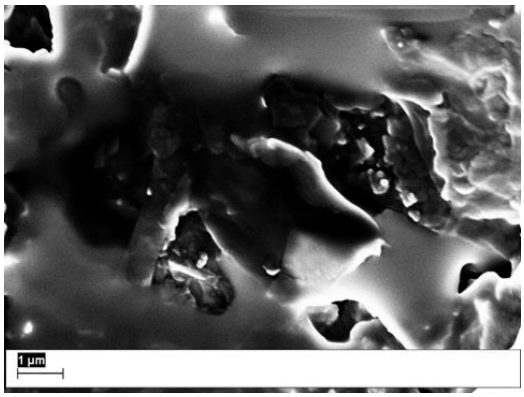

(c)

Figure 13. SEM of used C-Fe electrode from cell after charge and discharge cycles. (a) × 1000; (b) × 5000; (c) × 10000.

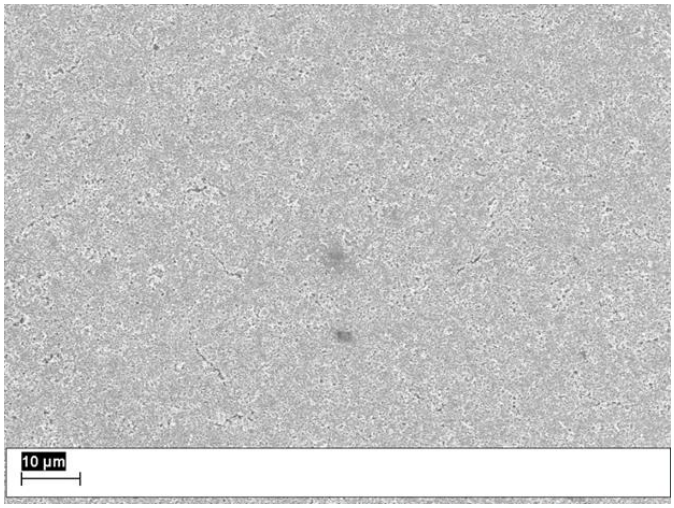

(a)

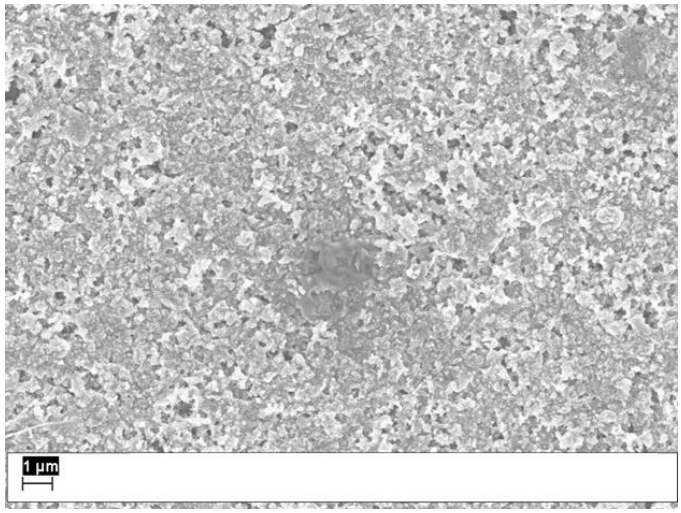

(b)

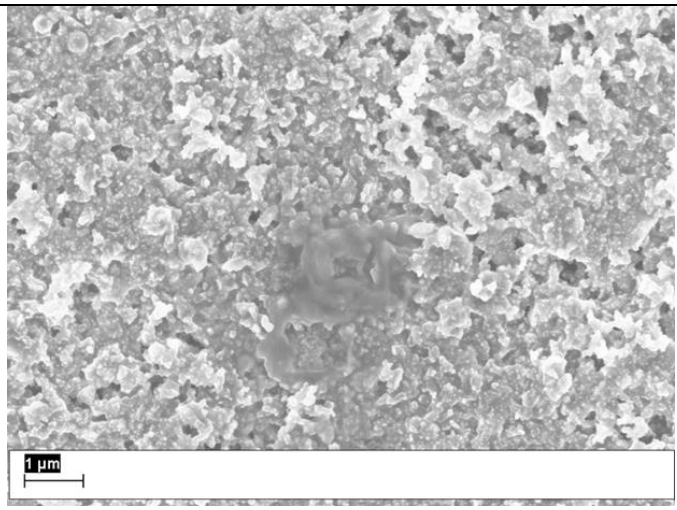

(c)

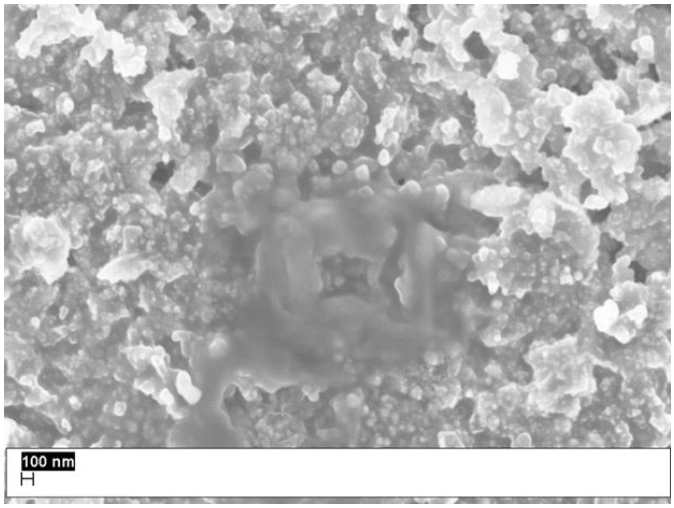

(d)

Figure 14. SEM of a used C-Fe anode from a cell with a graphite cathode after charge and discharge cycles. (a) × 1000; (b) × 5000; (c) × 10000; (d) × 20000.

Conclusions

ILs can be utilized as electrolytes in batteries and supercapacitors. Therefore, in this work, physical, and electrochemical properties of IL electrolyte are investigated using density meter, rheometer, conductivity meter, DSC, TGA, SEM, and electrochemical instrument. Based on the experimental

results, it is found that $BmimFeCl_4$ has good properties to be utilized as electrolyte. Therefore, $BmimFeCl_4$ is selected for Fe-ion rechargeable battery.

Fe-ion battery can be potentially utilized in stationary energy storage device, buildings, railways, electrical cars, electric ships, mobile devices, space technology, and other large scale energy storage systems. Fe is the cheapest metal among all the metallic materials. There is plenty of mineable Fe on the earth. The cost of Fe-ion battery is potentially much lower for example Li-ion batteries. Fe-ion battery is also an extremely safe battery. Electrodes inside Fe-ion battery are not oxygen or water sensitive. Fe-ion battery has highly stable and there is no explosion risk. Importantly, for Fe-ion battery obtained in our laboratory, a pure IL is utilized as the electrolyte to replace the organic solvents in traditional batteries. ILs have many favorable physical and chemical properties such as: non-flammable, high decomposition temperature, low vapor pressure, high ionic conductivity, and a good electrochemical window.

Cathode of Fe-ion battery consists of Fe containing materials, including pure Fe foil, C-Fe NPs, and Fe powder. Various types of Fe-ion full cells are obtained in the laboratory. It is found that Fe-ion battery with C-Fe NPs cathode and $BmimFeCl_4$ electrolyte showed good performance. Electrochemical properties of Fe-ion full cell are investigated, including CV curves, and charge-discharge capacity. In order to understand charge/discharge mechanism of the Fe-ion battery, SEM is utilized to investigate the electrodes surface before and after utilization of the cells. Fe-ion battery is also a magnetic battery. There may be other potential applications due to the magnetic properties of the Fe-ion batteries and non-volatile electrolyte inside of Fe ion battery.

Acknowledgements

The authors acknowledge Norwegian Directorate for Higher Education and Skills for financial support. In addition, the authors are grateful to Helmholtz Institute Ulm, and Karlsruhe Institute of Technology, Germany for the kind support to use their experimental instruments.

References

1 Pan, H.; Hu, Y.; & Chen, L. Room-temperature stationary sodium-ion batteries for large-scale electric energy storage. *Energy Environ. Sci.* **2013***,* 6, 2338-2360.

2 Zu, C.; Li, H. Thermodynamic analysis on energy densities of batteries. *Energy Environ. Sci.* **2011**, 4, 2614-2624.

3 Hartmann, P.; Bender, C.; Vračar, M.; Dürr, A.; Garsuch, A.; Janek, J.; Adelhelm P. A rechargeable room-temperature sodium superoxide (NaO_2) battery. *Nat. Mater.* **2013**, 12, 228-232.

4 Aurbach, D.; Lu, Z.; Schechter, A. ; Gofer, Y.; Gizbar, H.; Turgeman, R.; Cohen, Y.; Moshkovich, M. & E. Levi. Prototype systems for rechargeable magnesium batteries. *Nature* **2000**, 407, 724-727.

5 https://en.wikipedia.org/wiki/Abundance_of_elements_in_Earth%27s_crust (Assessed February 2022)

6 https://en.wikipedia.org/wiki/Oddo%E2%80%93Harkins_rule (Assessed February 2022)

7 Hoogerstraete, V.; Binnemans, K. Highly efficient separation of rare earths from nickel and cobalt by solvent extraction with the ionic liquid trihexyl(tetradecyl)phosphonium nitrate: a process relevant to the recycling of rare earths from permanent magnets and nickel metal hydride batteries. *Green Chem.* **2014**, 16, 1594-1606.

8 Wellens, S.; Thijs, B.; Binnemans, K. An environmentally friendlier approach to hydrometallurgy: highly selective separation of cobalt from nickel by solvent extraction with undiluted phosphonium ionic liquids. *Green Chem.* **2012**, 14, 1657-1665.

9 Asadi, M.; Kim, K.; Liu, C.; Addepalli, A.; Abbasi, P.; Yasaei, P.; Phillips, P.; Behranginia, A.; Cerrato, J.; Haasch, R.; Zapol, P.; Kumar, B.; Klie, R.; Abiade, J.; Curtiss, L.; Salehi-Khojin, A. Nanostructured transition metal dichalcogenide electrocatalysts for CO_2 reduction in ionic liquid. *Science* **2016**, 353, 467-470.

10 Rosen, B. Salehi-khojin, A.; Thorson, M.; Zhu, W.; Whipple, D.; Kenis, P.; Masel, R. Ionic Liquid–Mediated Selective Conversion of CO_2 to CO at Low Overpotentials. *Science* **2011**, 334, 643-644.

11 Lei, Z.; Chen, B.; Koo, Y.; MacFarlane, D. Introduction: Ionic Liquids. *Chem. Rev.* **2017** 117, 6633-6635.

12 Kawano, R.; Matsui, R.; Matsuyama, C.; Sato, A.; Susan, M.; Tanabe, N.; Watanabe, M. High performance dye-sensitized solar cells using ionic liquids as their electrolytes. *J. Photochem. Photobiol.* **2004**, 164, 87-92.

13 Basile, A.; Bhatt, A.; O'Mullane, A. Stabilizing lithium metal using ionic liquids for long-lived batteries. **7**, ncomms11794, doi:10.1038/ncomms11794

14 Kim, T.; Lee, H.; Stoller, M.; Dreyer, D.; Bielawski, C.; Ruoff, R.; Suh, K. High-Performance Supercapacitors Based on Poly(ionic liquid)-Modified Graphene Electrodes. *ACS Nano* **2011**, 5, 436-442.

15 Zhao, Y; Boström, T.; Passerini, S.; Moretti, A.; Bresser, D.; Zhen, Y. Rechargeable Iron-ion Battery. PCT patent application number: WO202007911.

16 Zhao, Y.; Hansen, J.; Boström, T. Extraction of magnetic nanoparticles using magnetic ionic liquids. *IET Micro & Nano Letters* **2015**, 11, 244-247.

17. Li J.; Li F; Zhang, L; Zhang, H.; Lassi, U.; Ji, X. Recent applications of ionic liquids in quasi-solid-state lithium metal batteries. GreenChE. **2021**, 2 (3), 253-265.

18. Song, X.; Wang, C.; Chen, J.; Xin, S.; Yuan, D.; Wang, Y; Dong, K.; Yang, L.; Wang, G.; Haitao Zhang, H.; Zhang, S. Unraveling the Synergistic Coupling Mechanism of Li^+ Transport in an "Ionogel-in-Ceramic" Hybrid Solid Electrolyte for Rechargeable Lithium Metal Battery, *Adv. Funct. Mater.* **2021**, 2108706-2108706.